Technische Universität München
Ingenieurfakultät Bau Geo Umwelt

Lehrstuhl für Wasserbau und Wasserwirtschaft
Dieter-Thoma-Labor

Development of a low head axial tidal turbine

Stephan Johann Sebastian Hötzl

Vollständiger Abdruck der von der Ingenieurfakultät Bau Geo Umwelt der Technischen Universität München zur Erlangung des akademischen Grades eines

Doktor-Ingenieurs

genehmigten Dissertation.

Vorsitzender:	Prof. Dr.-Ing. Michael Manhart
Prüfer der Dissertation:	1. Prof. Dr. sc. techn. Peter Rutschmann
	2. Assoc. Prof. Nils Rüther, Ph.D.

Die Dissertation wurde am 26.09.2018 bei der Technischen Universität München eingereicht und durch die Ingenieurfakultät Bau Geo Umwelt am 29.03.2019 angenommen.

Danksagung

Die vorliegende Dissertation entstand während meiner Tätigkeit als wissenschaftlicher Mitarbeiter im Dieter-Thoma-Labor des Lehrstuhls für Wasserbau und Wasserwirtschaft der Technischen Universität München. Eine wissenschaftliche Arbeit ist nie das Werk einer einzelnen Person, deshalb ist es jetzt an der Zeit, mich bei allen Menschen zu bedanken, die mir die Erstellung meiner Dissertation ermöglicht haben.

Mein besonderer Dank gilt Herrn Prof. Dr.-Ing. sc. techn. Peter Rutschmann, dessen vielfältige Unterstützung mir das Anfertigen dieser Arbeit ermöglichte. Herrn Assoc. Prof. Nils Rüther, Ph.D. danke ich für die Übernahme des Koreferates und das Interesse, das er meiner Arbeit entgegenbrachte. Für den Vorsitz der Prüfungskommision darf ich Herrn Prof. Dr.-Ing. Michael Manhart recht herzlich danken.

Ein ganz besonderer Dank gilt Herrn Dr.-Ing. Wilfried Knapp, der wesentlich zum Gelingen dieser Arbeit beitrug. Sein großer Erfahrungsschatz, sowie seine wertvollen Hinweise und viele interessante, lehr- und aufschlussreiche Diskussionen waren mir stets eine große Hilfe.

Für die stets außerordentlich gute Zusammenarbeit gebührt allen meinen Kollegen am Lehrstuhl für Wasserbau mein aufrichtiger Dank, sowohl denen die in München sitzen, als auch denen in Obernach. Speziell meinen Kollegen im Dieter-Thoma-Labor Tobias Schechtl M.Sc., Dipl.-Ing. Sebastian Roenneberg, Tatiana Stamou M.Sc., Thomas Siewert und Sardar Ateeq M.Sc. möchte ich für die ausgezeichnete Arbeitsatmosphäre und die fortwährende Unterstützung danken.

Auch bei meinen Bachelor- und Masterstudenten, die durch ihren Arbeitseinsatz zum Gelingen der vorliegenden Arbeit wesentlich beigetragen haben, möchte ich mich herzlich bedanken. Insbesondere Benjamin Richter M.Sc., Johannes Niebling M.Sc., Clara Wohnlich M.Sc. und Ayman Khalil M.Sc. gebührt Dank und Anerkennung für die gute Arbeit, die sie geleistet haben.

Ein herzlicher Dank gilt auch meinen Eltern Agnes und Sebastian, die mich jederzeit liebevoll unterstützt haben und immer für mich da waren. Der lieben Rosina gilt mein besonderer Dank für die Geduld und das Verständnis, welches sie mir entgegen brachte, sowie für ihre hilfreiche Unterstützung. Auch allen meinen Freunden, die mir immer zur Seite standen, bin ich zu großem Dank verpflichtet.

München, den 26.09.2018

Stephan Hötzl

Abstract

The present study describes the development of an axial water turbine with ring generator for use in tidal range power plants. The turbine's very compact design makes it possible to integrate all components into a reversible cylinder. Thus, the turbine can be optimized for one flow direction and by reversing the cylinder identical operating characteristics such as efficiency and unit discharge can be achieved in the opposite flow direction. As the turbine can be used also as a pump, it achieves an efficient four-quadrant operation, which can increase the energy output of tidal power schemes that are designed for a two-way operation with pumping.

This thesis gives an overview of the tidal range technology, its history, and state of the art. The new turbine concept is described in detail and the identified development targets are defined. A literature study gives insight into how much the new concept could increase the energy production of tidal power plants. Following this, the basis for the initial design is illustrated and the subsequent optimization process is described, which is based on three-dimensional computational fluid dynamics simulations with the software ANSYS CFX.

The operating characteristics of the final geometry are simulated over a wide range of unit speeds and unit discharges in both the turbine and pumping mode. The results show that the turbine concept is feasible and can achieve good operating conditions. However, the unusual concept brings with it some special requirements that lead to some restrictions. In particular the axial arrangement of the components induces a swirl distribution ahead of the runner that can only be mitigated by specially designed guide vanes.

Zusammenfassung

In der vorliegenden Arbeit wird die Entwicklung einer drehzahlvariablen axialen Wasserturbine mit Ringgenerator für den Einsatz in Gezeitenkraftwerken beschrieben. Die Besonderheit der Turbine liegt in einer sehr kompakten Bauweise, die es ermöglicht, alle wesentlichen Komponenten in einem Drehzylinder zu integrieren. Dies erlaubt es, die Turbine für eine Hauptströmungsrichtung zu optimieren. Durch Schwenken des Zylinders wird die Geometrie und somit auch die Hauptströmungsrichtung umgedreht, sodass die gleichen Betriebseigenschaften, wie z.B. Wirkungsgrad und Einheitsdurchfluss, in beiden Richtungen identisch sind. Durch ein Umkehren der Laufradrotation kann die Turbine auch als Pumpe betrieben werden. Die Turbine erreicht hohe Wirkungsgrade in allen vier Quadranten ihres Kennfelds. Dies erhöht die Energieausbeute insbesondere in Gezeitenkraftwerken, die in beiden Strömungsrichtungen arbeiten und zusätzliches Pumpen verwenden.

Die Arbeit zeigt zuerst die Geschichte und den Stand der Technik von Gezeitenenergie auf. Das neue Turbinenkonzept wird erklärt und die Entwicklungsziele definiert. In einer Literaturstudie wird aufgezeigt, wie hoch eine Steigerung der Energieerzeugung durch das neue Konzept ausfallen könnte. Anschließend wird dargelegt, worauf der Erstentwurf der Turbine basiert, und welche Entwicklungsziele identifiziert werden konnten. Der Optimierungsprozess der hydraulischen Kontur, welcher auf dreidimensionalen numerischen Strömungssimulationen mit der Software ANSYS CFX basiert, wird erläutert.

Die Betriebseigenschaften der finalen Turbinengeometrie wurden über einen weiten Bereich von Einheitsdurchfluss und Einheitsdrehzahl, sowohl im Turbinen-, wie auch im Pumpmodus simuliert. Die Ergebnisse zeigen, dass das vorgeschlagene Turbinenkonzept prinzipiell funktioniert und hohe Wirkungsgrade, sowie gute Betriebseigenschaften erreichen kann. Allerdings bringt die spezielle Konstruktion besondere Anforderungen mit sich, die zu gewissen Einschränkungen führen. So sind durch die sehr axiale Anordnung spezielle Leitschaufeln notwendig, um eine günstige Drallverteilung vor dem Laufrad zu erzeugen.

Contents

List of Figures

List of Tables

Nomenclature

Acronyms

CFD	Computational fluid dynamics
DES	Detached eddy simulation
DNS	Direct numerical simulation
FDM	Finite difference method
FEM	Finite element method
FVM	Finite volume method
GGI	General Grid Interface
IEC	International Electrotechnical Commission
LES	Large eddy simulation
RANS	Reynolds averaged Navier-Stokes
SST	Shear Stress Transport

Greek Symbols

β	blade angle	[°]
η	efficiency	[–]
κ	von Kármán constant	[–]
λ	friction coefficient	[–]
μ	dynamic viscosity	[Ns/m^2]
μ	flow rate number	[–]
ν	kinematic viscosity	[m^2/s]
ω	angular velocity	[rad/s]

ψ	head coefficient	[–]
τ	shear stress	[N/m^2]
θ	draft tube opening angle	[°]
φ	flow coefficient	[–]

Roman Symbols

$\dot{m}$	mass flow rate	[kg/s]
A	cross-sectional area	[m^2]
C	coefficient	[–]
c	velocity	[m/s]
c_{pi}	ideal pressure recovery coefficient	[–]
c_p	pressure recovery coefficient	[–]
D	runner diameter of the turbine	[m]
e	energy extraction factor	[–]
g	gravitational acceleration	[m/s^2]
H	hydraulic head	[m]
h_s	suction height	[m]
L	length	[m]
M	torque	[kg m/s^2]
m	draft tube area ratio	[–]
n	rotational speed	[min^{-1}]
n_1'	unit speed	[min^{-1}]
P	power	[W]
Q	flow rate	[m^3/s]
Q_E	unit discharge of 1	[m^3/s]
Q_1'	unit discharge	[m^3/s]
r	radius	[m]
Re	Reynolds number	[–]

S	span	[–]
s	width	[m]
SW	normalized streamwise length	[–]
u	blade velocity	[m/s]
u_*	friction velocity at the nearest wall	[m/s]
Y	specific supply	[m^2/s^2]
y	distance to the nearest wall	[m]
y^+	dimensionless wall distance	[–]

Subscripts

α	under consideration of the energy coefficient
dt	draft tube
f	friction
fl	fluid
i	inlet
M	model scale
m	meridional
me	mechanical
o	outlet
P	prototype scale
w	wall
d	runaway
gp	gap
l	loss
pu	pump
th	theoretical
tu	turbine
u	circumferential

Chapter 1

Introduction

This thesis describes the development and the characteristics of a new kind of tidal turbine that could allow to increase the energy production from tidal power plants. The concept for the principal function of the turbine was proposed by Tidetec AS, a Norwegian company. Based on this, a functional turbine was developed within the Eurostars-Eureka Project Safe*Coast. It seeks to mitigate the problem of suboptimal efficiency in the two reverse flow modes. To achieve this, the turbine is mounted in a reversible cylinder that can be turned by 180°. Thus, inlet and outlet are swapped, as is the position of the guide vanes and runner. The principle is illustrated in Figure 1.1.

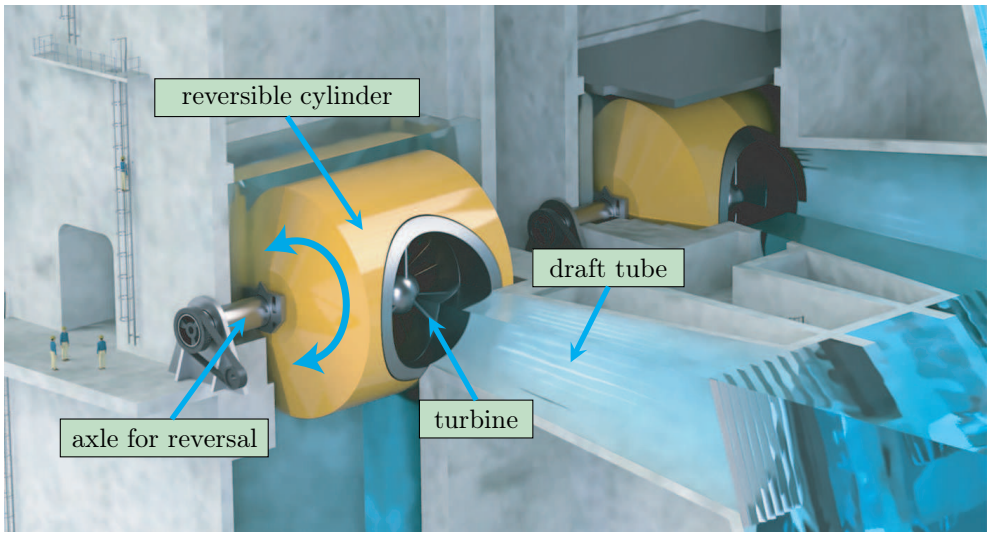

Figure 1.1: Concept of the turbine that is installed in a reversible cylinder (Figure courtesy of Tidetec AS)

The geometry is similar at the inlet and outlet and therefore equal efficiencies are reached in both flow directions. As the turbine needs to be designed for only one flow direction, no compromises need to be made in order to achieve satisfactory operating

characteristics in the reversed flow direction. At the beginning of the development, various turbine configurations were evaluated in a kinematic parameter study. Firstly, different combinations of adjustable and fixed guide vane and runner blade angles, as well as the adjustability of the rotational speed, were compared. Secondly, straight and curved blade profiles and rounded or sharp leading edges were evaluated. The third aspect was the reversibility of the turbine. The results of this work were presented in an earlier publication, see [1].

Based on these findings, a speed variable turbine with adjustable guide vanes and fixed runner blades was identified as the most promising concept. In order to make the turbine as compact as possible, it was decided to implement a rim generator, which avoids the need for a generator bulb that impedes the flow in the pumping mode. Turbines with this generator arrangement are referred to as Straflo turbines and are used for example in a number of submersible river hydro power plants in Germany [2] and in the Annapolis tidal power station.

The objective of this thesis is to give a general overview of the current state of the tidal energy sector, specifically the tidal range technology, and to verify whether it can be taken further with a new concept for tidal range turbines.

Firstly, the difference between one- and two-way operation of tidal power plants is outlined. A quantitative study based on the literature is used to determine to what extent a two-way operation can increase the output of tidal power plants and to assess how much pumping can add further. Design criteria that have to be met by the turbine to facilitate a successful operation are then identified. Examples of these are the head range, the specific speed, and the unit discharge. The constraints that arise from the new concept, which incorporate a turbine in a reversible cylinder, are identified so that solutions can be found in the subsequent design process. Based on this, the hydraulic contour of the turbine is designed and optimized using computational fluid dynamics (CFD) simulations.

Chapter 2

Tidal energy: a review

The following chapter gives an overview of the fundamentals of tidal energy and its use in the past and present, as well as possible uses in the future. The potential of the worldwide tidal energy potential is shown and operating schemes are explained. The purpose is to give an overview that makes it possible to put the new concept into an appropriate context that facilitates an assessment of its potential.

2.1 History of tidal energy

Making use of the rise and fall of tides has a history that goes back to ancient times. In the middle ages, the first facilities in the form of tide mills were constructed in Britain and France to grind corn. The remains of a tidal mill on Mahee Island, Ireland, were dated by dendrochronology to 619-621 AD [3, 4]. In England, the oldest recorded tide mill appears in the Domesday book from the 11$^{\text{th}}$ century [5]. It mentions a mill at the entrance of the port of Dover, Kent, that already existed in 1000 AD. Subsequently, the number of tide-mills in England increased. According to [6], eleven tide mills had been built by 1200 AD, and by 1600 AD there were a total of eighty-nine.

In the following centuries, however, the focus shifted to windmills, as tide mills were prone to destruction by storms. In other countries with high tidal range, many tide mills were built as well. Up to 150 former tide mills were recorded in France in 2004 [7], 90 of which were located in Britanny. On the Iberian Peninsula, there were 100 in the region of Cantabria, a region north of Spain, and 90 in the Gulf of Cadiz in the south [7]. On the other side of the Atlantic Ocean, on the coasts of North America, up to 350 tide mills were built [7]. With the invention and development of electricity, tide mills lost their usefulness and the total number of plants in operation declined. Tidal energy use, however, was reborn with the first large-scale tidal power plant, the La Rance tidal power station in France.

2.2 The physics of the tides

Tides are the rise and fall of the water levels of the sea that appear regularly at many coastal regions. They are mainly caused by a combination of the gravitational pull of the Sun and the Moon and the rotation of the Earth [8]. The amplitude and timing of the tides are determined by many variables and therefore differ in a temporal and spatial frame. The main influencing factors are the constellation of the celestial bodies, the bathymetry of the shoreline near the specific location, and the resonance effects of the oceans.

When the Sun and the Moon are in conjunction or opposition, i.e. on a line with the Earth, their combined pull leads to very high tides, which are referred to as spring tides. When the two bodies are at 90° to each other, viewed from the earth, the resulting tides are small and are referred to as neap tides. The time between neap and spring tides is roughly seven days, or a quarter of the 29.5-day lunar cycle as can be seen in Figure 2.1 [8].

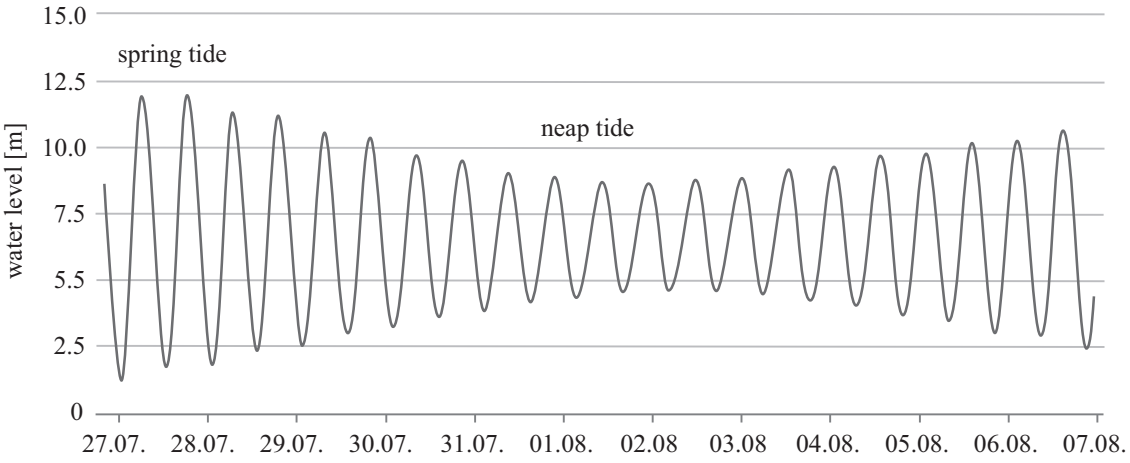

Figure 2.1: Tides at Dinan, Brittany near La Rance in summer 2017

The combined effects of resonance and declination of the earth lead to different tidal types at different coasts. A semi-diurnal tide has two nearly equal high and low tides a day, while a diurnal tide has only one high and low tide a day [9]. In some places, both types are present and this is referred to as a mixed tide. Figure 2.2 illustrates the different tide types. By monitoring the water levels at a specific location for an extensive time frame, i.e. at least one year, it is possible to determine harmonic constituents that describe the characteristics of the tide at the location very well. There are semi-diurnal constituents (e.g. M_2, S_2, N_2, K_2) with a period of roughly 12 hours, diurnal constituents (e.g. K_1, O_1, P_1, Q_1) with a period of roughly 24 hours and long period constituents (M_f, M_m, S_{sa}). The constituents with the largest impact

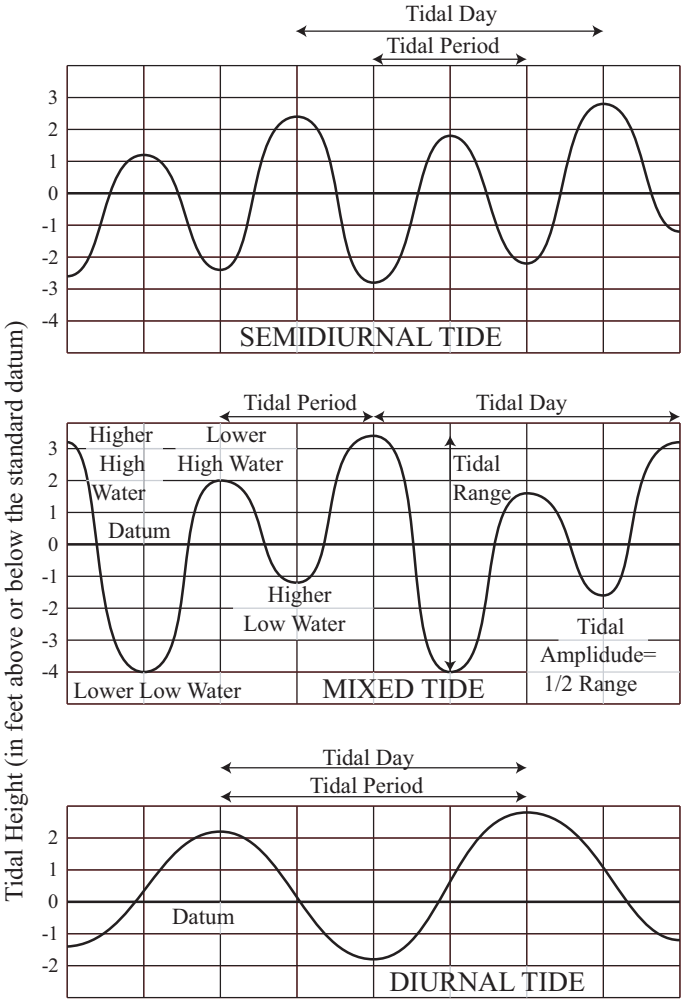

Figure 2.2: Principal types of tides, based on [10]

are M_2 and S_2, K_1 and O_1. For details on the harmonic constituents of tide-generating forces see Table A in the Appendix. With these parameters, a precise forecast can be made far into the future, making the tides a very predictable source of energy [11].

2.3 The potential of tidal resources

The physical process that creates tides is fundamentally different from the hydrological cycle that feeds the resources of hydro power. As a result, tidal energy, in contrast to hydro power, is a very predictable source of energy that has very small fluctuations from year to year and is relatively independent of the local weather or climate. According to [12], the theoretical potential of tidal energy is around 20,000–30,000 TWh/a. [13] states that the rate of dissipation of tidal energy in the Earth's shelf is on average about 21,900 TWh/a. Only a fraction of this potential can be used cost-effectively. Current studies suggest that the maximum recoverable tidal energy globally is around 1,800 TWh/a [14]. The total worldwide potential capacity is about 239 GW, whereas

the total global electrical generation capacity was about 4,300 GW in 2005 [15]. Based on these numbers, a significant share of 5.5 % of the global electricity generation capacity could be contributed by tidal energy. For comparison, the global generation capacity of wind power was 487 GW at the end of 2016 [16].

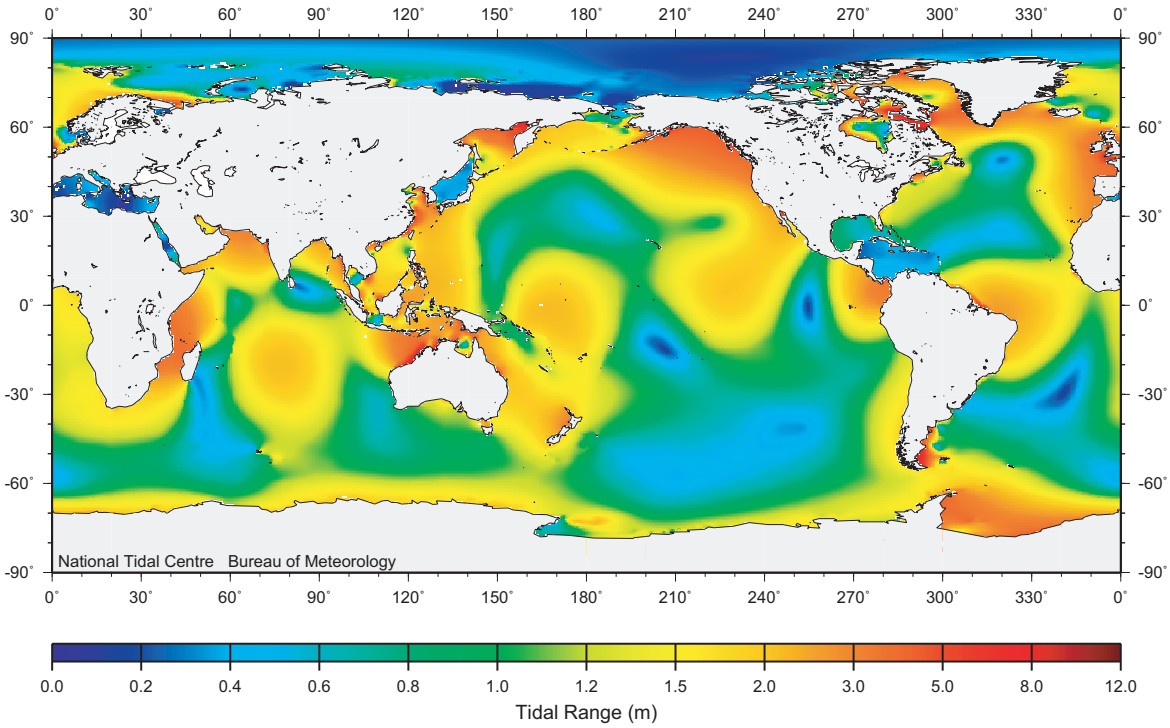

Figure 2.3: Map of the tidal range around the world, courtesy of James Chittleborough, Bureau of Meteorology, Australian Government

The energy that is produced by tidal power plants is proportional to the square of the tidal range at the location [11]. Locations with a large tidal range are therefore the most valuable and can be found on the coasts of all the world's oceans, as shown in Figure 2.3. According to [8], a tidal range of at least 5 m is considered to be the minimum for viable power generation.

In Europe, the UK possesses the largest resource with around 44–50 TWh/a, which amounts to about half the total European potential [8]. If the major tidal sites at the coasts of the UK are realized, up to 6 GW of tidal power could be generated during spring tides, resulting in an annual energy output of around 30 TWh/a [17]. The annual electricity supply in the UK was 349 TWh/a in 2017 [18].

2.4 Types of tidal power generation

There are currently two principal technologies for utilizing the movement of water induced by tidal forces. The first one is referred to as tidal range generation or power

generation from barrages and the second is referred to as tidal stream generation. The tidal range technology relies on the rise and fall of the tides and makes use of the different water levels between high tide and low tide. It was first employed in some of the ancient tide mills and is nowadays exploited by the use of hydraulic turbines. To make use of the difference in level between flood and ebb, a dam is built to separate a basin from the sea. Turbines and gates are included in the dam and allow for a regulated water exchange between the two water bodies. During the operation of the power plant, the dam is used to temporarily prevent the exchange of water during the transition between ebb and flood, thus creating a water level difference. When the turbines are operating, the potential energy of the water is converted into mechanical power and eventually electricity.

The second principle of tidal power generation does not use a difference in water levels but instead utilizes the kinetic energy of equalization streams flowing between high tide and low tide. It is therefore referred to as tidal stream power generation, and the corresponding tidal stream turbines are technologically different from the ones used for tidal range technology. They have a working principle comparable to wind turbines and are placed at locations where flow velocities are high. They rely entirely on the kinetic energy of the flow [8]. Thus, their energy density is comparatively low, which necessitates larger runner dimensions than in tidal barrage turbines, if the same power output is required. However, tidal stream turbines may be the better choice at sites where the construction of dams would be very expensive, or where the tidal range is very small. Moreover, tidal stream turbines have less impact on the environment, which circumvents some of the effects mentioned in Section 2.9. A great deal of research has been devoted to the advancement of tidal stream turbine technology in recent years, as described in [13].

This thesis focuses on tidal range turbines and therefore tidal stream turbines will not be described in more detail.

2.5 Operating schemes

Planning a tidal barrage power plant is a very complex task as there are many parameters that can be varied [11]. For a specific location, e.g. an estuary, the basin size depends on how far inside the estuary the dam is built. There are often multiple possible locations for the dam and these are dependent on geological features, the bathymetry and economic aspects. Once the basin size is determined, the number and size of turbines and sluice gates, as well as their location in the dam and their size and orientation must be determined. Apart from that, there is a variety of operating

schemes that define how the power plant is operated once it is built. Each type of operating scheme has specific benefits and downsides. The intended operating scheme has to be specified and its implications have to be considered in the planning process. To evaluate and assess different configurations, firstly 0D-simulations are usually employed that are subsequently followed by more detailed 2D-simulations.

When the generation of electricity takes place with water flowing in only one direction, e.g. from the basin to the sea, the operation scheme is referred to as one-way generation. In this case, turbines that are optimized for one flow direction, which is referred to as forward turbine operation, are used. The head and discharge, in this case, are positive, as depicted in Figure 2.4.

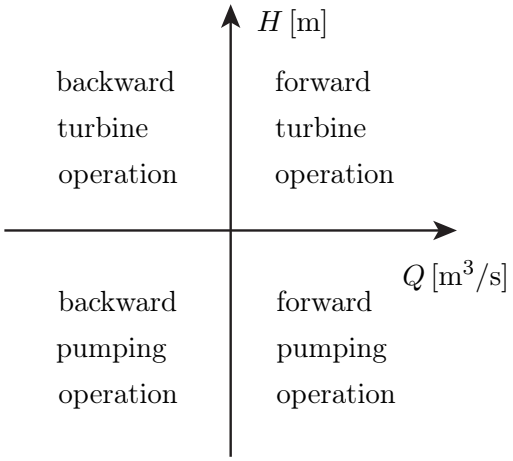

Figure 2.4: Four quadrants of turbine operation

When generation takes place with water flowing in both directions, i.e. from basin to sea and from sea to basin, the scheme is referred to as two-way operation. In this case, turbines that operate in the forward and backward turbine mode are used.

Both one- and two-way operations can be combined with pumping to further increase the energy output. In this case, the hydraulic head is also reversed , and turbines that operate in all four quadrants of a head-discharge diagram are necessary.

The details of the different operating schemes are described in the following section. First, single basin schemes are described. Later, multi-basin and alternative operating concepts are introduced.

2.5.1 One-way generation

One-way generation refers to a scheme where energy is produced only in one flow direction. There are two possibilities for the implementation of a one-way generation scheme – ebb and flood generation, and their properties differ.

Ebb generation The scheme depicted in Figure 2.5 is referred to as ebb generation, as the water level in the basin is higher than sea level during turbine operation. Production of electricity takes place while the basin is emptied during the ebb phase of the tidal cycle. The sea level falls and rises periodically in an approximately sinusoidal manner over time. Around hour eight, the water levels in the basin and in the sea are equal and the cycle begins with a waiting period. In this period the sluice gates and turbines are shut. After a while, when the head, i.e. the level difference between the water in the basin and the sea, reaches sufficient magnitude, the turbine operation starts and water begins to flow out of the basin, generating electricity. A few hours later the sea level reaches its lowest ebb level and begins to rise again while the basin water level is still falling. Shortly after, the turbines have to be stopped as the hydraulic head is below their minimum operating head. There is now another waiting time until both water levels are equal again. At this point, the sluice gates are opened, which allows the sea to flow into the basin. If the turbines are capable of idling while still allowing water to flow, an operation referred to as orifice mode, they can be used as additional capacity to fill the basin. The sea level rises further while the basin level also increases. Due to the limited gate capacity, the reservoir level stays somewhat below the sea level. Some hours later both water levels are again equal and the cycle begins again.

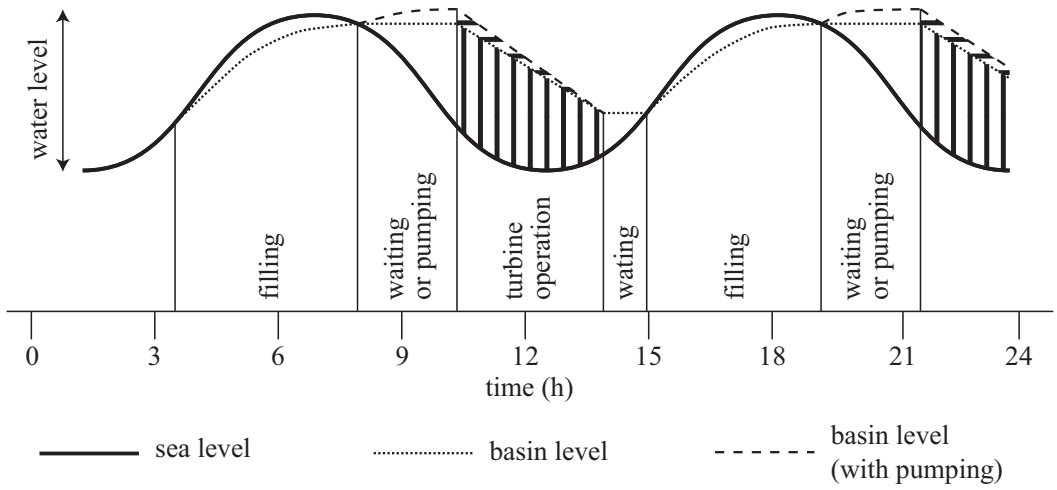

Figure 2.5: Scheme of a one-way operation scheme

Flood generation Another possibility is to reverse the scheme. In this instance, electricity is generated while water flows from the sea into the basin during the flood, thus filling it. After the generation phase, the basin is emptied again during the ebb phase.

The energy obtained in a flood generation scheme is less than in an ebb generation

scheme of equal size. This is due to the bathymetry of river estuaries, which in almost all cases has bed levels and embankments that slope upwards away from the dam. Thus, a greater volume of water is contained in the upper sections of the basin as compared to the lower sections. For this reason the water level rises very quickly when the filling begins, as only a small volume of water is needed to fill the bottom of the basin [19]. This leads to a quickly diminishing hydraulic head after turbine startup [11]. Ebb generation schemes are therefore generally more efficient than flood generation schemes; however, the exact relation depends on the specific location and there may be circumstances that make flood generation necessary, e.g. at the Lake Sihwa tidal power plant in South Korea, see Section 2.7.5.

2.5.2 Two-way generation

It is also possible to combine ebb and flood generation into one scheme, which is referred to as two-way generation. In this instance, the operation takes place in both the flood and ebb phase of the tidal cycle, i.e. when the basin is emptied and filled.

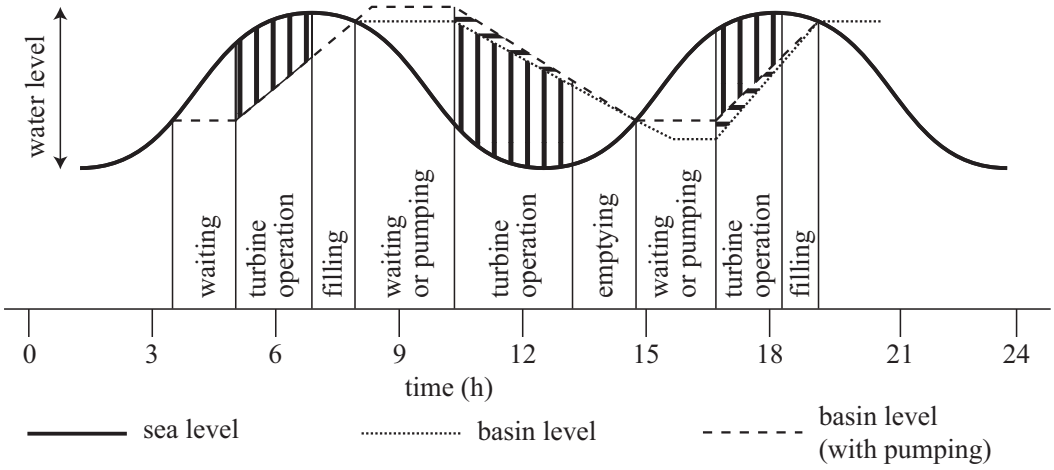

Figure 2.6: Scheme of a two-way operation scheme

The resulting graph of water levels resulting from a two-way generation scheme is depicted in Figure 2.6. During the ebb period, it looks similar to the one-way generation scheme. However, the turbines also operate in the flood period. Due to the increased overall generation time and the fact that a greater proportion of the moving water flows through the turbines the overall amount of produced energy can be increased. This, however, depends on many parameters and the improvement is less than one might expect.

Generally, the individual generation periods during ebb and flood are shorter than they are in one-way generation, due to a limited sluicing capacity. Moreover, the sluices have to be opened earlier towards the end of each generation phase, in order

to reduce the basin level quickly to provide for the period of flood generation or to fill the basin as quickly as possible before the start of ebb operation [19].

The hydraulic heads in a two-way scheme are generally lower than in a one-way scheme in a comparable tidal power plant and the efficiency of existing turbines that are capable of reverse operation is lower.

In [20] an analytic theory is presented that makes it possible to estimate the energy output of specific tidal power schemes. It uses dimensionless parameters based on the mean tidal range and the surface area of an enclosed basin. By applying this framework, it is possible to calculate the energy output at a specific location and to compare one- and two-way generation. The theory does not consider the number of turbines, their size, or the presence of sluices. It can be shown theoretically that with one-way generation 27 % of the potential energy of the water stored in the basin can be extracted. This is expressed with the energy extraction factor being $e = 0.27$. With two-way generation, the energy extraction factor is $e = 0.37$, which in turn represents an increase of 37 % when compared to one-way generation. However, this theory fails to account for the facts that firstly the turbine efficiency in a two-way scheme usually is not equal in both flow directions and secondly that the average heads during operation are lower. The paper's conclusion is that a two-way scheme has theoretical advantages in energetic aspects, that may be reduced by practical engineering realities [20].

In [11] equations to predict the annual energy production at specific locations are introduced that are, in keeping with the theory presented in [20], based on the average tidal amplitude and the basin area. The author makes use of the optimum values of the energy extraction factor e determined in [20] and compares the calculated energy output of tidal power plants to their preliminary design data. Depending on the location, the predicted values of the annual energy output have a discrepancy of between -20 % and 66 % with the design data. This comes from the neglect of parameters such as turbine capacity, the effect of pumping, and the basin geometry.

A project that has been proposed many times is the implementation of a tidal power plant in the Severn estuary in Great Britain, between Wales and England. In the course of developments, a large amount of research has been conducted into the operation of the proposed plant. In 2007 the Sustainable Development Commission concluded that one-way ebb generation with pumping would be the method with the highest potential output at this location [21].

Regarding two-way generation, a World Energy Council report states that the energy production when combining ebb and flood generation is in principle feasible, but there is no major increase in energy production [22]. Unfortunately, this claim is not supported by quantitative studies.

According to [23, 24] the efficiency in a two-way generation scheme is inherently lower because turbines and water flow cannot be optimized. Unfortunately, it is not clear if these results are based on models that use a turbine with equal efficiency in both flow directions. If this is not the case and the models use lower efficiencies for reverse turbine mode, energy production in two-way generation may be underestimated. A turbine that works equally efficiently in both directions may result in a greater energy production that could significantly surpass one-way production. However, making a quantitative assessment of this claim is quite challenging and can only be done with extensive simulations.

2.5.3 Pumping

Another concept for increasing the energy output of a tidal power plant is to use the turbines to pump during appropriate periods. It is possible to include pumping in both one-way or two-way generation schemes and in both cases the basin water level can either be pumped up to higher than the maximum sea level or pumped down to lower than the minimum sea level. The principle is illustrated in Figures 2.5 and 2.6.

In general, pumping increases the available tidal range between the basin and the sea. In the following example, a site is assumed where the tidal range is 4 m and pumping during high tide increases the water level in the basin by one meter. In the subsequent ebb cycle, the available head will be one meter greater than without pumping. While the turbine generator is used as a motor during pumping it consumes energy that is retrieved later in the cycle [25]. As pumping takes place under low heads, the energy needed per volume of water is comparatively small. The same volume of water drives the turbines at a later time when the head is much greater, leading to an overall gain [26].

There are limits on how extensively pumping can be used. Firstly, it is not possible to lower the basin water level further once the basin is empty. On the other hand, overfilling of the basin is limited by the height of the dam and the surrounding embankments as well as local legislation. Moreover, the turbines necessary for pumping operation are more complex as they have to be capable of the additional mode.

The study presented in [27] concludes that "Use of positive head pumping [...] is found to increase energy capture generally by somewhat less than 10 % in ebb generation, and the gain is found to be sensitive to barrage configuration and estuary bathymetry. Greater returns in energy with pumping are found to be achievable from dual (two-way) generation and for schemes of larger installed capacity". Net gains from flood pumping at a proposed Shoots Barrage in the Severn Estuary are predicted by a 2D-Model to be 2.7 % [28]. In a case study at Morecambe Bay, England it was

confirmed that energy gains from pumping are proportionally higher when the turbine number increases. With a pumping efficiency of only 40 % "...the net annual energy gains were found to be approximately 7 %, 13 % and 1 % for ebb, flood and dual modes, respectively" [17].

The authors of [26] conclude that "pumping at high tide substantially increases the energy potential of the subsequent generating period, typically by about 10 %". Moreover, "the inclusion of pumping at negative heads increases the potential energy output from an 8.5 m tide by more than 1 GWh (about 3 %), even if the efficiency of the process is as low as 20 %".

The conclusion of [29] is that besides combining flood and ebb generation at the Sihwa Lake tidal power plant "...an additional increment of 21.25 % in annual power output is achieved incorporating pumping additionally". These numbers show that it is not possible to make a universal statement as to how two-way operation and pumping influence annual energy production. It is very probable that this depends significantly on the basin geometry, tidal amplitude, resonance effects in the basin, pump and turbine performances and installed turbine capacity. Detailed values have to be determined for each project using increasingly detailed simulations during the planning phase.

2.5.4 Multi-basin schemes

The single basin schemes described above have been implemented in existing tidal power plants. There are, however, alternative concepts that are more complex but could have benefits. In a single basin design, "power can be produced for five to six hours during spring tides and three hours during neap tides" [8] during one tidal cycle. For a semi-diurnal tide with a period of 12.4 h and one-way generation, this means that there are two bursts of electricity generation each day. These bursts do not necessarily align very well with the daily demand pattern of the electrical grid. However, as the production times of the tidal power plant can be predicted very well, the energy produced could be used to reduce the output of base-load power plants. A two-way generation scheme would create four, albeit shorter, bursts of generation each day, which would result in a more continuous power output.

To obtain an even steadier output of a tidal power plant, many different proposals to use more than one basin, i.e. multi-basin schemes, have been made. A double basin scheme consists of two basins that are separated from each other and the sea with dams. In each dam, turbines are installed that allow for a water exchange. This makes it possible to have completely continuous energy production, but a downside is that the annual energy production is lower than in a plant with intermittent production.

However, these schemes could potentially lead to a more flexible operation that is less dependent on the natural tidal cycle. In a double basin installation of this kind, excess energy produced by the turbines of the first basin could be used to pump water into the second basin during times when the electricity demand is low. The stored water in the second basin could then be used to produce energy at a later time, when the electricity demand and therefore prices on the market are higher.

A major drawback to multi-basin schemes is that not only one, but multiple barrages have to be built. This increases the already high investment costs significantly and therefore no multi-basin schemes have been built to date.

2.6 Turbines used in tidal power plants

As in hydro power technology, the electricity in tidal energy is generated by hydraulic turbines. Figure 2.7 shows the application range of the established turbine types. As the head range in tidal applications is between 1 m and 15 m, only three types of hydraulic machines are suitable for use in tidal barrages: water wheels, cross-flow turbines, and Kaplan turbines. In the following sections, the different turbine types are assessed regarding their suitability for the development targets of this thesis.

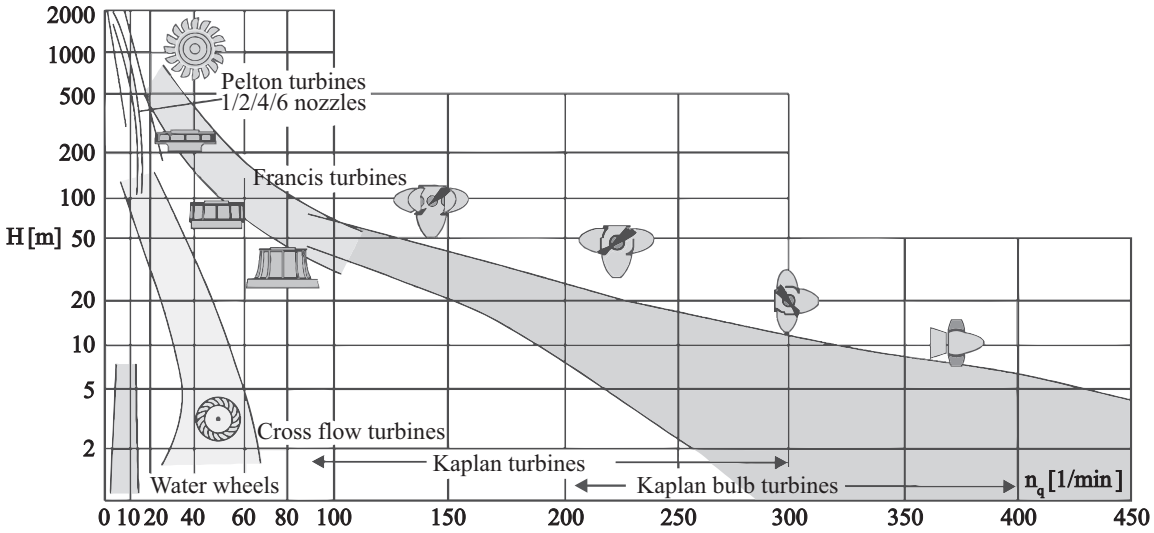

Figure 2.7: Application ranges and specific speed n_q of different turbine types, depending on the head H, based on [30]

Water wheels

Water wheels were used in tidal mills, but have a limited efficiency at small heads when stream, undershot or breastshot water wheels are used. For heads of more than

a few meters backshot or overshot water wheels can be used that have efficiencies of over 80 %. The main disadvantages, however, are the low specific speed, which is disadvantageous for the electric generator, and the low unit discharge, which demands extremely large dimensions. For these reasons, water wheels are not used in modern tidal power plants.

Cross-Flow turbines

Cross-flow turbines, also referred to as Bánki-Michell turbines, or Ossberger turbines, are low specific speed impulse turbines that are mostly used for small and medium heads of 2–50 m in small hydro power plants. The runner blades are fixed and do not permit an adaption to the discharge. However, a segmented layout of the guide vanes in 1/3 and 2/3 of the runner width leads to a relatively flat efficiency curve [31]. At low discharges, the smaller segment is opened while the larger is closed. At medium discharges, the condition is reversed, and for high discharges, both segments are opened. As the turbine layout relies on only a small number of parts, it is easy to manufacture and to maintain.

One disadvantage of cross-flow turbines is their low specific speed, which results in a low power density when they are constructed for low heads. In conjunction with the high discharges that need to be processed in tidal barrages, this leads to very large turbine dimensions. Furthermore, the low speed leads to very large generator dimensions unless a step-up gearbox is used. Narrow blade passages and a high number of blades could be challenging in a seawater environment, as they are prone to clogging and entangling by plants. The large wetted surface area of the turbine leads to high friction losses and overall efficiencies limited to approximately 80 % at the design operating point [31].

Due to their construction type and working principle they are not capable of pumping or two-way generation. These properties rule out cross-flow turbines for use in large-scale tidal applications.

Orthogonal turbines

Over the last few decades, a new type of turbine has been introduced by A. Gorlov [32]. It was originally proposed for use as a hydrokinetic turbine and its functional principle is based on the vertical axis Darrieus type wind turbine rotor: a vertical shaft carries a number of blades oriented more or less in parallel to the rotational axis. During a single revolution of the runner, the flow conditions at each blade change over time, which leads to large torque variations. However, on average, positive torque is created, which is independent of the flow direction. This feature is favorable for

two-way operation.

In the original Darrieus design, the blades were given a parabolic shape to reduce the bending stresses caused by centrifugal forces. When used as a hydrokinetic turbine, the rotational speed is much lower in comparison to its speed in the air due to the much higher density of water and lower flow velocities. Centrifugal forces are thus much smaller and thus there is no need for a parabolic blade shape. This permitted Gorlov to give the blades a helically twisted shape, which greatly reduces the torque fluctuations compared to a Darrieus rotor. Reported efficiencies of the turbine reach approximately 35 %. This seems to be quite low but needs to be seen in the context of the Betz limit of 59.3 %, which applies for free stream turbines [33].

Counter-rotating turbines

In recent years, turbines with two rotors in series, turning in opposite directions, have been suggested and evaluated. At the University of Strathclyde, UK, a marine current turbine with a second rotor behind the first one was developed [34]. The main advantage is that the torque reaction of the whole turbine is greatly reduced as the torque components induced by both rotors cancel each other out to a great extent. This allows for lighter mounting structures and is especially important for turbines mounted on floating structures, where the residual torque changes the trim of the float. Another advantage is that the swirl in the wake of the turbine and the losses pertaining to it are reduced. As marine current turbines typically do not possess a guide vane apparatus that creates an inlet swirl, an outlet swirl is induced. With a second, counter-rotating rotor this swirl can be reduced and additional power can be generated.

The design employs an unusual generator assembly where there is no stator but two counter-rotating generator rotors. Moreover, the blade-to-blade interactions of the front and rear runner lead to dynamic loads that induce oscillations. This can create fatigue problems in the long run. More details on this technology can be found in [34]. A counter-rotating design has also been proposed for axial Kaplan turbines by different research groups [35, 36, 37]. In these cases, the guide vane apparatus is replaced by a rotor that is arranged directly in front of the existing rotor. At the South China University of Technology in Guangzhou numerical models have been created to evaluate the idea [38]. Results from this study suggest that with unchanged turbine dimensions an increased head can be used and therefore more power generated. The downside is again a more complex generator design, and also that both runners have to be equipped with adjustable blades. This is mechanically rather complex and economically costly.

Researchers at the University of Tokushima in Japan have carried out similar simulations for small-scale axial turbines [37]. Their results are not as promising, since a major drop-off in efficiency is expected to occur at the second rotor when the flow rate deviates from the design flow rate.

Another research group from the Japanese Kyushu Institute of Technology has dealt with the topic of counter-rotating axial turbines for replacing standard Kaplan bulb turbines. They ran an on-cam test with a model unit, compared different blade configurations, and tested a new type of synchronous generator. The hydraulic performance of the turbine reached 90 % [36]. At the University of Applied Sciences and Arts Western Switzerland another model turbine with counter-rotating runners has been built and evaluated. The design is intended to be used for pressure reduction in drinking water supply systems. The research group's conclusion suggests that regulation of the turbine can be accomplished by varying the ratio of rotational speeds of the runners. The turbine reached an efficiency of 83 % in numerical simulations, however, model tests resulted in a efficiency in the best efficiency point of 53 %. Thus, further design optimizations are needed [39].

Overall, recent publications show that counter-rotating turbines are in principle feasible. To some degree, they share the properties of standard Kaplan turbines. As energy conversion is distributed on two runners instead of one, larger heads can be used with the same runner diameter. This is especially interesting in medium-head hydro-power stations, where it might permit the use of bulb turbines in head ranges formerly restricted to Kaplan spiral or semi-spiral turbines with their inherently larger dimensions. However, with the low heads normally available in tidal barrage applications, only a rather moderate reduction in size can be expected while the mechanical complexity, especially in double-regulated designs, is considerable.

Tubular turbines

Tubular turbines are the most common technology used in low head hydro power and tidal power plants. There are countless hydro power stations around the world equipped with this reliable and highly developed technology. Tubular turbines for the use in run-of-the-river hydro power plants are optimized for only one flow direction. According to [2], the first tubular turbines were commissioned in 1936 in Rostin, Poland by the Swiss turbine manufacturer Escher Wyss. Research since then has led to a mature technology. Depending on the working conditions there are different kinds of tubular turbines that mainly differ in the arrangement of the generator. These designs are described in the following paragraphs.

Bulb turbines For large turbines with runner diameters of 2.5 m or greater the bulb configuration is normally used. In this design, the generator is encased in a steel bulb that is immersed in water. Static and dynamic seals are required to avoid ingress of water into the generator bulb and in some cases, the bulb is additionally pressurized by air. This reduces the pressure difference between the inside and the outside of the bulb and as a side-effect the denser air has a greater cooling effect upon the generator. Access to bearings and the generator is provided by service shafts. Nowadays the bulb is arranged in the upstream part of the turbine. Some early designs with downstream generators were tried, but experiments showed that this configuration is unfavorable [2], mainly due to drawbacks in draft tube efficiency. The same is true if the flow direction is reversed.

It is possible to drive the generator directly by mounting its rotor on a common shaft with the turbine runner, which has the advantage of high efficiency, low maintenance, and long life. However, due to the low rotational speed of low head turbines, the dimensions of the generator have to be relatively large. This limits the overall power rating of the turbine as the generator size is limited by the feasible size of the bulb.

To overcome this issue, a planetary step-up-gear can be included between runner and generator. This permits using a fast running, high power generator with relatively small size inside the limited space of the bulb. The drawbacks of this layout are the efficiency penalty induced by the gearbox losses, increased maintenance requirements due to the added auxiliary equipment like oil pumps, coolers and filters, and the difficulty in designing a generator that can withstand the high rotational speeds occurring in a turbine runaway condition. All in all, the bulb configuration is best suited for large units in river hydro power plants and tidal power plants, and the most common setup is the direct drive solution.

Bevel gear turbines One alternative to arranging the generator in a bulb is to use a bevel gear drive. The runner axis intersects the generator axis at an angle of 90°. The two shafts are connected by a gearbox that can be designed to work as a step-up-gear. This allows for a small bulb size and for the generator to be situated completely out of the waterway. This eases up sealing and makes the generator easily accessible. Using a step-up gear allows for small, high-speed generators with all their advantages, however, runaway of the turbine can be problematic just as it is with bulb turbines.

In general, bevel gears are problematic when it comes to adjustment and service life. Permanent oil circulation and cooling systems are necessary to provide smooth operation. High manufacturing precision and high-class maintenance are required to

allow for high availability. Small units can be prefabricated and aligned at the manufacturer. Large units have to be assembled at the power plant site. Especially with large dimensions, it becomes challenging to adjust the gears correctly. It is necessary to pretension the assembly while making this adjustment in order to guarantee a good fit during working conditions. Equipment to induce the pretension force is costly and complex and does not even exist for large dimensions. To sum up, bevel gear configurations are a good option for small units but are problematic with large turbines [40].

Rim generator turbines A third option, the Straflo (a portmanteau word for straight flow) turbine, was suggested by Leroy F. Harza in 1919 and subsequently developed by Escher Wyss. The idea is to mount a generator directly at the outer perimeter of the turbine runner and dispense with the driving shaft. The rotor assembly is fixed on a rigid ring at the tip of the runner blades. Dynamic seals prevent water flowing into the gap between stator and rotor and therefore the whole generator assembly is outside the waterway. The large diameter of the generator runner means that a high circumferential rotor velocity can be attained without using a step-up gearbox, which makes for a compact generator design. Moreover, the large diameter has a high moment of inertia, which stabilizes the speed of revolution and is beneficial in a runaway condition [2]. However, keeping the generator dry is a quite demanding task requiring a rather complex sealing system. Early versions of the Straflo turbine suffered from sealing problems, but these were resolved by advances in the technology. However, research is still going on with the aim of equipping old Straflo turbines with improved sealing systems [41].

The further development of permanent magnet generators has created a new solution to the sealing problem: The rotor, with permanent magnets encapsulated within a synthetic resin, can be designed to run in the water, while the stator is sealed off with a static seal as is the case with canned motors. A small bulb is still needed to house bearings and to guide the flow. When using a wet running rotor the sealing system becomes simple.

The advantages of this construction type are a large rotor diameter and a purely axial flow without obstruction. The discharge capacity is 10 % greater in comparison to the Kaplan Turbine [40]. The overall length of the turbine is comparatively small and the compactness high, which saves construction costs on the civil engineering side.

Some Straflo turbines have been built with adjustable runner blades in the past, but this has proven to be troublesome. The runner blades could not be adjusted during operation of the turbine because forces in the connections between blade and rim were too large [40], and the sealing of the generator proved even more challenging

due to alignment difficulties. Thus, the Straflo turbines operating today have fixed runner blades. This is a disadvantage if the turbine needs to operate over a wide range of discharges or a wide range of heads. However, the latter condition, which is a challenge in tidal barrage applications, can be successfully overcome by using variable speed generators. According to [42] a variable speed turbine with variable guide vanes, i.e. distributor and fixed blades, has the highest annual energy output of regulation methods, as is depicted in Figure 2.8.

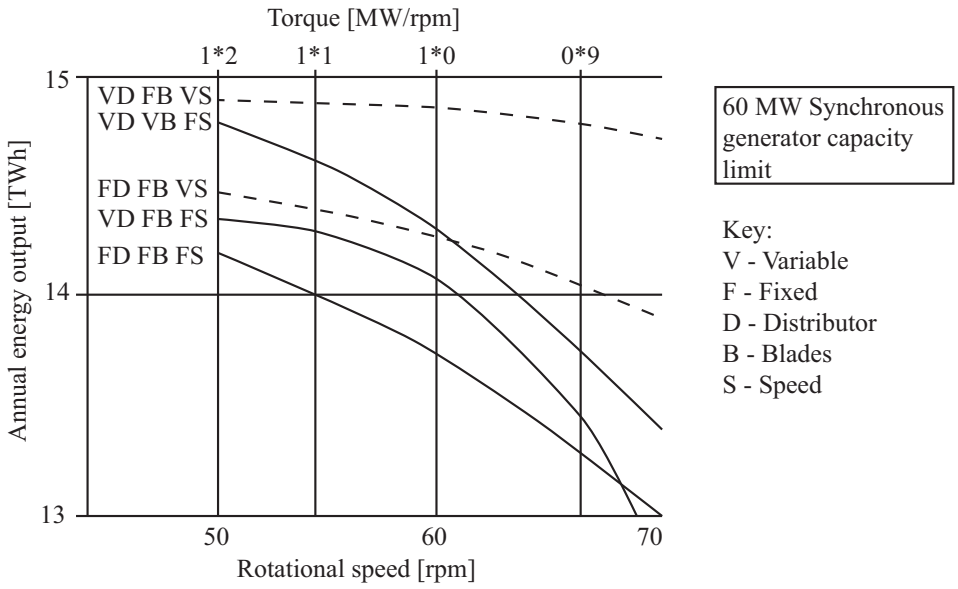

Figure 2.8: Different regulation methods of hydraulic turbines [42]

Straflo turbines can be built with large dimensions. However, the outer rim of the runner is many times heavier than the runner itself, which makes the construction dependent on a special bearing system. Escher Wyss uses self-stabilizing, hydrostatic support elements that are arranged around the outer rim.

Between 1937 and 1951, a total of 73 axial flow turbines with rim generators were installed in 14 power stations on the rivers Iller, Lech and Saalach in Germany, according to [40]. In the Annapolis tidal power plant, a Straflo turbine runs smoothly and quietly and has operated since it entered commercial service in 1984 with a high level of availability [43].

2.7 Existing tidal power plants

Although the worldwide tidal energy potential is very high, as described in Section 2.3, only a small number of tidal power plants have been built to date. The main reasons for this low count are environmental concerns, which are discussed in Section 2.9, and reasons of political and economic nature. An overview of the existing tidal power plants and the used turbines is given in Table 2.1.

Table 2.1: Characteristic data of turbines used in existing tidal power plants

	D [m]	H [m]	Q [m^3/s]	$\# \cdot P$ [MW]	Turbine type
La Rance [19]	5.35	rated: 5.65	rated: 275	$24 \cdot 10$	Bulb turbine
Kislaya Guba 1968 [11]	3.30	rated: 1.28 range: 0.5-2.5	rated: 50	$1 \cdot 0.4$	Bulb turbine
Kislaya Guba 2004, 2006 [44]	2.50 5.00	rated: 1.8 n/a	n/a n/a	$1 \cdot 0.2$ $1 \cdot 1.5$	Orthogonal turbine
Annapolis [19]	7.60	rated: 5.50 range: 1.4-7.1	rated: 378 max: 407.5	$1 \cdot 19.6$	Straflo turbine
Jiangxia [45]	2.50	rated: 3.00 range: 1.2-5.5	rated: 29.7 max: 34	$1 \cdot 0.545$ $1 \cdot 0.655$ $4 \cdot 0.760$	Bulb turbine
Lake Sihwa [46]	7.50	rated: 5.82 range: 2.0-6.0	rated: 482 max: n/a	$10 \cdot 25.4$	Bulb turbine

2.7.1 La Rance tidal power station

The first tidal range power plant put into operation was the La Rance tidal power station near St. Malo at the estuary of the Rance river in France. Construction began in 1961 and in December of 1967 all generating units were connected to the grid [11]. The power plant consists of a dam with a length of 720 m and powerhouse with 24 bulb turbines with a rated power of 10 MW each. The enclosed basin has a surface area of 4.75–22 km and the tidal range at the location is between 3 m and 13.5 m. Under these conditions, the yearly energy generated amounts to approximately 538 GWh/a [47].

La Rance was originally intended as a pilot plant to evaluate the feasibility of large-scale tidal power plants and the characteristics of different operational modes. For this reason, a bulb turbine was specifically designed for the project in a large-scale development programme. In 1959 the resulting design was tested in a separate

installation in Saint-Malo preceding the construction of the actual power plant. It was considered to be a good design and was then produced with slight modifications for the final power plant. It allows for a two-way generation and pumping in both flow directions. However, the maximum efficiency in most of the modes is not optimal with 87 % in the forward turbine mode, 73 % in the backward turbine mode, 58 % in the backward pumping mode and 66 % in the forward pumping mode [11]. In order to protect the mechanical equipment from corrosion, a cathodic protection system was installed, consisting of "three crowns of 12 anodes per turbine, representing 864 in total" [47]. The La Rance tidal power station is still in operation; it has provided many possibilities for research and deep insight into the operation of tidal range power plants.

2.7.2 Kislaya Guba tidal power station

The construction of the Kislaya Guba (Russian for 'sour bay') tidal power station began in 1964 and its commissioning in 1968 made it the second of its kind in operation. The whole site is much smaller than the La Rance tidal power station, but it was also originally plannes as a pilot plant. The mean tidal range at the location is 2.27 m and the basin has a mean surface area of only 1.1 km^2 [11].

The location in the northwest of Russia, near the border to Finland, puts some special requirements on the powerhouse, as low temperatures lead to heavy ice formation in the basin. Therefore, it was necessary to use special ice- and salt-resistant materials with high rigidity [48]. "The materials were tested to withstand the demanding conditions experienced in the tidal zones where water salinity was observed to be up to 35 %, air temperature down to −46 °C, water temperature ranging from −1.75 °C to 10.5 °C, and there are 450 freeze and thaw cycles per year" [48].

It was planned to install two turbines in the powerhouse, one of which was a bulb turbine with a rated power of 0.4 MW to be produced by Neyrpic-Alsthom from France. The generator was specifically designed for the power plant and was speed variable, which increased the efficiency of the turbine by five percent [49]. Its efficiencies are 86 % in the forward turbine mode, 76 % in the backward turbine mode, 67 % in the backward pumping mode and 63 % in the forward pumping mode [11]. A second turbine with a variable speed generator was planned and was supposed to be manufactured by a Soviet company. When it became clear that the second unit could not be delivered, the design of the plant was changed and the penstock of the second unit was used as a sluice opening. The power plant operated in one-way ebb generating mode until 1991 when it was put into idle mode after an emergency with the generator [50]. Between 1999 and 2004, the French bulb turbine was dismantled and a vertical axis orthogonal

turbine with a runner diameter of 2.5 m and a power rating of 0.2 MW was installed to replace it. In 2006, another similar turbine with a runner diameter of 5 m and a rated power of 1.5 MW was installed. The turbine was tested in field tests and is said to have reached a maximum efficiency of 71 % [49]. This is so far the only known application of this kind of turbine that makes use of a static head. A major advantage of the orthogonal turbine is the simple design, which makes it easy to manufacture, e.g. by rolling of the blades, thus allowing for cost savings of up to 30 % [49].

2.7.3 Annapolis Royal tidal power station

The Annapolis tidal power station was constructed in 1984 in the Annapolis Basin, a sub-basin of the Bay of Fundy, Canada. The tidal range at the location is about 8 m, which is roughly half of the maximum range reached in the Bay of Fundy, see Figure 2.9 [51]. The mean tidal range at the location is 6.4 m and the size of the basin is roughly 7.5 km^2 [11].

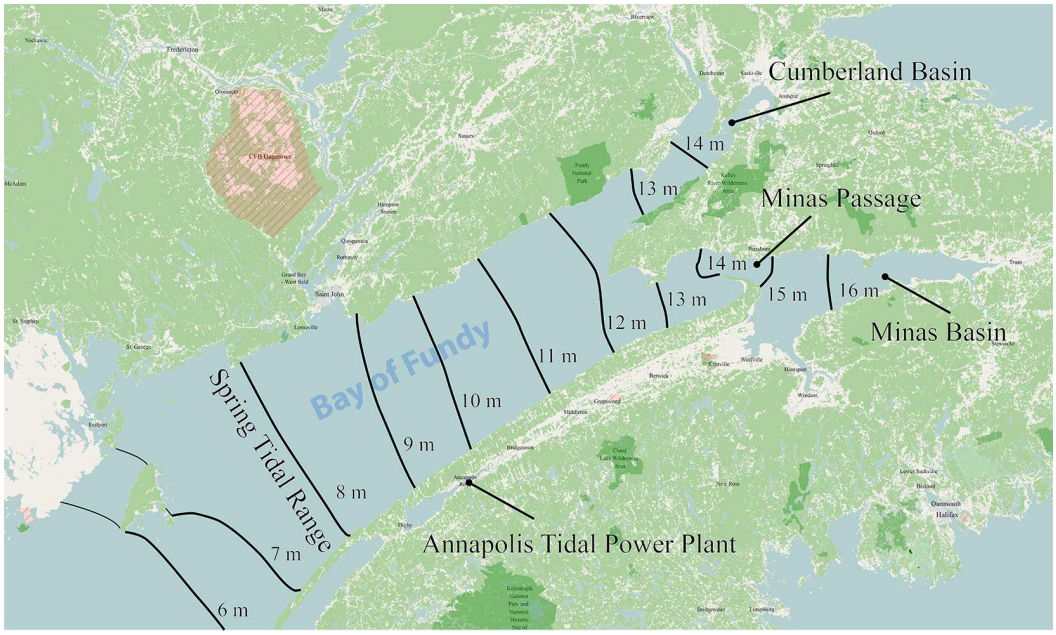

Figure 2.9: Map of the Bay of Fundy, Canada, based on [52]

It is the only tidal power plant in North America and unlike the other existing power plants, it uses a single Straflo turbine, the largest of its kind with a diameter of 7.6 m and a rated power of 20 MW. This turbine type was chosen because the manufacturers stated that the construction cost of future tidal power plants could be reduced by 10 % [11]. The power plant operates in one-way ebb generation mode with a maximum efficiency of 89.1 % [51]. Each generation period has a duration of 6 hours. Annually it generates about 50 GWh of electricity.

2.7.4 Jiangxia tidal power station

In China, semidiurnal tides with usable ranges of up to 8.93 m can be found on the eastern coasts. The mean tidal range there is over 4 m, which makes the construction of tidal range power stations viable [11]. In the 1960s several very small tidal power stations, each with a power of less than 1 MW, were constructed. However, many of them operated only for a few years, owing to "poor choices with locations and using flawed turbine designs" [25].

In the 1980s several plants with higher power and more options for regulation emerged, seven of which, with a total installed capacity of 10 MW, were still operational in 1996 [11]. According to [53] 128 plants were in operation with a total capacity of around 7.6 MW. After eleven years of construction, the Jiangxia tidal power station, which is the largest yet in China, was commissioned in 1985. Its dam was originally designed for beach reclamation purposes, but during construction, it was decided to redesign the plans and to include a tidal power plant. The powerhouse was designed to be equipped with six turbines, five of which were installed between 1981 and 1985 with a cumulative capacity of 3.2 MW. The sixth turbine was installed much later, in 2007, and raised the generating capacity to 3.9 MW [45]. Electricity generation amounts to 6.5 GWh per year and the maximum tidal range at the location is 8.39 m. The tidal power station operates in two-way generation without pumping, an operating scheme that is required for the original purpose of beach reclamation at the site.

2.7.5 Lake Sihwa tidal power station

The largest tidal power station built to date is located at Lake Sihwa on the west coast of South Korea at the Yellow Sea, see Figure 2.10. In 1994 a 12.7 km long dam was constructed at the Sihwa Bay to separate an artificial lake from the sea. Its intended purpose was to act as freshwater storage for agricultural, industrial and recreational use, with a volume of $323 \times 10^6\,\mathrm{m}^3$ and a surface area of $56.5\,\mathrm{km}^2$ [54]. Due to severe water contamination, mainly from an adjacent industry complex, a decision was made to abandon its use as a freshwater reservoir and to allow for seawater exchange. The main reason for this was to restore the water quality in the lake, and a proposal for the production of clean energy was put forward as a secondary benefit of the modification. As result, a tidal power plant was integrated into the existing dam, with a construction time from 2004 to 2011 [46, 55].

The powerhouse accommodates ten bulb-turbines, each with a rated power of 25.4 MW and a runner diameter of 7.5 m, making the Lake Sihwa tidal power station the tidal barrage with the highest generating capacity to date [56]. The station generates around 553 GWh of electricity per year with a one-way flood generating mode.

The water level in the artificial lake must be kept one meter below the mean sea level, which rules out ebb or two-way generation [55].

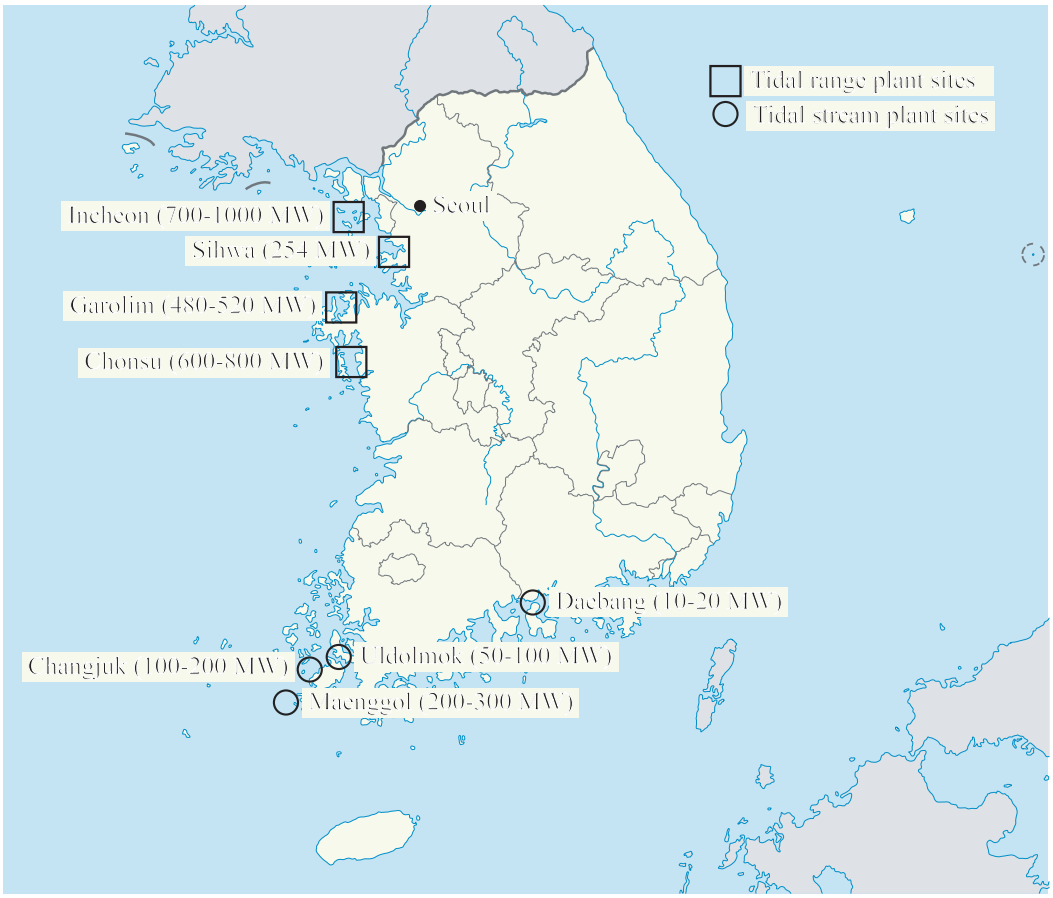

Figure 2.10: Potential sites of tidal range and tidal current power plants in South Korea, based on [55]

2.8 Prospective tidal power projects

Since the commissioning of the Lake Sihwa tidal power plant in 2011, no new facilities have been constructed to date. There are, however, plans for several large-scale tidal power projects, which are described in the following section.

2.8.1 Canada

Several projects have been proposed in the Bay of Fundy, Canada, where the tidal range is amongst the largest in the world. During spring tide, the tidal range can exceed 16 m [52]. From the 1970s, the first plans and assessments for constructing dams which would cut off sections of the bay were made. Two major basins, the Cumberland and the Minas Basin, were considered in 1986 [57], as depicted in Figure 2.9. The

power plant at the Cumberland Basin would have had 48 turbines with a combined rated output of 1.428 MW. In the Minas Basin, the proposed power plant would have had 128 turbines with a combined rated output of 5.338 MW [57]. However, studies indicated that these dams would alter the tidal amplitudes in the bay significantly, which was considered to be potentially hazardous to the neighboring ecosystems [52]. In more recent times, new concepts are on the rise and new plans to make use of tidal power in the Bay of Fundy have emerged, as is described in [58, 52].

2.8.2 United Kingdom

As shown in Section 2.3 the tidal power potential along the west coast of the United Kingdom has been very well studied and would allow for the construction of several economically feasible tidal power plants. Many plans have been made and rejected over the years. However, some of them are still in consideration and are presented in the following sections.

Severn Estuary

The Severn Estuary, which lies between the coasts of England and Wales, is the largest tidal range resource in the United Kingdom [59], see Figure 2.11. The tidal range is up to 14 m during spring tides at Avonmouth near Bristol [60]. Therefore many plans to build a dam between the Welsh and English coasts have been proposed in the past decades. Not only would such a dam provide for flood protection and a transport link, but according to [59], "The Severn's enormous tidal range could provide up to 5 % of our current electricity generation from an indigenous renewable source". Potential locations for the dam were assessed in several studies supported by the UK Department of Energy, beginning in 1975 [61].

In 1981, the Severn Barrage Committee investigated six proposed locations and recommended a barrage between Cardiff and Weston [42], which was further investigated by the Severn Tidal Power Group [62], the Sustainable Development Commission in 2007 [63] and the Department of Energy and Climate Change [64] together with the National Assembly of Wales [59] in 2010.

The project would consist of a dam with a length of 15.9 km that would create a basin with a surface area of 480 km^2 at mean sea level [8]. 216 turbines with a diameter of 9 m and a power of 40 MW would provide for a generating capacity of 8.640 MW and an annual energy output of 17 TWh. The operational mode of the power plant would be one-way ebb generation with pumping.

However, the DECC study concludes that "many years of further detailed work would be needed to plan, finance, and assess the impacts of such a large structure

Figure 2.11: Map of the Severn Estuary and its location in Great Britain

as a Severn power scheme before a case could be put forward for planning consent" [64]. Consequently, in 2010 the UK government scrapped the plans to build the power plant.

Swansea Bay

To make use of at least a part of the potential in the Severn Estuary, the technology of tidal barrages was replaced by a tidal lagoon which could be implemented in the Swansea Bay. Unlike the proposed tidal barrage schemes that block off the whole estuary, a dam that is shaped like a horseshoe with a length of 9.5 km is projected to extend from the coast near Swansea to enclose a tidal lagoon with an area of 11.5 km^2 [25]. The tidal range at the location is 10.5 m and with 16 installed bulb turbines the combined rated output would reach 320 MW. The operating scheme was projected to be a two-way scheme with pumping, generating roughly 530 GWh annually. The proposed concept would not block off the estuary and for this reason environmental impacts would be much lower. Since the number of turbines and sluices would be fewer, the initial investment costs would also be much lower, which makes this project an interesting case for private investors. The Hendry review, an independent review commissioned by the UK government, comes to the conclusion that the construction of a tidal lagoon in the Swansea bay should be considered: "Moving ahead with a pathfinder lagoon is, I believe, a no-regrets policy" [65].

Eastern Irish Sea

Apart from the large-scale concepts in the Severn Estuary, several other locations on the west coast of the United Kingdom are potential locations for tidal range power plants, such as the Mersey barrage, which was first proposed in the 1970's [66]. These projects would not only be interesting on their own, but the combination and conjunctive operation of the multiple sites could have the benefit of creating a longer generation window from tidal power, as the tidal cycles along the coast are phase shifted in time. This idea is proposed by [17] as a case study, where five tidal barrages, located at the Solway Firth, the Morecambe Bay, and the Mersey, Dee, and Severn estuaries are combined. In total, this scheme with an installed capacity of 21 GW could produce 33 TWh of electrical energy per year, which is at least 10 % of the annual electricity demand of the United Kingdom.

2.8.3 South Korea

After the successful implementation of the Lake Sihwa tidal power station in South Korea, many more tidal power locations along the country's coasts were suggested. Figure 2.10 gives an overview of the suggested tidal range and tidal stream projects along with estimates on possible installed capacities. The most advanced plans have been proposed by the state-run Korea Hydro & Nuclear Power (KHNP) for the Incheon tidal power plant that is located close to Lake Sihwa. The planned power station implements 44 turbines, each with a capacity of 30 MW. Thus the total installed power of 1.320 MW would make it the largest tidal power plant worldwide [67]. The construction of the facility was halted in 2012 after growing concerns over large impacts on the surrounding environment. Saller schemes could be implemented and have been suggested at the Garolim and Ganghwa bays, with installed capacities of 520 and 840 MW [67].

2.8.4 China

Although the tidal amplitude along the coasts of China does not reach the peak values of other locations around the world, several large-scale tidal power plants have been proposed. [68] presents a case study for four project sites that could together create an annual output of 402 GWh with an installed capacity of 159 MW.

2.9 Environmental considerations

The construction of a dam across an estuary creates large changes in its surrounding environment. The tidal cycle in the basin is necessarily altered to facilitate generation of electricity. The water level in the basin will no longer follow the natural cycle anymore but will instead follow a cycle induced by the operation of the tidal power plant. During waiting times the water level can stay constant for longer periods than it would in a natural cycle. The changes of the water level and flow patterns potentially have, among other things, the following effects:

- limitation of fish migration
- shift of the tidal cycle inside the basin in amplitude and time
- deposition of sediments within the basin
- alteration of the salinity and turbidity of the water in the estuary
- reduction of the area of the intertidal zone
- influence on tidal currents

Research on environmental impacts has been intensively conducted in the ecosystems of existing tidal power plants [8, 50, 63, 69, 70]. The ecosystem in the Kislaya Guba bay, for example, is considered to be ecologically stable; however, it is not the same as it was before the construction of the power plant, as new biological conditions are present. One example is strong desalination, which occurs in years of unusually high water levels, e.g. 1996 [71]. Problems with fish migration can be solved by the construction of pass facilities as described in [72]. Newly built structures such as dams, powerhouses and sluices can create new habitats for marine life and birds. Firstly bacteria accumulate on surfaces and form a microbial biofilm. Several days later algae, fungi, and protozoa grow on top of the biofilm and after few weeks a process referred to as macrofouling starts, where larger invertebrates such as mollusks and crustaceans as well as macroalgae such as seaweed accumulate [73]. Biofouling on periphery structures such as the dam does not have detrimental effects, but it decreases the discharge flowing through turbines and moreover lowers their efficiency [74]. Methods referred to as antifouling technologies can be used to limit the extent and pace of biofouling. There are special antifouling coatings and paints but their environmental impact varies widely [73]. An alternative is chlorine protection, which is considered highly effective with little environmental impact [74].

Tidal lagoons are a new concept where a basin is erected not in a coastal estuary but as a ring dam close to the shore, either as a coastal tidal lagoon or located freely in the ocean, i.e. as an offshore tidal lagoon. This concept is considered to have a lower

environmental impact than conventional tidal barrage schemes. Tidal lagoons create little to no change in the tidal amplitude in an existing river estuary [8], and moreover, they also avoid the problem of ship passages and migrating animals. However, to date, no tidal lagoon has been implemented.

The environmental impact of tidal barrage power plants differs from location to location and depends on the operation strategy [8]. A general statement cannot be made and is also not within the scope of the present work.

2.10 The new tidal turbine concept

From the evaluation of the tidal energy potential and different operating modes, it is clear that advancing the technology can facilitate the implementation of future projects and increase their output, thus accelerating the transition from nuclear and fossil-fuel to renewable energy sources. An efficient four quadrant operation is especially suitable and can make projects more flexible and economically more favorable, as described in Section 2.5. For a successful and economically reasonable operation, turbines capable of four-quadrant operation are required.

The proposed turbine concept, which is based on a reversing cylinder, claims to fulfill this requirement. For the implementation into a reversing cylinder, a speed variable axial turbine with fixed runner blades was identified as the best turbine type, after careful assessment of different alternatives. The space limitation imposed by the cylinder is one of the main considerations in the development of the turbine. A turbine with rim generator configuration, also referred to as Straflo turbine, is best suited for this application, as it allows for a large generator capacity without the need for a large generator bulb. Moreover, with the generator being arranged in a very central position, the space within the reversing cylinder is used in a very efficient way, making the turbine very compact. This allows for a relatively large runner diameter with respect to the diameter of the reversing cylinder.

In traditional Straflo turbines, the generator rotor is kept dry by a complex dynamic sealing system that prevents water from entering. With large diameters, the sealing system is split into several rubber segments that are hydraulically pushed against a hardened rotating surface. For smaller diameters, lip seals are used [2]. Their service life is approximately 20,000 h, after which they have to be replaced [40]. A regulated loading of filtered sealing water protects the seal surfaces from excessive wear by suspended sediments in the seawater [2]. As the sealing system is complex and requires frequent restoration, especially in cases where sand enters the sealing gap, in recent years research has been conducted into ways to minimize abrasion problems

[41]. In the present design, the generator rotor is completely surrounded by water to avoid the need for dynamic seals. A similar concept has proven to be feasible and is used for hydro turbines in applications where space is limited [75]. Figure 2.12 depicts the general layout of the turbine.

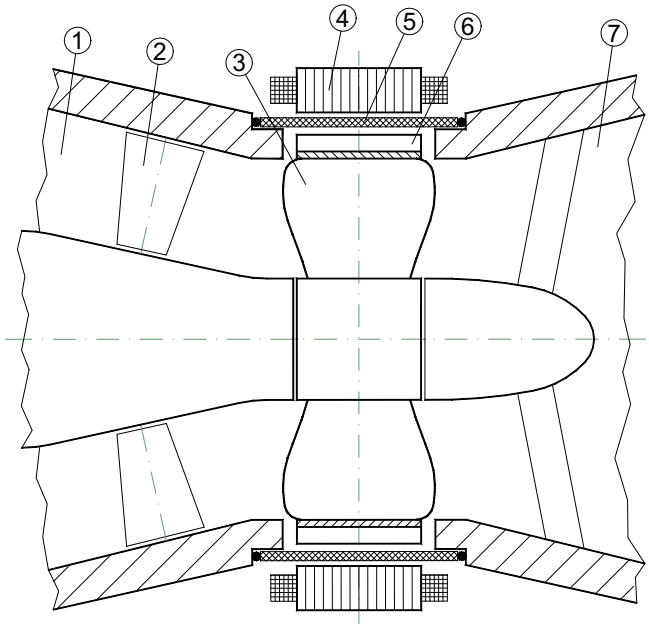

Figure 2.12: Meridional section through the turbine runner and generator [76]

Water flows through the intake of the turbine (1) and then passes the guide vanes (2). The generator rotor carries a set of permanent magnets (6) and is directly mounted on the tip of the runner blades (3). A thin-walled tube (5) is placed in between the generator rotor and stator and acts as a static seal. It prevents the generator stator (4) and its windings from contact with water. Downstream of the runner, the flow is decelerated in the draft tube (7).

In order to demonstrage the principal feasibility of the concept and to identify strengths and weaknesses, as well as specific challenges, a functional turbine was developed. The methods used in the development are described in the following chapter.

Chapter 3

Methodology

As a first step in developing a functional and efficient turbine based on the Straflo design, a hydraulic geometry had to be designed. From this, a mechanical design was derived in a second step. Apart from building on experience and the literature, the method selected to find satisfactory shapes for the runner, guide vanes, and draft tube, was computational fluid dynamics (CFD), which is the study of fluids in motion by simulation with computers. The physical laws governing flows are quite complex and can be described using the Navier-Stokes equations. This set of partial differential equations can be solved numerically on a computational mesh of small volumes. With this method, hydraulic machines can be modeled and optimized on the computer before an actual model turbine is manufactured.

One of the main advantages of CFD is that one can obtain insights into fluid flows without the need for measuring devices. This means that flow variables can be determined at any location and at as many locations as desired, and even in places that may not be accessible to measurement instruments. The determination of flow values can be accomplished without disturbance of the flow by measuring instruments. Once simulations are fully converged and thus completed, their results can be studied in many different ways, repeatedly and long after completion.

CFD is especially useful for designing hydraulic machines, as it facilitates the study of different designs and allows the researcher to select the most promising design before building a costly model device for experimental testing. It has to be stated, however, that CFD also has many limitations and has to be employed very carefully. The results of simulations can never be trusted blindly as some errors always occur. These are:

- Numerical errors, due to finite approximations
- Modeling errors, due to modeling of true physical processes, such as turbulence and the boundary layer

- Assumptions on boundary conditions
- Geometry errors, such as the roughness
- Simplifications, e.g. the assumption of steady flow

A detailed summary of the limitations of turbomachinery CFD with examples of the above-mentioned errors is given in [77]. The author states, however, that "Despite these limitations CFD remains an extremely valuable tool for turbomachinery design", which proved to be true in the present work. A detailed description of the numerical simulation theory and the simulation setup is given in Sections 3.2 and 3.3.

3.1 Turbine theory

In this section, the working principle of hydraulic turbines is explained and the corresponding theory is presented. According to Newton's second law an acceleration a of a mass m, i.e. a change of its momentum, is directly proportional to a force F. Moreover, the change in momentum takes place in the direction of the force.

Pumps make use of this principle by accelerating a flow through the application of a force, or rather torque, with the blades of a rotating impeller, while mechanical work is applied. The accelerated flow is usually decelerated shortly thereafter in a stationary guide vane apparatus, where velocity is converted into pressure.

Turbines apply the principle in reverse, as the available pressure is converted into velocity in the intake and the stationary guide vane apparatus where a circumferential velocity component c_u is created. The blades of a rotating runner then deflect the flow again while a torque is created that acts on the runner. This torque, in combination with the rotation of the runner, creates mechanical power P_{me}.

3.1.1 Euler head

The performance of a hydraulic turbine or pump can be quantified with Euler's turbine and pump equation, which was introduced in 1754 [78]. It is based on the conservation of angular momentum and relates the flow velocities in the runner to the specific power that is taken out of the fluid (turbine) or put in (pump) [79]. It reads

$$Y_{th} = H_{th} \cdot g = u_2 \cdot c_{u2} - u_1 \cdot c_{u1} = \Delta(u \cdot c_u) \quad [\mathrm{J/kg}], \tag{3.1}$$

where Y_{th} [J/kg] is the specific theoretical supply, H_{th} [m] is the theoretical pressure head, g [m^2/s] is the gravitational acceleration, c_{u1} and c_{u2} [m/s] are the circumferential components of the absolute velocities at the inlet and outlet respectively and u_1 and u_2 [m/s] are the blade velocities at the inlet and outlet respectively.

In the following, the energy transfer from a fluid flow onto a turbine blade is explained by example. Figure 3.1 depicts the idealized, i.e. frictionless, flow around an axial turbine blade. Positions are denominated with numbers in order of increasing pressure. This means that in turbine mode the values of the numbers decrease along the flow path through the turbine and in pumping mode, the numbers increase along the flow path.

The circumferential velocity of the runner blade u depends on the angular velocity ω and the distance from the rotational axis r. This distance can be expressed by the span S, which is the normalized distance from the minimum radius of the turbine blade to the maximum radius. Locations with $S = 0$ are directly at the hub and locations with $S = 1$ are directly at the shroud. The circumferential velocity u is low at $S = 0$ and increases with the distance from the rotational axis. Its maximum value is at the tip of the blades, i.e. at $S = 1$.

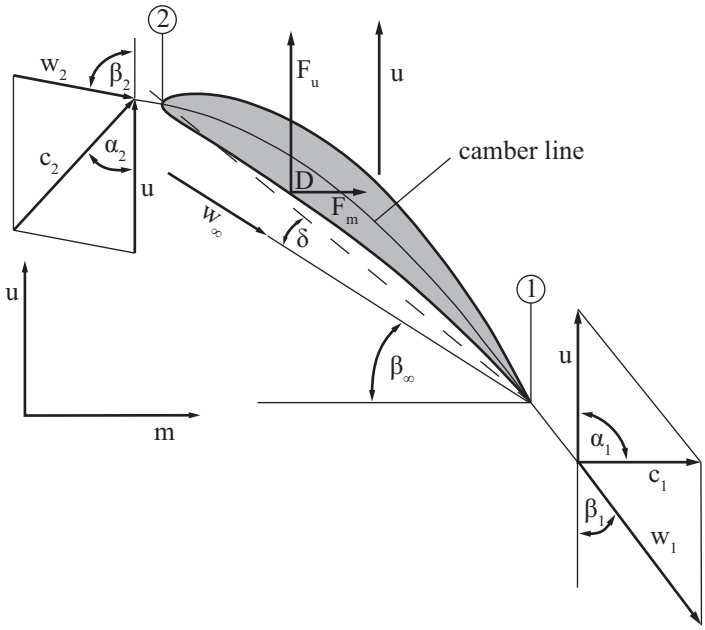

Figure 3.1: Blade of an axial turbine; flow velocities and forces, based on [79, 80]

The absolute flow velocity c is the flow velocity with respect to a fixed coordinate system, i.e. when the turbine is viewed from outside. The relative flow velocity w is the flow velocity with respect to a coordinate system that moves with the turbine runner, i.e. in the circumferential direction. Position 2 is on the leading edge of the blade, where the flow approaches the blade with the absolute velocity c_2. At the trailing edge, i.e. at position 1, the absolute velocity is c_1. The specific energy of the fluid at positions 1 and 2 is $c_1^2/2$ and $c_2^2/2$, respectively. The difference in the magnitudes of the specific energies $c_2^2/2$ and $c_1^2/2$, together with the mass flow rate $\dot{m}$

gives the theoretically transferred power P_{th} [79]:

$$P_{th} = \dot{m} \cdot \Delta Y_{th} = \dot{m} \cdot \left(c_2^2/2 - c_1^2/2\right) \quad [\mathrm{W}] \tag{3.2}$$

The deflection of the flow can be expressed by the change in the circumferential components of the absolute velocity from c_{u2} to c_{u1}, which creates a pressure difference that results in a force F_u on the blade in the circumferential direction. Greater values for the deflection create a higher force and therefore torque M. In this example, c_{2u} has a finite value, which is induced by the guide vanes and c_{1u} at the trailing edge is zero. In an ideal turbine, the circumferential component of the flow behind the blades is small or zero, as this means that the downstream flow has a low exit swirl and therefore low energy losses.

The relative flow velocity w is a result of a combination of the absolute flow velocity c with the circumferential velocity u. Ideally, the flow approaches the blade at the leading edge (2) without inclination of the vector w_2 towards the camber line of the blade. An angle between the real approach flow β_2 and the blade angle of the camber line at the leading edge β_{s2} is referred to as an incidence angle [81]. A condition in which the incidence angle is zero is referred to as shock free. The angle β_1 between the relative flow vector leaving the blade w_1 and the blade angle of the camber line at the trailing edge β_{s1} is referred to as the deviation angle.

The meridional velocity c_m is the velocity component of the absolute velocity c that points perpendicularly to each cross-section of the turbine. Together with the cross-sectional area A, it defines the flow rate through the turbine and it is bound to continuity.

The blade profile has to be optimized in order to achieve small incidence and deviation angles on all spans. The curvature of the camber line defines the extractable Euler head, which should ideally be equal on all spans as well, in order to prevent compensation currents. Another factor of the blade profile design is its thickness distribution. It determines the ratio of the lift force F_u and the drag force F_m. It also has an influence on the onset of flow separation, which must be avoided. In axial turbines, where the circumferential velocity u is directly proportional to the radius of the runner r, the Euler head $u \cdot \Delta c_u$ is directly proportional to $r \cdot \Delta c_u$.

3.1.2 Unit values and scaling laws

For the representation of the turbine performance characteristics at different operating points the unit quantities Q_1' and n_1' are used. These values represent the characteristics of a geometrically similar turbine with a runner diameter of $D_E = 1\,\mathrm{m}$, operating at a head of $H_E = 1\,\mathrm{m}$. This allows for a comparison of different turbine types and

sizes and different operating points [82].

Unit discharge

The unit discharge Q'_1 is defined as

$$Q'_1 = \frac{Q}{D^2 \cdot \sqrt{H}} \cdot {D_E}^2 \cdot \sqrt{H_E} \quad [\mathrm{m^3/s}], \tag{3.3}$$

where Q [$\mathrm{m^3/s}$] is the discharge through the turbine, D [m] is the runner diameter of the turbine, H [m] is the hydraulic head, D_E is the unit diameter of 1 m, and H_E is the unit head of 1 m. The unit discharge can range from $Q'_1 = 0.1\,\mathrm{m^3/s}$ in the case of Pelton turbines up to $Q'_1 = 3\,\mathrm{m^3/s}$ in the case of Kaplan bulb turbines.

Unit speed

The unit speed n'_1 is defined as

$$n'_1 = \frac{n \cdot D}{\sqrt{H}} \cdot \frac{\sqrt{H_E}}{D_E} \quad [\mathrm{min^{-1}}], \tag{3.4}$$

where n [$\mathrm{min^{-1}}$] is the rotational speed of the runner. The ideal unit speed of Pelton turbines is $n'_1 = 42.3\,\mathrm{min^{-1}}$, while Francis turbines have a typical unit speed of $n'_1 = 80\,\mathrm{min^{-1}}$ and Kaplan turbines have a typical unit speed of $n'_1 \geq 100\,\mathrm{min^{-1}}$.

Specific speed

The specific speed of a hydraulic machine can be expressed in two forms, n_y, and n_q. The dimensionless value n_y corresponds to the rotational velocity n of a specific hydraulic machine in 1/s. The machine is scaled geometrically in size and its rotational speed so that it operates with a discharge of $Q = 1\,\mathrm{m^3/s}$ and a specific work of $\Delta Y = 1\,\mathrm{m^2/s^2}$. It is defined as

$$n_y = n \cdot Q^{1/2} \cdot \Delta Y^{-3/4} \quad [–]. \tag{3.5}$$

The factor n_q is very common in the field of hydraulic machines, but with a unit of 1/min, it is not dimensionless. This is a constraint for using it as a characteristic number. It specifies the rotational speed at which a turbine operates with a discharge of $Q = 1\,\mathrm{m^3/s}$ and a head of $H = 1\,\mathrm{m}$. It is defined as

$$n_q = n \cdot \frac{Q^{1/2}}{H^{3/4}} \cdot \frac{{H_E}^{3/4}}{{Q_E}^{1/2}} \quad [1/\mathrm{min}], \tag{3.6}$$

where Q_E is the unit discharge of $1\,\mathrm{m^3/s}$. The two parameters n_y and n_q are numerically correlated with the ratio being [79]

$$n_q \approx 333 \cdot n_y \; [1/\mathrm{min}]. \tag{3.7}$$

In the present work, n_q is used rather than n_y as it has a more intuitive range.Hydraulic turbines can be grouped together depending on the field of operation and arranged in a chart, see Figure 2.7. Typical specific speeds range from $n_q = 1$ in the case of multi-nozzle Pelton turbines, over Francis turbines with intermediate values of $n_q = 20$–100, Kaplan turbines with $n_q = 100$–250 and up to $n_q = 500$ for Kaplan bulb turbines. Generally, higher specific speeds lead to smaller turbine dimensions, a higher rotational speed of the generator, and reduced costs.

Theoretically, all types of turbines can be sized so as to work with the desired discharge and head given by a specific location. Then, however, to operate the turbine at its specific speed n_q, the real rotational speed of the turbine n has to be adjusted accordingly.

The upper boundary of n for each turbine type is defined by the structural strength of the runner and by cavitation. On the other hand, the lower boundary is established on the basis of economic considerations, as the dimensions and therefore costs of the turbine and generator rise with lower rotational speeds. These limits mean that for any head, the specific speed n_q is chosen as high as possible, in order to obtain a high power density. Thus, turbines with low specific speeds are typically used in high head applications, whereas turbines with high specific speed are used in low head applications.

Head and flow coefficient

Water pumps can be characterized by plotting the relation between the discharge Q and the hydraulic head H as shown in Figure 3.2. A pump reaches its maximum head when the discharge is zero and reaches its maximum delivery discharge when the hydraulic head is zero. The progression of the delivery head between these two operating points is referred to as characteristic curve or head curve and depends on the geometry of the impeller and thus the specific speed. Pumps with a high specific speed generally have a steep head curve. Each point on the head curve is an operational point at which the pump can work. The efficiency of the pump varies along the curve and can be shown in a second graph.

To obtain a dimensionless representation of the head curve, the underlying quantities can be converted according to the laws of similitude. The head can be represented by the head coefficient

$$\psi = \frac{\Delta Y}{u_2^2/2} \quad [–], \tag{3.8}$$

which is dependent on the specific work ΔY and the circumferential velocity of the runner blade tips at the outlet u_2.

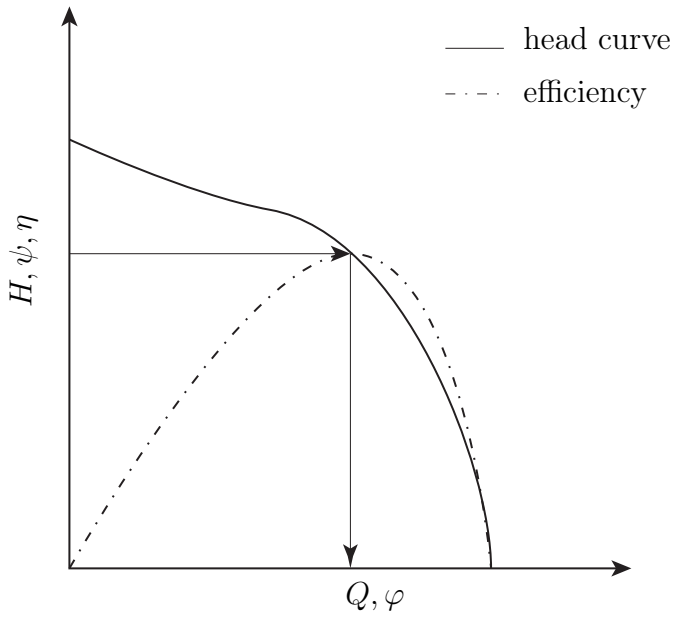

Figure 3.2: Head curve of a centrifugal pump

The flow rate can be represented by the flow coefficient

$$\varphi = \frac{8 \cdot Q}{\pi \cdot D^3 \cdot \omega} \quad [-], \tag{3.9}$$

which is dependent on the flow rate Q and the rotational speed n of the runner, as well as the runner diameter D.

Upscaling and uprating of turbines

The operating conditions, efficiency and cavitation characteristics of hydraulic turbines are usually measured in model tests before a prototype turbine is built. This is done to verify the design and to find possible flaws. A model turbine with a runner diameter of approximately $D = 0.34\,\mathrm{m}$ is manufactured according to the hydraulic design, i.e. in strict geometrical similitude. The smaller scale saves costs on the turbine itself as less material is needed and it can be manufactured on smaller machines. Moreover, the test rig on which the tests are performed is smaller as well, and less electrical power is needed during measurements.

In order to obtain valid values, it is important to measure the model turbine using the operating points that the prototype will be working with, i.e. the kinematic similitude has to be maintained. To do so, the dimensional values flow rate Q_P, head H_P and speed n_P of the prototype are converted into the unit values Q'_1 and n'_1. From them the dimensional values for the model tests Q_M, H_M and n_M can be derived. Table 3.1 gives values for the conversion between model and prototype scale.

When water is used in the model test it is not possible to maintain dynamic similitude, i.e. parameters such as the Reynolds-, Froude- and Weber-number are

different. Due to the smaller scale of the model turbine, it would be necessary to use a fluid with a smaller viscosity or to use extremely high speeds in order to keep the Reynolds number constant. As neither of these options is practicable, model tests are conducted at a Reynolds number which is lower than that of the prototype. This leads to a measured model efficiency that underestimates the efficiency of the prototype scale. To correct this, a process referred to as uprating is carried out and is standardized and defined according to the standards of the IEC [83]. The standard also specifies how to correctly carry out model tests of hydraulic machines.

Table 3.1: Example conversion from model scale to prototype scale

	H [m]	Q [m^3/s]	n [1/min]	D [m]	Q_1'[m^3/s]	n_1' [1/min]
Model	3.0	0.475	900	0.34	2.37	176.7
Prototype	3.0	36.98	102	3.00	2.37	176.7

3.1.3 Runaway speed

During normal operation, the rotational speed n of the turbine runner is kept in a specified range by the generator. The torque M created by the turbine blades is counteracted by the load, which is the torque generated by the magnetic forces within the generator. In the case of a power outage or a similar disturbance, the turbine torque is no longer counteracted and the runner speeds up until it reaches runaway speed n_d, which is much higher than the operational speed n.

The turbine has to be designed so as to withstand the extraordinarily high centrifugal forces that occur during a runaway condition, even when the hydraulic head has its maximum magnitude. TO ensure that all rotating parts remain intact, the yield strength of the materials used must not be exceeded. Moreover, the deformation of components must be considered so as to prevent jamming and subsequent failure. Eventually, the turbine has to be slowed down as fast as possible and halted, which can be done by stopping the flow. This can be done by closing the distributor or other protective devices. Turbine runaway is not a frequent condition, especially in Europe, but in the United States of America, several instances have been reported that caused considerable damage [84].

The magnitude of the runaway speed depends on the turbine type and is given in Table 3.2 as a ratio of n_d and n. The turbine used in the Annapolis tidal power plant has a nominal rotational speed of $n = 50\,\mathrm{min}^{-1}$ and a runaway speed of $n_d = 98\,\mathrm{min}^{-1}$, which comes close to a factor of 2. The runaway speed of a turbine can be simulated, but for this, the final geometry of the turbine has to be known

Table 3.2: Runaway speed of different turbine types [79, 85, 31]

Turbine type	n_d/n
Pelton	1.8–1.9
Francis	1.6–2.1
Kaplan	2.2–2.8

and, moreover, parameters such as the bearing friction have to be known. Due to these restrictions, the runaway speed was is numerically determined and is instead estimated using the literature values presented in Table 3.2.

3.1.4 Efficiency

The efficiency of a machine, defined as the ratio of useful output to total input, gives a measure of how efficiently the machine transforms power or energy from one state into another. In hydraulic machines, the conversion is from hydraulic power to mechanical power or vice versa. The direction of conversion has to be taken into account in the calculation. For a turbine, the input power is the hydraulic power and the output power is the mechanical power. The equations read

$$\text{for turbines}: \quad \eta = \frac{M \cdot \omega}{\rho \cdot g \cdot Q \cdot H} \quad [-] \tag{3.10}$$

$$\text{for pumps}: \quad \eta = \frac{\rho \cdot g \cdot Q \cdot H}{M \cdot \omega} \quad [-] \tag{3.11}$$

where Q [m^3/s] is the flow rate, H [m] is the head, ω [rad/s] is the angular velocity of the runner and M [kg m^2/s^2] is the torque. The difference between the input and output power is the sum of all losses that arise in the machine, which are described in detail in the following section. In the international standard for turbine model acceptance tests IEC No. 60193, the International Electrotechnical Commission (IEC) stipulates that the head H is calculated from the difference in absolute pressure, the mean velocity $\bar{c}$ and the geodetic height z on the reference in- and outlet-sections 0 and 1 [83]:

$$H_{IEC} = \frac{p_0 - p_1}{\rho \cdot g} + \frac{\bar{c_0}^2 - \bar{c_1}^2}{2 \cdot g} + z_0 - z_1 \quad [\text{m}] \tag{3.12}$$

When the cross-sectional area of the reference sections is equal, i.e. $A_0 = A_1$, the resulting mean velocities $\bar{c_0}$ and $\bar{c_1}$ are equal. In the case of an axial turbine with a horizontal axis the geodetic heights z_0 and z_1 are equal as well and the head can then be calculated from the difference in static pressure p on the reference planes:

$$H_{IEC} = \frac{p_0 - p_1}{\rho \cdot g} \quad [\text{m}] \tag{3.13}$$

3.1.5 Losses

Losses decrease the efficiency of turbo machines as they reduce the amount of power that is converted into electricity. They can be grouped into two main categories: inner losses and outer losses [79]. The former category describes all losses that arise from friction in the working fluid and generate thermal energy, i.e. through dissipation. The latter includes all mechanical losses that are introduced by friction in the bearings and seals, and, if applicable, by air friction on the coupling and drive shaft, as well as the power needed for auxiliaries. Another loss occurring is the exit loss, which is evaluated separately. The outer losses depend to a great extent on the mechanical design of the turbine bearings and seal system, which depends on the size of the turbine and the specific conditions of the projected site. Thus in the present work, outer losses, with the exception of the exit loss, were not considered and the turbine was optimized by reducing inner losses as much as possible.

Inner losses are referred to as hydraulic losses in the context of water turbines, as water is the working fluid. Their main contributors are:

- Profile losses, i.e. at the guide vanes and runner blades
- Shock losses
- Leakage losses, i.e. volume losses through the gaps
- Gap friction losses, i.e. friction losses in the generator gap

Alternatively, the losses occurring in the individual turbine sections can be quantified separately by conducting a loss analysis. This was carried out for the main components of the turbine, i.e. the inlet structure, the guide vanes, the runner and the draft tube. For each component, the difference in total pressure p_t between the inlet and outlet was computed:

$$\Delta H_{in} = \frac{p_{t,inletInlet} - p_{t,inletOutlet}}{\rho \cdot g} \quad [\text{m}] \tag{3.14}$$

$$\Delta H_{gv} = \frac{p_{t,gvInlet} - p_{t,gvOutlet}}{\rho \cdot g} \quad [\text{m}] \tag{3.15}$$

$$\Delta H_{ru} = \frac{p_{t,ruInlet} - p_{t,ruOutlet}}{\rho \cdot g} - \frac{M \cdot \omega}{\rho \cdot g \cdot Q} \quad [\text{m}] \tag{3.16}$$

$$\Delta H_{dt} = \frac{p_{t,dtInlet} - p_{t,dtOutlet}}{\rho \cdot g} \quad [\text{m}] \tag{3.17}$$

By dividing the total pressure difference ΔH of each component by the total head H_t, each head loss can then be normalized and be expressed as a percentage of the total head H_t. These relative losses subsequently are referred to as $H_{l,in}$, $H_{l,gv}$, $H_{l,ru}$, $H_{l,dt}$.

Profile losses

Profile losses can be attributed to the friction occurring on the surfaces of the runner blades and guide vanes. The friction and thus the losses increase with higher relative velocities between the surfaces and the flow. Thus, the rotational speed of the runner is one of the major factors contributing to profile losses and therefore should not be too high. Another factor is the profile length, as it has a direct influence on the area of the surfaces with friction. Shorter profiles generally have less frictional area and thus lower profile losses, however they are more susceptible to cavitation. Finding a good balance requires careful consideration.

Shock losses

Figure 3.3 a) depicts a situation where the relative flow velocity w_2 approaching the blade hits the blade camber line tangentially. This is referred to as shock-free entry and is achieved at the design point of a turbine. In an ideal case, the flow on all spans of the guide vanes and the runner blades is shock-free and there are no or only minor shock losses. This is usually true for a well optimized turbine in the rated operating point.

Shock losses occur at the leading edge of runner blades and guide vanes when the flow velocity is inclined to the blade profile. This is the case when the flow rate differs from the design flow rate or when the blades are not properly aligned. The forced, rapid change in velocity increases friction and in extreme cases leads to zones of flow separation with recirculation flow [79]. Both of these phenomena result in a pressure loss. If the operation flow rate is higher than the design flow rate the turbine is working in overload where the shock hits the pressure side of the blade and flow separations can occur on the suction side as depicted in Figure 3.3 b). In part load, when the operating flow rate is lower than the design flow rate the shock hits the suction side and flow separations can occur on the pressure side of the blade as depicted in Figure 3.3 c).

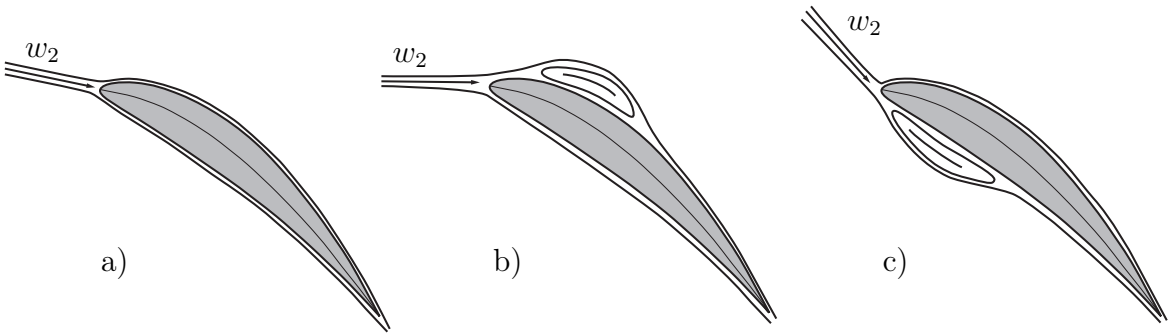

Figure 3.3: Illustration of shock losses. a) design flow b) overload c) part load

Leakage losses

A flow arises in gaps between surfaces when a pressure difference is present. That is, for example, the case with the gap between runner blades and the stationary shroud. In the present turbine design, there is a gap between the rotor and the stationary turbine housing. The flow through this gap reduces the flow rate of the working fluid through the runner. It is referred to as leakage flow and the resulting hydraulic loss is referred to as leakage loss. In a smooth axial gap, the gap flow rate number μ_{gp} is defined as

$$\mu_{gp} = 1/\sqrt{\lambda \cdot L_{gp}/(2 \cdot s_{gp}) + 1,5} \quad [–] \tag{3.18}$$

where L_{gp} [m] is the length of the gap, s_{gp} [m] is the width of the gap, and λ [–] is the friction coefficient.

The flow rate through the gap can be obtained from the pressure difference between the pressure at the inlet of the gap (p_i and pressure at the outlet of the gap p_o) together with the cross-section of the gap A_{gp} and the gap flow rate number μ_{gp}:

$$Q_{gp} = \mu_{gp} \cdot A_{gp} \cdot \sqrt{2 \cdot (p_i - p_o)/\rho} \quad [\mathrm{m}^3/\mathrm{s}] \tag{3.19}$$

Gap friction losses

Friction arises on all surfaces where shear flow exists. On stationary surfaces, this friction leads to a reduction of total pressure along the flow path. On rotating surfaces, the friction results in a torque around the axis of rotation. In hydraulic machines, this torque causes a loss of power and can have a significant effect. In the following, it is referred to as gap friction loss. In axial bulb turbines, the turbine runner is mounted on a shaft that transfers torque to the generator, which is housed in a bulb. The generator is usually surrounded by a gas, such as air, which has a very low viscosity in comparison to water. Thus the gap friction losses in the generator are low. Apart from this friction occurs at the hub, the blade surfaces and in the gap between the blade tips and the stationary turbine shroud.

In comparison, the frictional surfaces are much larger in axial turbines that possess a rim generator. The rim at the periphery of the runner blades that carries the generator rotor has a relatively large rotating area. When these areas are in contact with water the friction losses may be substantial. According to [40], they can be reduced by keeping the dimensions of the rim small and additionally "these purely frictional losses may all be majorated, i.e. for large dimensions and heads they become relatively less important". In conventional rim generator turbines, dynamic seals keep the outer part of the rotor dry. This is necessary due to the generator design and

it also reduces the area rotating against the water. The dynamic seals, however, are another source for friction, but "these losses are kept so low that they are significant only for machines of up to 5 MW output, within which range they vary between 0.1 % and 0.5 % [40]."

Exit loss

The flow velocity of the fluid leaving a turbine or pump stage is regarded as exit loss because the kinetic energy it contains is not utilized [79]. It is not possible to design a hydraulic machine with an exit velocity of zero, as the working fluid has to leave the machine. In low head water turbines, which usually consist of only a single stage, the kinetic energy at the runner outlet can be up to 50 %. This comes from the fact that low head turbines are designed to have a very high unit discharge Q_1' in order to achieve an adequate power density from the low specific energy of the flow, thus the transport velocity through the turbine is very high. However, the major part of this kinetic energy is converted into pressure in the draft tube. It is therefore very important that the draft tube fulfills its function properly and without large losses. Normally, the flow velocity at the draft tube outlet is reduced to approximately 20–25% of the velocity at the runner outlet. For low-head Kaplan-bulb turbines the flow velocity is reduced to approximately 1–2.5 m/s at the draft tube outlet.

According to [83] the mean velocity entering the turbine $\bar{c}_i$ and the mean velocity leaving the turbine $\bar{c}_o$ have a uniform distribution, i.e. a rectangular velocity profile. The magnitudes can be calculated from the flow rate and the cross sectional areas of the respective planes. The exit loss can then be calculated by

$$\Delta H_{ex} = \frac{(Q/A_o)^2}{2 \cdot g} = \frac{\bar{c_o}^2}{2 \cdot g} \quad [\text{m}]. \tag{3.20}$$

In reality, however, the velocity in the two reference planes is usually not uniform. In the draft tube for example, the velocities in the center are higher than at the draft tube walls and, depending on the runner design, there may exist a circumferential component c_u as well. This nonuniform velocity distribution results in a kinetic energy of the flow leaving the draft tube that is higher than that given by a calculation with a rectangular velocity profile. The difference between the two calculation methodologies can be quantified by an energy coefficient α that is defined as

$$\alpha = \int_A \frac{c^2 \cdot c_m \cdot dA}{\bar{c}^3 \cdot A} \quad [\text{–}]. \tag{3.21}$$

where c is the absolute flow velocity, c_m is the meridional component of the absolute flow velocity and $\bar{c}$ is the area averaged flow velocity. For a uniform velocity distribution α is 1 and for real flow it is always greater than 1.

According to [83] it is very time consuming in model tests and therefore impracticable to determine the velocity distribution of flow passing cross-sections and therefore it is conventionally agreed to assume that $\alpha = 1$. Although the difference between the accurately determined kinetic energy and the kinetic energy calculated from the area averaged flow velocity can reach 1 % to 2 %, it is usually agreed to disregard it in the evaluation of measurements. In the evaluation of CFD-simulations, it is easy to make an accurate determination of the velocity on reference planes.

For efficiency evaluations this means that according to [83] the velocity distribution on reference planes is assumed to be uniform, while in reality it is not. The higher kinetic energy of the flow leaving the turbine is contained in the head H_{IEC}. When the nonuniform velocity distribution is taken into account, the head H_t has to be calculated:

$$H_t = \frac{p_i - p_o}{\rho \cdot g} + \frac{c_i^2 - c_o^2}{2 \cdot g} + z_i - z_o = \frac{p_i - p_o}{\rho \cdot g} + \frac{\alpha_i \cdot \bar{c_i}^2 - \alpha_o \cdot \bar{c_o}^2}{2 \cdot g} + z_i - z_o \quad \text{[m]} \tag{3.22}$$

It can alternatively be calculated from the difference in total pressure, which yields the same result:

$$H_t = \frac{p_{t,i} - p_{t,o}}{\rho \cdot g} \quad \text{[m]} \tag{3.23}$$

Due to the consideration of nonuniform velocity distributions, the head based on the total pressure difference H_t is smaller than the head H_{IEC} defined by the IEC. This comes from the fact that the non-uniformity of the velocity is normally much greater in the diffuser than in the inlet section. An efficiency calculated with H_t is therefore higher than an efficiency calculated with H_{IEC}. The difference between H_{IEC} and H_t is referred to as modified exit loss $\Delta H_{ex,t}$ in the present work:

$$\Delta H_{ex,t} = H_{IEC} - H_t = \alpha_o \cdot \frac{\bar{c_o}^2}{2 \cdot g} - \alpha_i \cdot \frac{\bar{c_i}^2}{2 \cdot g} \quad \text{[m]} \tag{3.24}$$

A larger non-uniformity of the flow velocity leaving the turbine results in a larger α and thus a larger exit loss $\Delta H_{ex,t}$.

3.1.6 Cavitation

Cavitation is a phenomenon that occurs in fluids whenever the static pressure of the fluid falls below its vapor pressure. This is often the case when the fluid is rapidly accelerated or its path is rapidly deflected. In the low-pressure region, the fluid begins to form small bubbles of vapor that grow and travel downstream along the flow path. There, the static pressure might rise again and once it exceeds a certain value the vapor bubbles rapidly collapse while forming a jet. This is illustrated in Figure 3.4. The energy densities in this process can be extremely high and so are the local temperature

and pressure. When these implosions take place near solid surfaces, they are subject to very high cyclic stresses that over time lead to an erosion of the material. Moreover, cavitation creates strong vibrations and a loud noise.

Figure 3.4: Photograph of a liquid jet produced by a collapsing cavitation bubble [86].

In hydraulic machines, cavitation should be avoided, as the induced erosion can have an adverse effect on the efficiency and even lead to a total failure. Locations with high flow velocities and therefore low static pressure are most susceptible to cavitation. These are the leading edges of the runner blades, where the corresponding phenomenon is referred to as leading edge cavitation. Additionally, the suction side of guide vanes and runner blades can be affected by surface cavitation. Cavitation can also appear at the tips of the runner blades and at surfaces at the draft tube entry.

Therefore, cavitation has to be considered during the design of the hydraulic machine. The geometry has to be shaped in a way that changes in velocity are moderate and spikes of low pressure are avoided. This can be achieved by keeping the incidence angles of the flow approaching the blades low on all spans and by designing the leading edge of the runner blades with a sufficient roundness. Surface cavitation can be avoided by making the blade profiles long enough and thus reducing the pressure difference between the suction and pressure side under a specific Euler Head.

In a hydraulic machine, cavitation will occur whenever the local static pressure drops below the vapor pressure. Thus, for a given design of a pump or turbine, the occurrence of cavitation is strongly linked to the pressure level in the whole system, which depends on the pump or turbine head H and the suction head h_s. With a vertical axis Kaplan turbine, the suction head is defined as the vertical distance from the tailwater surface to the most cavitation-prone point within the turbine, i.e. the uppermost point of the runner circumference, see Figure 3.5.

Setting the machine lower with respect to the tailwater surface will reduce the likelihood of cavitation. This, however, is very costly, as it requires increased excavation

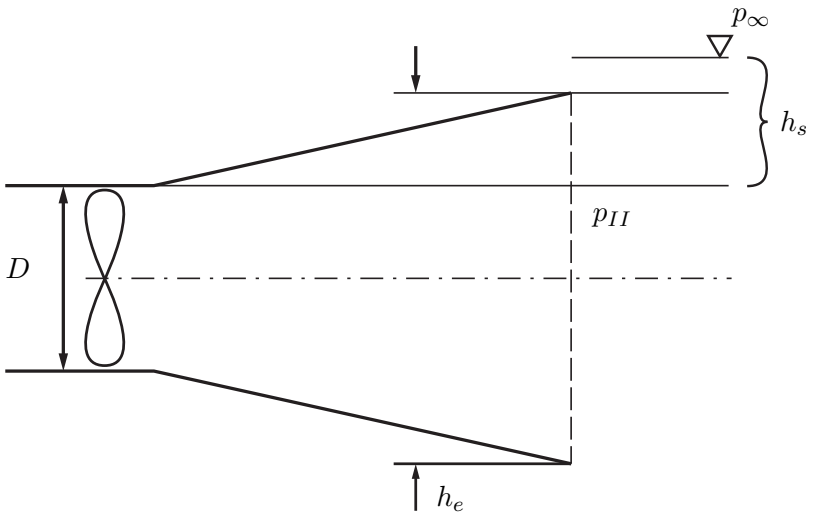

Figure 3.5: Definition of a setting to obtain σ_{plant}

depth during the construction of power plants.

Cavitation will occur when the dimensionless Thoma number σ is lower than the critical Thoma number σ_c:

$$\sigma = \frac{p_\infty - p_v - \rho g h_s}{\rho g H} < \sigma_c \tag{3.25}$$

where p_∞ is the static pressure at the tailwater surface, p_v is the vapor pressure and h_s is the suction head, i.e the elevation difference between the uppermost runner location and the tailwater level. The vapor pressure of water p_v is a function of the temperature; at $T = 25\,°\text{C}$ it is $p_v = 2073$ Pa. The critical Thoma number σ_c is a property of the specific machine design; a low figure of σ_c means that the machine has a low cavitation susceptibility. Due to the high flow velocities occurring in machines of high specific speed and high unit discharge, the critical Thoma numbers are usually higher in these machines. Figure 3.6 gives an overview of the numbers which can be typically achieved.

The onset of cavitation can be determined from numerical flow simulations if the pressure at the turbine outlet is known. This depends on the exact setting of the turbine, i.e. its installation depth with regard to the tailwater level. This setting is not defined a priori in the specific case and therefore the aim in the design process was to reduce pressure spikes at the leading edges and to achieve a design that has a low critical Thoma number σ_c, i.e. is rarely prone to cavitation. The blade length was chosen conservatively based on known designs to minimize the risk of surface cavitation occurring during operation. The critical Thoma number σ_c indicates when cavitation starts to arise. For a specific turbine design, σ_c has to be determined in model tests and from experience with existing turbines, where typical values are known. Values of σ_c are a function of the specific speed n_q of different turbines. Kaplan and bulb turbines

with a specific speed of $n_q = 260$ min^{-1} typically have a critical Thoma number of $\sigma_c = 1.1$–1.7, depending on their unit discharge Q_1' [82].

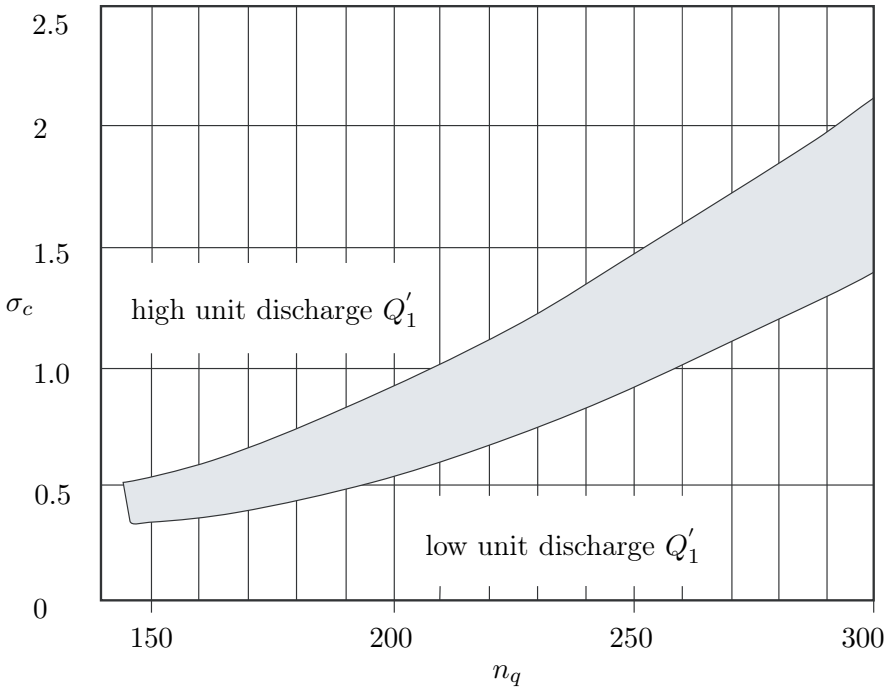

Figure 3.6: Critical Thoma number σ_c in relation to n_q [82]

3.1.7 Draft tube theory

The purpose of a draft tube is to form a connection between the turbine outlet and the tailwater and to reconvert the kinetic energy remaining in the flow at the turbine outlet into static pressure during the draft tube passage. The kinetic energy in a tubular turbine can be up to 50 % of the available head and without a draft tube, this energy would be lost at the turbine outlet [87]. To convert it into static pressure, the flow has to be decelerated. This is achieved by increasing the cross-sectional area along the stream path. Due to continuity, the flow velocity at a fixed flow rate has to decrease when the area increases. According to Bernoulli's law, this leads to an increase in pressure; thus the static pressure at the runner is lower than the pressure at the draft tube outlet, which in turn is determined by the tailwater level. Altogether, the draft tube increases the pressure difference across the runner and minimizes the outlet losses.

Figure 3.7 depicts a schematic view of a draft tube. The draft tube inlet is located at the beginning of the expansion and marked with i. The draft tube outlet is marked with o. The corresponding cross-sectional areas are A_i and A_o, respectively, and the flow velocities are c_i and c_o. The draft tube length L_{dt}, together with the draft tube

opening angle θ, defines the increase of cross-sectional area between draft tube inlet and draft tube outlet.

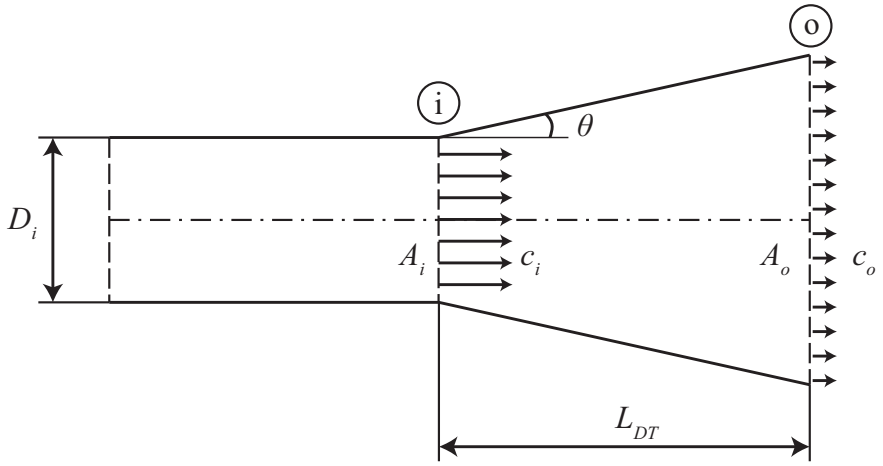

Figure 3.7: Schematic view of a draft tube, modified from [87]

The continuity equation specifies that the inlet flow rate is equal to the outlet flow rate. It reads

$$A_i \cdot c_i = A_o \cdot c_o. \tag{3.26}$$

It shows that a larger outlet area A_o results in a lower outlet velocity c_o. The area ratio m of the draft tube is calculated as the ratio of the inlet area and the outlet area

$$m = \frac{A_o}{A_i} \quad [–]. \tag{3.27}$$

By formulating Bernoulli's equation for the draft tube without friction, we see that a reduction in the outlet velocity c_o results in an increase in pressure p_o. The remaining kinetic energy of $\frac{c_o^2}{2}$ is lost and therefore c_o should be reduced as much as possible. The Bernoulli equation in this frictionless view reads

$$\frac{p_i}{\rho} + \frac{c_i^2}{2} = \frac{p_o}{\rho} + \frac{c_o^2}{2}. \tag{3.28}$$

By rearranging Equation 3.28 we get the equation for the ideal pressure recovery:

$$\Delta p_{ideal} = (p_i - p_o)_{ideal} = \frac{\rho}{2} \cdot \left({c_i}^2 - {c_o}^2\right) \quad [\text{Pa}] \tag{3.29}$$

By substituting the outlet velocity $c_o = c_i \cdot A_i/A_o = c_i \cdot 1/m$ we get

$$\Delta p_{ideal} = \rho/2 \cdot \left({c_i}^2 - \left(c_i \cdot \frac{A_i}{A_o}\right)^2\right) = \rho/2 \cdot {c_i}^2 \cdot \left(1 - \frac{1}{m^2}\right). \tag{3.30}$$

The area ratio of the draft tube m determines the ratio of flow velocities between inlet and outlet. In an ideal draft tube, the outlet velocity would be close to zero and all of the kinetic energy would be converted into static pressure. In this case, the draft

tube outlet would need to have an infinite area. The proportion of kinetic energy converted into pressure can be expressed by the pressure recovery coefficient c_p, which is calculated by the following equation:

$$c_p = \frac{(p_i - p_o)}{0.5 \cdot \rho \cdot {c_i}^2} \quad [–] \tag{3.31}$$

With a finite outlet area, there is a theoretical limit on how large c_p can get, which is referred to as ideal pressure recovery coefficient c_{pi} that is calculated with

$$c_{pi} = 1 - \left(\frac{A_i}{A_o}\right)^2 = 1 - 1/m^2 \quad [–]. \tag{3.32}$$

Table 3.3 lists the ideal pressure recovery coefficients c_{pi} for different draft tube area ratios.

Table 3.3: c_{pi} for different area ratios m [87]

m	1.5	2	3	4	5	10	∞
c_{pi}	0.555	0.75	0.89	0.937	0.96	0.99	1.0

With an area ratio of $m = 2$ in an ideal case, 75 % of the kinetic energy is converted into pressure, while at an area ratio of $m = 4$ over 90 % of the kinetic energy is converted. Area ratios of 5 and more only give a very small additional pressure gain and therefore the area ratio of real draft tubes is in a range of 3 to 5.

In a real scenario, where friction is present and the deceleration is not uniform, the real pressure recovery is lower than the ideal pressure recovery. Reasons for this can be flow separations, nonuniform velocity distribution and friction losses at the draft tube walls.

$$c_p = \frac{p_o - p_i}{\rho/2 \cdot {c_i}^2} \quad [–] \tag{3.33}$$

To account for these effects and to evaluate the draft tube quality one can calculate the draft tube quality grade η_{dt}:

$$\begin{aligned} \eta_{dt} = \frac{c_p}{c_{pi}} = \frac{\Delta p_{real}}{\Delta p_{ideal}} = \frac{p_o - p_i}{\rho/2 \cdot ({c_i}^2 - {c_o}^2)} = \frac{p_o - p_i}{\rho/2 \cdot {c_o}^2 \cdot (1 - {c_o}^2/{c_i}^2)} = \\ = \frac{p_o - p_i}{\rho/2 \cdot {c_i}^2} \cdot \frac{1}{(1 - 1/m^2)} \quad [–] \end{aligned} \tag{3.34}$$

The area ratio m achievable at a given length L_{dt} is proportional to the opening angle θ of the draft tube, where higher opening angles result in larger area ratios. However, if the opening angle is too steep, flow separations can occur that effectively limit the cross-sectional area of the flow. The draft tube length L_{dt} is limited, as longer draft tubes are more costly than short ones. Additionally, the sum of friction losses at the

draft tube walls is higher the more wetted area a draft tube has. Finding a good balance between area ratio m, opening angle Ω and draft tube length L_{dt} is a delicate task. The goal is to find a shape where the length is as short as possible in order to keep the friction losses low, with a large area ratio in order to reduce the exit losses, while still maintaining stable flow conditions, i.e. avoiding flow separations [87][88].

3.2 Computational fluid dynamics theory

The simulations in this study were carried out using the software package ANSYS. The simulation projects were created and managed using ANSYS Workbench and the simulations were carried out using ANSYS CFX, which itself is structured into four software modules [89]. CFX-Pre is a pre-processor and allows the user to import meshes, define simulation parameters such as boundary conditions, initial values, and settings for the CFX-solver. CFX-Solver Manager provides a graphical user interface to interactively monitor equation residuals and flow properties and it also allows the user to control and modify simulation runs. Moreover, it acts as a job manager and prepares the CFX-solver for parallel calculations [90]. ANSYS CFX-Solver is a coupled solver, which means that it solves the hydrodynamic equations for three components of the flow velocity u, v, and w and the pressure p simultaneously. This is in contrast to segregated solvers where the momentum equations are solved first and the pressure is obtained afterwards. Coupled solvers have a higher memory demand than segregated solvers, but reach convergence with fewer iterations. Moreover, implicit solvers can be numerically stable independently of the Courant number. The set of equations solved by ANSYS CFX are the unsteady Navier-Stokes equations in their conservation form. The discretization scheme is an element-based finite volume method. The solver computes quasi-steady or transient simulations, which after completion can be analyzed with the post-processing module CFD-Post. This allows the user to calculate quantitative information by defining variables and expressions and has facilities for creating plots and diagrams.

The hardware used for the simulations was a workstation with a CPU with six physical cores (Intel Core i7-3930K@3.2 GHz) and 32 GB of memory, as well as a server with 20 physical cores (dual Intel XEON E5-2687W v3 @ 3.1 GHz) and 64 GB of RAM. A total of 245 ANSYS workbench projects were created in the course of the Safe*Coast project, with more than 1500 simulation runs in total. However, some of these were not created specifically for the optimization, but were used to check different simulation settings and techniques.

The main purpose of the numerical simulations was to optimize the turbine geom-

etry in order to achieve high efficiencies and a high unit discharge in both the turbine and pumping mode. While the goal was to predict the overall characteristics as reliable as possible, no data was available during the optimization process that could be used to calibrate and validate the simulations, mostly because the new turbine concept is very individual.

Thus, assumptions for boundary conditions like inflow turbulence intensity, wall roughness, and turbulence settings had to be based on best practice retrieved from the literature. It was decided to do the optimization on a relative level, so even if some of the assumptions were not be perfectly adequate, the final solution would be near the optimum. All simulations were done in the model scale because the simulation results then can be directly compared to the values measured with the physical model turbine.

3.2.1 Navier Stokes equations

The calculation of a viscous flow in a computational domain is based on the Navier-Stokes equations, which are a system of nonlinear partial-differential equations. With the velocity vector $\vec{u} = (u, v, w)$, the momentum equations in the three dimensional form in Cartesian coordinates for an incompressible fluid and no body forces read [91]:

$$\frac{\partial u}{\partial t} + \left(u\frac{\partial}{\partial x} + v\frac{\partial}{\partial y} + w\frac{\partial}{\partial z} \right) u = -\frac{1}{\rho}\frac{\partial p}{\partial x} + \nu \left(\frac{\partial^2}{\partial x^2} + \frac{\partial^2}{\partial y^2} + \frac{\partial^2}{\partial z^2} \right) u \tag{3.35a}$$

$$\frac{\partial v}{\partial t} + \left(u\frac{\partial}{\partial x} + v\frac{\partial}{\partial y} + w\frac{\partial}{\partial z} \right) v = -\frac{1}{\rho}\frac{\partial p}{\partial y} + \nu \left(\frac{\partial^2}{\partial x^2} + \frac{\partial^2}{\partial y^2} + \frac{\partial^2}{\partial z^2} \right) v \tag{3.35b}$$

$$\frac{\partial w}{\partial t} + \left(u\frac{\partial}{\partial x} + v\frac{\partial}{\partial y} + z\frac{\partial}{\partial z} \right) w = -\frac{1}{\rho}\frac{\partial p}{\partial z} + \nu \left(\frac{\partial^2}{\partial x^2} + \frac{\partial^2}{\partial y^2} + \frac{\partial^2}{\partial z^2} \right) w \tag{3.35c}$$

These three equations are supplemented by the continuity equation that guarantees a conservation of mass and reads

$$\frac{\partial \rho}{\partial t} + \nabla \cdot (\rho \vec{u}) = \frac{\partial \rho}{\partial t} + \frac{\partial (\rho u)}{\partial x} + \frac{\partial (\rho v)}{\partial y} + \frac{\partial (\rho w)}{\partial z} = 0 \tag{3.36}$$

and in the case of incompressible fluids simplifies to

$$\nabla \cdot \vec{u} = \frac{\partial u}{\partial x} + \frac{\partial v}{\partial y} + \frac{\partial w}{\partial z} = 0. \tag{3.37}$$

3.2.2 Discretization methods

In order to simulate a physical flow problem, the continuous partial differential Navier-Stokes equations have to be converted into a discrete form so that the resulting equation system can be solved. There are numerous discretization strategies that accomplish this, of which the three most important ones will be briefly described in the following sections.

Finite difference method

With the finite difference method (FDM) the partial derivatives in the differential equations are replaced by difference equations. This is usually accomplished by a Taylor series that represents a function as an infinite sum of terms that are calculated from the values of the function's derivatives. The problem is then approximately solved by calculating the solution for the difference equations at discrete points of time and space. The error between the numerical and the exact solution is called discretization error or truncation error. It stems from the fact that only a finite part of the Taylor series is used in the approximation, i.e. the Taylor series is truncated. The number of terms included in the Taylor series defines the order accuracy. Including many terms, e.g. a second-order accuracy leads to a high rate of convergence, which means that the approximation errors are reduced quickly when the timestep or grid size resolution is increased. However, higher order accuracy schemes increase the computational effort and are generally less numerically stable than low-order schemes [90].

The finite difference method is in most cases employed with structured grids, which allows for very efficient computation. It is therefore only suited for block-shaped or rectangular, but not for irregular geometries. Moreover, the method in itself does not conserve quantities such as mass, momentum or energy, unless special methods are applied [92].

Finite volume method

In the finite volume method (FVM) the spatial domain is discretized into small finite volumes that do not overlap [92]. The integral form of the conservation equations for mass, momentum, and energy are the basis for the computation. Fluxes through the finite volumes are equal to the fluxes through the combined volume faces. Values for the solution variables are computed and stored at nodes that lie in the center of each volume and interpolation is used to express the values on the volume surfaces.

The finite volume method is suited for unstructured grids and complex geometries and is relatively easy to implement. The main advantages are that the mass, momentum, and energy quantities are conserved very well. This makes it the most commonly used method in engineering applications [92].

Finite element method

The finite element method (FEM) partitions the domain into many small elements that consist of nodes that are connected to each other. It is in this regard similar to the Finite volume method. However, the equations are multiplied by a test function, which is also referred to as weighting, before integrating them over the whole domain.

Continuity is achieved by approximating each element value by an internal function so that the values are consistent with the neighboring values. The method can be applied to both structured and unstructured grids. Unfortunately, the FEM method does not guarantee a local or global conservation of flow variables and is therefore not used as frequently as the finite volume method. The finite element method is historically most commonly used in the simulation of structural mechanical problems [93].

3.2.3 Simulation of turbulent flows

Turbulent flow is present in virtually all practical engineering problems and therefore turbulence should not be neglected. Turbulence must either be resolved directly, or modeled by an appropriate turbulence model. According to [94], turbulence modeling is, besides grid generation and the development of solving algorithms, one of three key elements in Computational Fluid Dynamics (CFD). Its purpose is to approximate the essential physical behavior of turbulent flows by means of a mathematical model that has a minimum amount of complexity [94].

In the past, numerous approaches to solve the Navier-Stokes-Equations were developed, some of which employ turbulence models of varying complexity. The most frequently utilized ones can be grouped together in three classes described in the following sections.

Direct numerical simulation

The Direct numerical simulation (DNS) approach is based on a very fine mesh in order to directly resolve eddies of all scales using the Navier-Stokes-Equations. The whole range of spatial and temporal scales is resolved, and therefore this approach directly simulates turbulent features. The smallest scales to be resolved are the Kolmogorov scales, of which the Kolmogorov length scale η is the one which determines the minimum cell size of the mesh. According to [89], in order to resolve this scale in a three-dimensional mesh, the number of mesh nodes and therefore computational effort increases with

$$N = Re^{9/4}. \tag{3.38}$$

Figure 3.8 depicts the typical energy spectrum of a turbulent flow on a log-log scale of the turbulent kinetic energy E versus the wave number k. It shows the energy contained in the flow for different sizes of eddies. Most of the energy is contained in the large eddy scales (low wave number k), but a significant part is also contained in the inertial sub-range, where k is "small enough that viscosity does not affect the motion, but large enough that the overall dimensions of the flow such as boundary-

layer thickness do not matter" [94]. At very high wave numbers of k, the dissipation or viscous range is located, where kinetic energy is dissipated into heat.

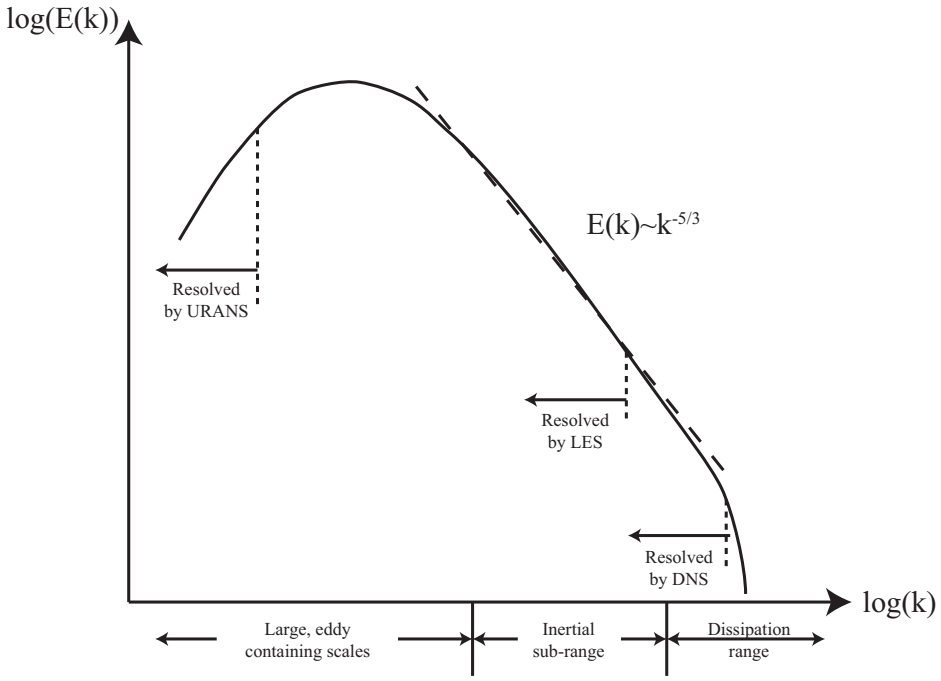

Figure 3.8: The typical energy spectrum of a turbulent flow plotted against the wavenumber [95]

With today's supercomputers, simulations with up to 10^8 elements can be solved [89], but this is far from enough to examine real engineering problems. In the foreseeable future, it will therefore not be possible to use DNS for those applications and thus it is necessary to find simplifications in order to reduce the computational effort.

Large eddy simulation

Kolmogorov's theory of self-similarity implies that large eddies are dependent on the geometry but small eddies are more universal. This means that it is sufficient to solve for the larger scales and to model the smaller scales as depicted in Figure 3.8. Large eddy simulations (LES) take advantage of this and make a significant reduction in the computational effort in comparison to direct numerical simulations significantly while still covering the characteristic flow features. The Navier-Stokes-equations are low-pass filtered, which can be compared to a temporal and spatial averaging, i.e. ignoring the information on the small-scale. Thus, large eddies are explicitly resolved, but the effect of small eddies has to be implicitly accounted for by a subgrid-scale model of which several exist. As only large eddies have to be resolved, Large Eddy Simulations can be computed on coarser meshes than DNS.

Detached eddy simulation

Detached eddy simulations are a hybrid of the RANS model, which is described in the next section, and the LES model. In regions where the mesh is not fine enough to resolve all turbulent length scales, typically near walls, the model uses RANS. In regions where the turbulent length scales exceed the mesh resolution, typically in the free stream, the model switches to LES. The computational effort is higher than with pure RANS models but lower than with pure LES models. Mesh generation, however, is more complicated as in the separate cases, as the switch between the models has to be considered.

Reynolds-Averaged-Navier-Stokes simulation

To reduce the computational effort even more, the Reynolds-Averaged-Navier-Stokes (RANS) approach was developed. As the name suggests, the Navier-Stokes-Equations are time-averaged and therefore simplified. Thus, small-scale temporal fluctuations are neglected and only the large-scale dynamics are represented. However, the nonlinear influence from the small-scale fluctuations that have an effect on the large-scale fluid motion has to be modeled [96]. For a steady flow, the instantaneous quantities are described using a time-averaged part and a fluctuating part, which is achieved by what is referred to as Reynolds decomposition. If we consider for example the instantaneous velocity u, the decomposition is defined as

$$u(x, y, z, t) = \overline{u}(x, y, z) + u^{'}(x, y, z, t) \tag{3.39}$$

where $\bar{u}$ is the average velocity and $u^{'}$ is the value of the fluctuation at a given time.

The time-averaged Navier-Stokes equations for a stationary, incompressible Newtonian fluid can be written in Einstein notation as

$$\rho\bar{u}_j\frac{\partial\bar{u}_i}{\partial x_j} = \rho\bar{f}_i + \frac{\partial}{\partial x_j}\left[-\bar{p}\delta_{ij} + \mu\left(\frac{\partial\bar{u}_i}{\partial x_j} + \frac{\partial\bar{u}_j}{\partial x_i}\right) - \rho\overline{u_i'u_j'}\right]. \tag{3.40}$$

The term on the left-hand side quantifies the variation in mean momentum from unsteadiness and convection. It is balanced by the mean body force, the stress caused by the mean pressure field, the viscous stresses, and the Reynolds stress $\left(-\rho\overline{u_i'u_j'}\right)$.

The Reynolds stress, although it has the dimensions of stress is in fact not a stress, but accounts for turbulent fluctuations in fluid momentum. Its value cannot be related directly to flow properties and is therefore unknown. The appearance of this term leads to a problem referred to as the closure problem of the Reynolds-averaged Navier-Stokes equations: There are more unknowns than there are equations. In a three dimensional case, there are six stress components that have to be related to the mean motion before the equations can be solved [97]. This information gap has to be overcome by modeling the Reynolds stresses.

RANS-based turbulence modeling There are three main categories of RANS-based turbulence models:

1. Linear eddy viscosity models
   (a) algebraic models
   (b) one-equation models
   (c) two-equation models
      i. k–ε
      ii. k–ω
2. Nonlinear eddy viscosity models
3. Reynolds stress model

k–ε-model The k–ε-model is a two-equation turbulence model that is based on the computation of two extra transport variables, namely the turbulent kinetic energy k that determines the energy in the turbulence, and the turbulent dissipation ε, which determines the scale of the turbulence. The two transport equations read [98]:

$$\frac{\partial}{\partial t}(\rho k) + \frac{\partial}{\partial x_i}(\rho k u_i) = \frac{\partial}{\partial x_j}\left[\left(\mu + \frac{\mu_t}{\sigma_k}\right)\frac{\partial k}{\partial x_j}\right] + P_k + P_b - \rho\varepsilon - Y_M + S_k \tag{3.41}$$

$$\frac{\partial}{\partial t}(\rho\varepsilon) + \frac{\partial}{\partial x_i}(\rho\varepsilon u_i) = \frac{\partial}{\partial x_j}\left[\left(\mu + \frac{\mu_t}{\sigma_\varepsilon}\right)\frac{\partial \varepsilon}{\partial x_j}\right] + C_{1\varepsilon}\frac{\varepsilon}{k}\left(P_k + C_{3\varepsilon}P_b\right) - C_{2\varepsilon}\rho\frac{\varepsilon^2}{k} + S_\epsilon \tag{3.42}$$

The constants in the model have to be defined and are usually chosen according to Table 3.4.

Table 3.4: Constants in the standard k-epsilon model [92]

C_μ	$C_{\varepsilon 1}$	$C_{\varepsilon 2}$	σ_k	σ_ε
0.09	1.44	1.92	1.00	1.30

The k–ε-model is one of the most frequently used turbulence models because it is proven to be stable and offers a good compromise between accuracy and robustness [90]. However, it may not be suitable for flows with boundary layer separation, flows with sudden changes in the mean strain rate, flows in rotating fluids and flows over curved surfaces [90]. Moreover, the onset of flow separation is predicted too late by epsilon-based turbulence models, which also leads to an under-prediction of the amount of separation later on. Flow separation can be very detrimental to the efficiency of hydraulic turbines and it is crucial to model it correctly.

k–ω-model The k–ω-model introduced by Wilcox is similar to the k–ε-model in the sense that one of the extra transport variables is the turbulent kinetic energy k. The second variable ω is the characteristic frequency of the energy dissipating eddies [94].

$$\rho\frac{\partial k}{\partial t}+\rho\bar{u}_j\frac{\partial k}{\partial x_j}=C_\mu\rho\mu_t\left(\frac{\partial\bar{u}_i}{\partial x_j}+\frac{\partial\bar{u}_j}{\partial x_i}\right)\frac{\partial\bar{u}_i}{\partial x_j}-\beta^*\rho k\omega+\frac{\partial}{\partial x_j}\left[(\mu+\sigma^*\mu_t)\frac{\partial k}{\partial x_j}\right] \quad (3.43)$$

$$\rho\frac{\partial \omega}{\partial t}+\rho\bar{u}_j\frac{\partial \omega}{\partial x_j}=\alpha\frac{\omega}{k}C_\mu\rho\mu_t\left(\frac{\partial\bar{u}_i}{\partial x_j}+\frac{\partial\bar{u}_j}{\partial x_i}\right)\frac{\partial\bar{u}_i}{\partial x_j}-\beta\rho\omega^2+\frac{\partial}{\partial x_j}\left[(\mu+\sigma\mu_t)\frac{\partial \omega}{\partial x_j}\right] \quad (3.44)$$

The standard k–ω-model is well suited for the simulation of boundary layer flows near walls. It is however very sensitive to the free stream boundary condition of omega. This means that the user has to decide on a value for omega that is appropriate for the flow in question and set it at the free stream boundary. This behavior is referred to as free stream sensitivity of the k–ω turbulence model.

Shear-Stress-Transport The Shear-Stress-Transport turbulence model was introduced by Menter in 1994 and combines the advantages of the k–ε-model in the free stream and the k–ω-model near walls [99] [100]. The transition between the two models is accomplished by using a blending function that is based on wall distance. For free shear flows, the SST model and the k–ε-model give identical results.

SST was designed to predict the onset and extent of flow separation under adverse pressure gradients by modifying the eddy viscosity formulation, to account for the transport effects of the principal turbulent shear stress [90].

Kato-Launder modification (production limiter) The Kato-Launder modification was introduced by Kato and Launder in 1993 and can be used with most two-equation models [101]. It is a modification to the term for the rate of production of the turbulent kinetic energy, which is over-predicted by many models, especially in regions with strong acceleration.

Turbulence intensity The turbulence intensity, also referred to as turbulence level, is defined as

$$I=\frac{u'}{U}\quad [–]. \quad (3.45)$$

where u' is the root-mean-square of the turbulent velocity fluctuations and U is the mean velocity [102]. If the turbulent energy k is known, u' can be calculated by

$$u'=\sqrt{\frac{1}{3}(u_x'^2+u_y'^2+u_z'^2)}=\sqrt{\frac{2}{3}k}\quad [\mathrm{m/s}]. \quad (3.46)$$

U can be computed from the three mean velocity components U_x, U_y, and U_z with

$$U=\sqrt{U_x^2+U_y^2+U_z^2}\quad [\mathrm{m/s}]. \quad (3.47)$$

Handling of the boundary layer

In wall-bounded flows the velocity is zero at the point of contact with a wall and increases with distance from the wall, forming a velocity profile. Moreover, gradients of flow properties in this region are very strong and viscous effects have a large influence. To accurately simulate these processes it is important to account for the viscous effects near the wall and to represent the rapid change of flow variables perpendicular to the wall.

An important variable in describing the flow near walls is the dimensionless wall distance y^+. This is the perpendicular distance y of a point to the wall, made dimensionless using [103]

$$y^+ = \frac{u_* \cdot y}{\nu} \quad [–], \tag{3.48}$$

where u_* [m/s] is the friction velocity at the nearest wall, y [m] is the distance to the nearest wall and ν [m^2/s] is the local kinematic viscosity [103].

The friction or shear velocity u_* is a re-written form of the shear stress so that it has units of velocity:

$$u_* = \sqrt{\frac{\tau_w}{\rho}} \quad [\mathrm{m/s}], \tag{3.49}$$

where τ_w is the wall shear stress and ρ is the density of the fluid. The wall shear stress τ_w is defined as

$$\tau_w = \mu \left(\frac{\partial u}{\partial y} \right) \quad [\mathrm{kg/(m\,s^2)}], \tag{3.50}$$

where μ [Ns/m^2] is the dynamic viscosity of the fluid, u [m/s] is the fluid velocity parallel to the wall and y [m] is the distance to the nearest wall [99]. The dimensionless velocity u^+ is the velocity u parallel to the wall as a function of y, divided by the friction velocity u_*:

$$u^+ = \frac{u}{u_*} \quad [–]. \tag{3.51}$$

Average fully developed turbulent velocity profiles in the vicinity of walls have been analyzed experimentally and mathematically. They can be universally described with the dimensionless parameters y^+ and u^+. Velocity profiles can be divided into three zones as shown in Figure 3.9.

The zone adjacent to the wall is referred to as viscous sublayer and extends to a wall distance of up to $y^+ < 5$. The velocity in this layer increases linearly with distance to the wall and is dominated by viscous effects:

$$u^+ \propto y^+ \tag{3.52}$$

The zone furthest from the wall is referred to as the logarithmic region. It spans a wall distance of approximately $30 < y^+ < 500$ and the dimensionless velocity u^+ in

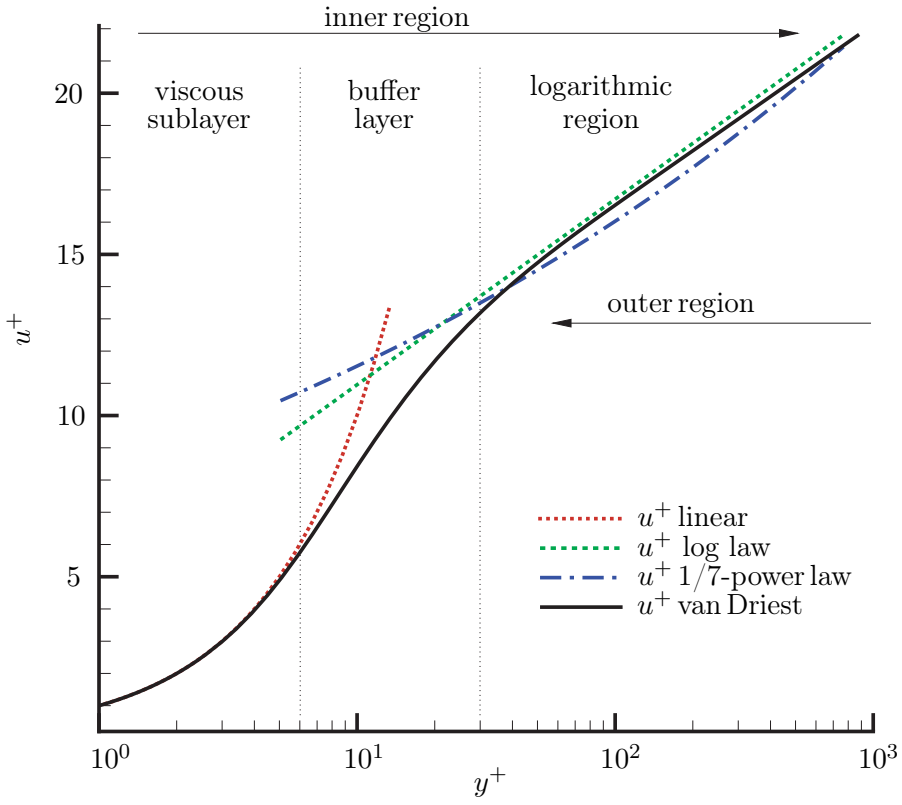

Figure 3.9: Velocity profiles resulting from different wall functions [104]

this region is proportional to the natural logarithm of the distance from the wall, as turbulent transport processes dominate the flow. This relation can be expressed with

$$u^+ = \frac{1}{\kappa} \ln y^+ + C^+ \tag{3.53}$$

where κ is the Von Kármán constant ($\kappa \approx 0.41$) and C^+ is a constant that is dependent on the wall roughness.

The layer in between ($5 < y^+ < 30$) is referred to as buffer layer and here neither the viscous nor the turbulent effects may be neglected, as they have approximately the same magnitude.

Two approaches are commonly used to model the flow near walls: Low-Reynolds-number models and wall function models. The name of Low-Reynolds-number models refers to the Reynolds number in the viscous sublayer, which is usually low, even for highly turbulent flows in the free stream. In these models, the boundary layer flow is computationally resolved by placing many cells in the boundary layer perpendicular to the wall. The method delivers accurate results but has a high computational effort due to a large number of nodes required. Wall function models are based on empirical formulas determined in experiments on typical flows. They do not resolve the boundary layer and therefore fewer elements near walls are required. This saves computational resources by using relatively coarse meshes and still allows to model the high gradients

of the flow properties in the boundary layer. This process is referred to as an automatic near-wall treatment.

3.3 Optimization procedure and simulation setup

The initial design of the turbine was based on the results of a feasibility study that is presented in [1]. [79] states that a common hub-to-shroud ratio of Kaplan-turbines is 0.4, which is needed to accommodate the control mechanism of the blades. To achieve a higher unit discharge a reduced hub-to-shroud ratio of 0.35 was chosen as no control mechanism is needed in the design with fixed runner blades. Runners of axial turbines usually have between three and eight runner blades while the number of blades decreases with increasing specific speed [79]. The design of a three-bladed runner was chosen for the present project, as the turbine is intended to have a high specific speed.

One constraint in the design was that all parts of the final turbine stage had to fit into the confined space given by the turnable turbine concept described in Section 1. Due to mechanical and economical reasons the size of the turning cylinder should be as small as possible with regard to the runner diameter. For a runner diameter of $D = 0.34\,\mathrm{m}$ a cylinder size of $0.6\,\mathrm{m}$ was defined, as depicted in Figure 3.14. The meridional contour adjacent to the turbine stage was designed to be symmetrical in order to fit the overall symmetrical design.

The optimization of the turbine was done iteratively in the process depicted in Figure 3.10. The challenge was to find a good combination of turbine and pump characteristics. All simulations were carried out with the Shear-Stress-Transport turbulence model and a high-resolution advection scheme, as is recommended by the CFX reference guide.

3.3.1 Geometry

Each part of the turbine has to be optimized with respect to different objectives. The individual requirements and considerations are presented in the following sections. The process started with the design of an initial geometry for the turbine. The geometry was then imported into the project and meshes were created. After that, simulation properties such as fluid definition, boundary conditions, and solver parameters were set. Subsequently, a number of simulations were run for each geometry and the simulation results were evaluated and analyzed. Weaknesses of the design were identified based on an interpretation of the results. The geometry was then modified in an attempt to improve its performance. The focus of geometry modifications was on the

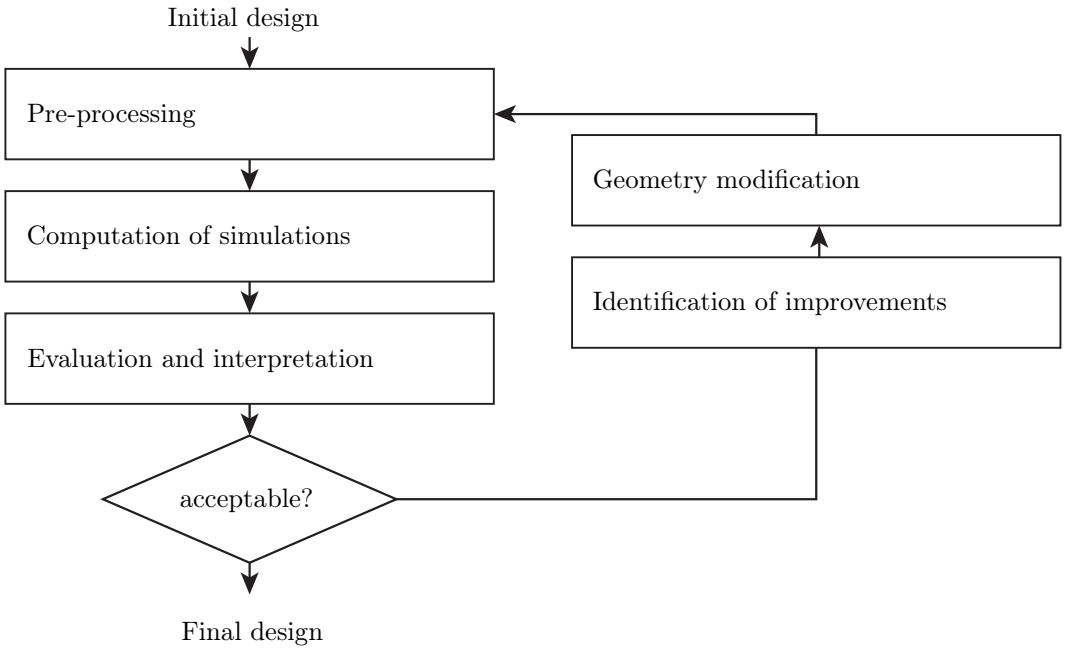

Figure 3.10: Steps of the optimization process

guide vane and runner blade shapes, as well as the meridional contour. This process was repeated until the performance of the turbine was satisfactory.

For the simulations and the model turbine geometry, a Cartesian coordinate system is used. Its origin, i.e. the center point, lies in the center of the runner while the main rotation axis of the runner defines the Z-axis. The main transport direction of the water is parallel to this axis, and the turbine is referred to an axial turbine. The Y-axis goes from top to bottom and the X-axis from left to right.

Meridional contour

The meridional profile defines the boundary of the flow path through the turbine. It can be represented on a meridional section, i.e. a section along the rotational axis of the turbine. When the meridional profile is rotated by 360° it defines the hub and shroud surfaces. Ideally, all curves of the meridional profile are continuous, in order to prevent any unfavorable flow conditions such as flow separation. The shape of the meridional profile also determines the flow cross-section at each point of the turbine. Finding a good shape is important in order to obtain a uniform distribution of the meridional velocity c_m. The inlet to the turbine stage is circular. The contour then narrows towards the guide vanes and runner and behind the runner, it gets wider again. At the inlet, the inclination of the shroud is slightly higher than at the hub in order to make use of conservation of momentum. By choosing such a configuration the magnitude of $r \cdot c_u$ is increased to a greater degree than at the shroud, which yields a more favorable swirl distribution at the runner inlet.

The nose of the hub at the intake has a circular shape to enable a short transition towards the guide vanes. This is necessary because the space ahead of the guide vanes is very limited so that all parts of the turbine stage can be fitted into the reversible cylinder. At the outlet end, the shape of the hub is more elongated to allow for a steadier increase of the cross-section. This was designed to prevent the occurrence of flow separations in the decelerated flow in turbine mode.

Guide vanes

Guide vanes have different functions and are a very important element of the turbine. As described in Section 3.1.1 the working principle of turbines is to reduce the Euler Head in the turbine runner, i.e. to change the circumferential component of the flow. In order to achieve a low circumferential velocity downstream of the runner, i.e. a low exit swirl, the flow needs to have an appropriate circumferential velocity magnitude upstream of the runner. In Pelton turbines, this is achieved by the orientation of the nozzle to the rotation axis to the runner. In Kaplan turbines, the circumferential velocity is predominantly created by the spiral casing. Tubular turbines do not possess a spiral casing and thus the swirl upstream of the runner has to be created solely by the guide vanes. They accelerate the flow by converting pressure into velocity and deflect it into a circumferential rotation, thus creating a swirl. The swirl magnitude on each span depends on the deflection angle of the specific guide vane profile and the guide vane angle, which describes its orientation. By turning the guide vanes around an axis perpendicular to the flow the free cross-section available to the flow can be adjusted, which allows for regulation of the discharge. In run-of-river hydro power plants, discharge regulation allows the operator to respond to varying flow rates of the river and thus to keep the upstream level constant. In tidal power plants, this is normally not necessary, as the aim is to empty the reservoir as quickly as possible for maximum energy production. However, the guide vanes might still be used to regulate the power output in order to meet constraints imposed by the demands of the electrical grid.

An adjustment of the guide vane angle thus results in two effects that are directly linked to each other: the intensity of the swirl and the discharge through the turbine. For this reason, an ideal swirl distribution that results in a low exit swirl downstream of the runner can only be achieved at the rated operating point of the turbine.

A third function of the guide vanes is to stop the flow through the turbine. When properly designed, the guide vanes contact each other when fully closed and the cross-section available to the flow becomes zero. This can be achieved by designing straight vanes that have no twist and an equal profile from hub to shroud. With twisted vanes,

the design is more complicated, but the desired effect can still be achieved by a special procedure.

The number of guide vanes should be even and ideally be divisible by four [79], unless the runner has four blades. The chosen quantity affects the length of each individual guide vane because the guide vanes have to cover the whole cross-section of the turbine in the closed position. A higher number results in shorter guide vanes. Moreover, there is less load on each individual vane when their number is higher. Another important consideration is to ensure the number of guide vanes is not a multiple of the number of runner blades, in order to avoid effects of resonance and vibration, i.e. a combination of three runner blades and fifteen guide vanes would be a bad choice. After careful consideration and a review of existing turbines, the number of guide vanes was chosen to be 16.

During the optimization, different guide vane geometries were designed and compared. The guide vanes profiles were created using ANSYS BladeGen in the angle and thickness mode. The curvature of the camber line was defined as constant between the leading and trailing edge, representing a circular arc. The difference in blade angle β between the leading and the trailing edge is the deflection angle of the blade (see Figure 3.1). The thickness was defined as normal to the meanline on the layer surface between the leading and trailing edge. The point of maximum thickness was defined to be at 50 % of the meridional length, giving the guide vanes a symmetrical shape. Versions with the point of maximum thickness at 33 % and 66 % were evaluated as well. The distribution of the thickness was defined as a cubic spline element with defining points at the leading and trailing edge and the point of maximum thickness. The normal thickness of the final guide vane profile was 1 at the leading and trailing edge and 5.5 at the point of maximum thickness.

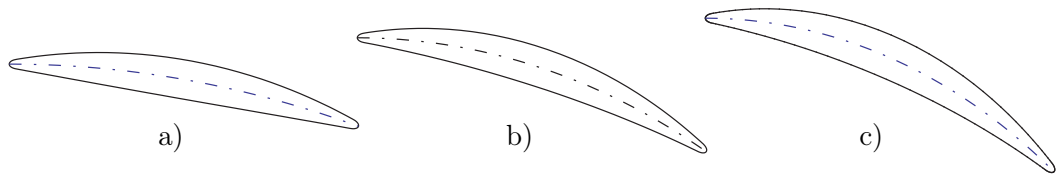

Figure 3.11: Guide vane profiles with different deflection angles a) $\Delta\beta = 20°$, b) $\Delta\beta = 35°$ and c) $\Delta\beta = 45°$

Guide vanes with deflection angles from 20° to 45° were evaluated as shown in Figure 3.11. A total of fourteen different guide vane geometries was generated and evaluated in the simulations. In early versions, the deflection of the guide vanes was equal on all layers between the hub and the shroud, e.g. a blade with a deflection of 35° had this deflection on all layers. This facilitated the design of guide vanes that had a

common line of contact when turning them around their rotation axis, thus allowing the flow to be closed off. In order to achieve this, the guide vanes were constructed using the created profiles and the theorem of intersecting lines with the focal point of all guide vanes and their rotation axis lying on the same point.

During the optimization, it proved necessary to increase the deflection near the hub in comparison to the shroud to achieve the same Euler head on all spans. The final guide vanes have a deflection of 25° at the shroud and 35° at the hub.

The guide vane angle γ is defined with respect to a parallel of the rotation axis Z so that at $\gamma = 0°$ the camber line of the guide vane at the leading edge at the hub is tangential to the Z-axis. Positive values of γ indicate a further opening of the guide vanes, while negative values indicate a closing. Figure 3.12 depicts three guide vane positions with $\gamma = +10°, 0°, \text{and} -10°$. This definition was chosen because the standard methodology for defining the guide vane angle of $\gamma = 0°$ at the closed position depends on the deflection angle of the profiles. Thus the guide vane angle with zero incidence would be different for profiles with varying deflection, which complicates a comparison of different shapes.

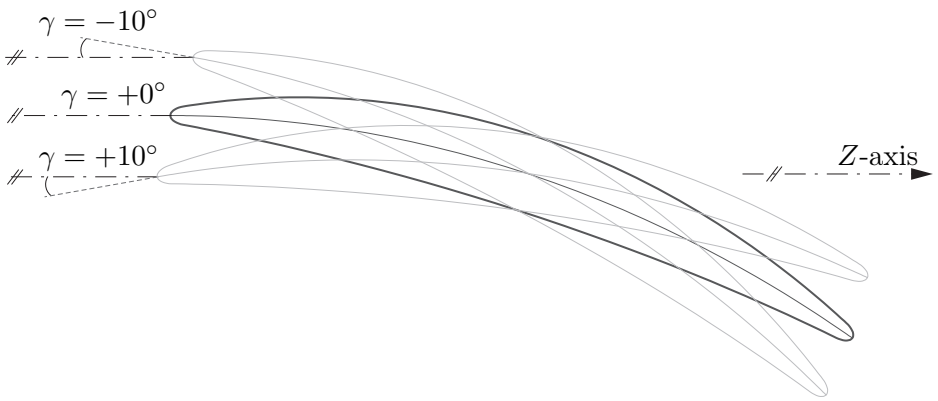

Figure 3.12: Definition of the guide vane angle γ

Runner

The runner blades need to have a specific profile that creates lift and consequently torque. The task in the optimization process was to find suitable blade profiles and to optimize the twist of the blade from hub to shroud.

The profile length of the runner blades was specified at the start and not significantly changed during the optimization process. The blade length has to compromise between frictional area and susceptibility to cavitation. If the blades are very short, the Euler head has to be extracted in a short distance, which means that the pressure difference between pressure and side has to be large, thus leading to very low pressures

on the suction side of the profile. If the profile length is too long, the losses due to friction become unnecessarily large.

Over fifty blades profiles were created with ANSYS BladeGen after the meridional contour was determined and assessed in the optimization process. Runner blades were defined on five profiles between the hub and the shroud. For spans that lie between these profiles, the shape of the blades is automatically interpolated. The deflection angle was adjusted on each of the five spans so that the same Euler head is extracted on all spans. Additionally, the twist of the blades, i.e. the angle β at the leading edge, was optimized and adjusted so that the incidence angle on all spans is equal and near to zero at the rated operating point.

Apart from that, different thickness distributions were evaluated with the point of maximum thickness being located at various locations. In order to obtain good characteristics in both the turbine and pumping mode, the final blade profiles have the point of maximum thickness at 50 % of the meridional length. The shape of the leading and trailing edges was assessed as well, with round and pointed forms, as well as truncated blades. As the flow approaches both the leading and trailing edges, depending on the flow direction, sharp edges were shown to be not feasible and both edges were designed to be round.

Draft tube

In the current work, three draft tubes with varying area ratio were evaluated. Each of them consists of two sections, the first one having a circular profile from the draft tube inlet to roughly half the draft tube length and the second one forming a transition from the circular to a rectangular cross-section towards the draft tube outlet. The first section is subdivided into three conical parts that can be made from unrollings of sheet metal, when manufacturing a model turbine, or relatively simple formwork when fabricating the draft tube from concrete. The background for this is to allow for a cost-efficient manufacturing process. The second section has a constant height and expands only in its width. A brim is attached to the draft tube end.

The core guideline for the geometry is to obtain a steady and constant increase in cross-sectional area along the draft tube length ($\frac{dA}{dL} = \text{constant}$) in order to achieve a steady deceleration of the flow. Steps or kinks that could cause flow separations must be avoided. Due to the requirements imposed by the rotating cylinder and the design of the turbine stage, an interface location where the rotating cylinder connects to the draft tube had do be defined, in order to separately design and evaluate the model turbine stage and the draft tube. This location is at 0.29 m downstream of the runner center, which is outside of the reversible cylinder and downstream of the hub.

The cross-sectional area widens already in the turbine stage itself, which leads to a reduction in flow velocity and subsequent pressure recovery. The widening of the cross-sectional area then continues in the draft tube, of which three different geometries were evaluated, see Table 3.5.

Table 3.5: Principal values of the three draft tubes

Draft tube	dA/dL [–]	m [–]	L_{dt} [m]	c_{pi} [–]
1	0.50	2.71	1.51	0.86
2	0.55	2.77	1.51	0.87
3	0.58	3.01	1.51	0.89

3.3.2 Parameterization

During the optimization process and subsequent simulation of the final geometry, a large number of simulations had to be computed. To obtain a complete hill chart of the turbine, several guide vane angles, and for each guide vane angle, several rotational speeds had to be simulated. In order to automate this process, a feature referred to as parameterization was used. It allows selected simulation input values to be defined as parametric instead of static. These values are then referred to as input parameters. They can be used to define the geometry, simulation inputs or boundary conditions such as the guide vane angle, the rotational speed of the runner, or pressures at the boundaries. In other words, input parameters automatically change the simulation setup. In the same way as with input parameters, values derived in the analysis following each simulation can be defined as output parameters. They could, for example, be the torque of the runner blades M, the head H, or the efficiency η.

A set of input parameter values is referred to as design point and represents an operational point of the turbine. To automatically perform a number of simulations, multiple design points, each with its specific input parameter values, can be defined and stored in a list. If, for example, ten design points are to be simulated, the input parameters for each point are specified in advance. Then the software can be instructed to update all design points in sequence and automate the setup.

First, the input parameter values of the first design point are read and the simulation setup is updated accordingly. Then the simulation for the specific design point is performed. After this is completed, the values of the output parameters are determined in the post-processing and stored in the list of design points. Then the input parameter values of the second design point are read. This process is repeated until

all design points are simulated and the corresponding output parameters values are determined.

3.3.3 Determination of flow parameters

Some simulation parameters, such as the rotational speed and the flow rate, are known beforehand because they are input parameters. Other parameters, such as the runner torque or the hydraulic head have to be determined after each simulation. The runner torque can be determined from the pressure difference on the runner blade surfaces, but some parameters depend on the conditions in the flow itself, where no surface is present. Examples are the total pressure p_t and the static pressure p_s. They are derived in the post-processing on planes normal to the Z-direction. In the model tests, there are four measuring planes, which are depicted as 1–4 in Figure 3.13.

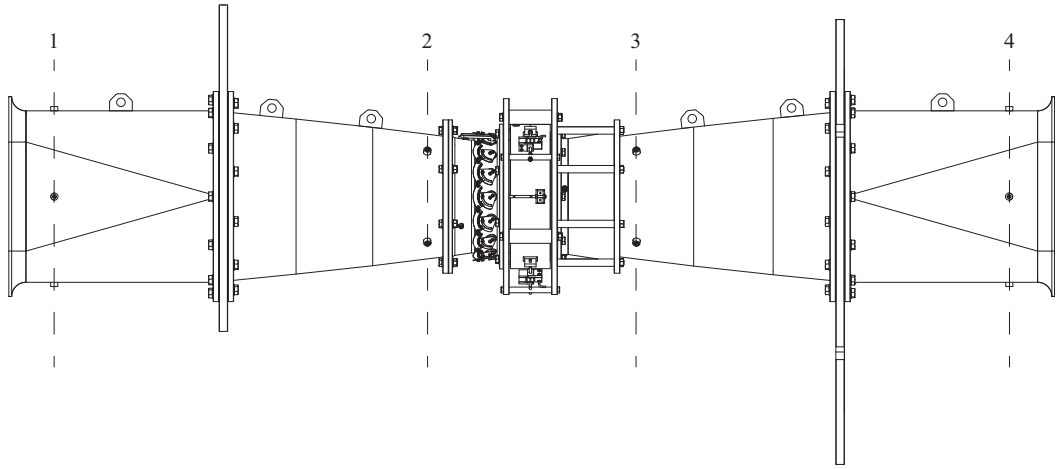

Figure 3.13: Locations of the measuring planes [76]

The turbine performance can be evaluated in two ways. The first takes only the turbine stage into account and therefore uses the measuring planes two and three, which are located at a distance of 370 mm from the origin. At the start of the optimization, only the turbine stage is simulated in order to spare computational effort. At a later time, the whole turbine, including the draft tube and inlet is simulated. The second simulation takes the whole turbine with inlet geometry and draft tube into account and the corresponding measuring planes are 1 and 4, each at a distance of 1680 mm from the origin. The turbine head H_{IEC} is calculated according to Equation 3.12.

In the post-processing stage, H_{ICE} is determined by calculating the area-weight average of the static pressure p_s on the reference planes. Area-weighting is appropriate because the static pressure is a quantity that is spatially conserved.

The area-weighted average is the integral of the local static pressure multiplied by the local area divided by the total area. Since static pressure is the force that acts

on surfaces it makes sense to weight its average based on the area so that the spatially dominant quantity has the greatest influence.

$$areaAve(p_s) = \frac{\int p_s dA}{A} \quad [\text{Pa}] \tag{3.54}$$

The total head H_t results from the difference in total pressure Δp_t between the upstream and downstream boundary, as defined in Equation 3.23. The total pressure at each location refers to the sum of static pressure p_s, the kinetic energy $\frac{c^2}{2g}$ and the elevation z. The average total head on the reference planes is determined by calculating the mass flow weighted average of the total pressure p_t. The mass flow average is an integral of the local total pressure multiplied by the local mass flow, divided by the total mass flow.

$$massFlowAve(p_t) = \frac{\int p_t d\dot{m}}{\dot{m}} \quad [\text{Pa}] \tag{3.55}$$

The weighting by the local mass flow is important because the total pressure is not spatially conserved. Locations with low flow velocities have a little mass transport and total pressure, but they also contribute very little to the flow and therefore need to be given a correspondingly low weight, even when their area is large. The mass flow average is therefore needed if energetic quantities such as the total pressure are compared. However, if for example the mass flow averaged velocity of a nonuniform flow is calculated and multiplied by the total area, the calculated flow rate will not be correct and in this case the area average would be appropriate.

The torque of the runner M is determined by the CFD-post function *torque*, which uses the pressure on the runner blade surfaces to calculate the torque around the Z-axis. The angular velocity ω is known in each case, as it is an input parameter.

3.3.4 Numerical mesh

Figure 3.14 depicts the four separate meshing domains. In simulations of the turbine mode, the domain denoted as "inlet domain" acts as intake, while the domain denoted as "outlet domain" acts as a draft tube. The designation of the domains is not changed when switching between turbine and pumping mode simulations. Thus, in simulations of the pumping mode the domain denoted as "outlet domain" acts as intake, while the domain denoted as "intake domain" acts as a draft tube.

Both the inlet and outlet domain were meshed using the ANSYS Meshing application, which creates an unstructured mesh that consists of hexahedral, tetrahedral and pyramidal elements. Prism layers were introduced at all solid surfaces in order to allow for an adequate modeling of the boundary layer. The number and growth rate of the prism layers was set individually at different locations to achieve appropriate y^+-values.

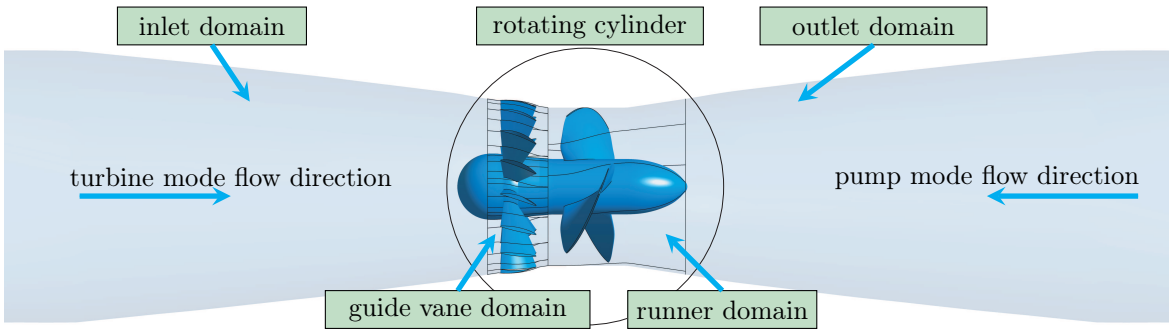

Figure 3.14: Overview of the turbine geometry with the four mesh domains

The guide vane and runner domains were meshed using TurboGrid, which is a tool specifically developed for the meshing of turbomachinery components. It uses the geometrical data of the hub, shroud and blade surfaces as an input. By using a predefined topology, i.e. "Automatic Topology and Meshing", it creates a mesh for the passage between the blades, which consists solely of hexahedral elements. A mesh representing the hub and shroud surfaces, and various layers in between, is created. Figure 3.15 depicts the mesh as 2D representation on the shroud layer of a guide vane.

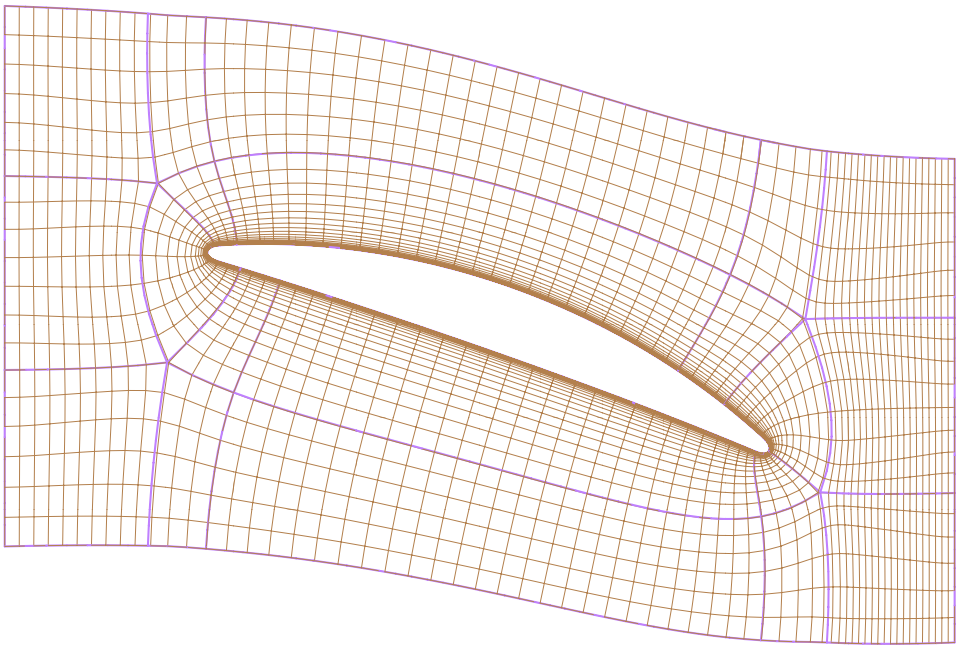

Figure 3.15: Topology and refined mesh at the shroud layer of one guide vane

Magenta colored lines in the figure depict the master block topology curves and the thin brown lines show the final mesh on the shroud layer. The number of elements in streamwise direction, i.e. between the leading and trailing edge, can be set using edge split controls, which basically split the topology blocks. The resolution normal to

surfaces is defined by a target y^+-value and an expansion rate. The number of elements in spanwise direction can be defined as well. Apart from the y^+-value, a global size factor determines how many elements are generated in total for each mesh. In order to obtain a good mesh quality, some mesh limits have to be met. These are the minimum face angle, the maximum face angle, the maximum element volume ratio, the minimum volume, the maximum edge length ratio and the maximum connectivity number. In order to obtain a good mesh quality and to stay below the mesh limits, the global size factor has to be adjusted depending on the chosen y^+-value. In general, a lower target y^+ leads to an increased number of elements. A detailed view of one runner mesh is given in Figure 3.16. It shows the quadrilateral faces of the hexahedral elements on the blade and hub surface, as well as the y^+-distribution on the two surfaces.

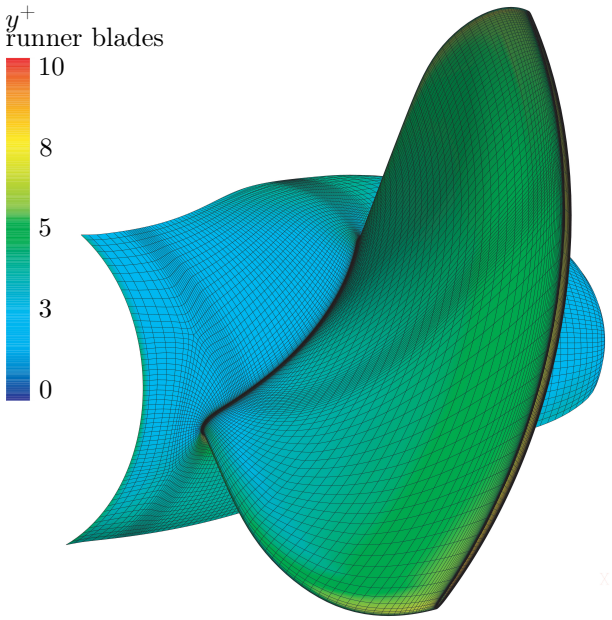

Figure 3.16: Mesh of the runner with y^+-values on the blade and hub surfaces

Mesh independence study

In order to find a good compromise between simulation time and accuracy of results and to verify that the results are independent of the chosen mesh resolution, a mesh independence study was conducted. Eight simulations were carried out for the study, each with a similar turbine setup and a different mesh resolution. The target y^+-value was varied in a range between 100 and 1. The number of nodes was set individually for each mesh so that all mesh quality criteria were met.

Table 3.6 lists the mesh values and some selected results from the simulations carried out in the mesh independence study. The number of mesh elements rises exponentially

Table 3.6: Mesh values and results of the mesh independence study

y^+ [–]	# of elements [–]	P_{fl} [W]	P_{me} [W]	η_t [%]	H_t [m]
100	214,097	13,555	12,099	89.3	2.91
50	405,485	13,267	11,774	88.8	2.85
30	672,197	13,359	11,863	88.8	2.87
15	1,214,156	14,096	12,564	89.1	3.03
10	1,505,952	14,568	13,034	89.5	3.13
5	2,346,468	14,934	13,398	89.7	3.21
2.5	5,307,843	15,092	13,583	90.0	3.24
1	14,438,470	15,120	13,636	90.2	3.25

when y^+ is decreased. In the region of large values of y^+ the resulting quantities differ significantly between different simulations. With increasing mesh resolution the differences in the results between the setups are decreasing. The discrepancies between values obtained with $y^+ = 5$ and $y^+ = 1$ are considered to be negligible. This trend is also evident in Figure 3.17, which depicts the total head H_t and number of mesh elements in relation to y^+.

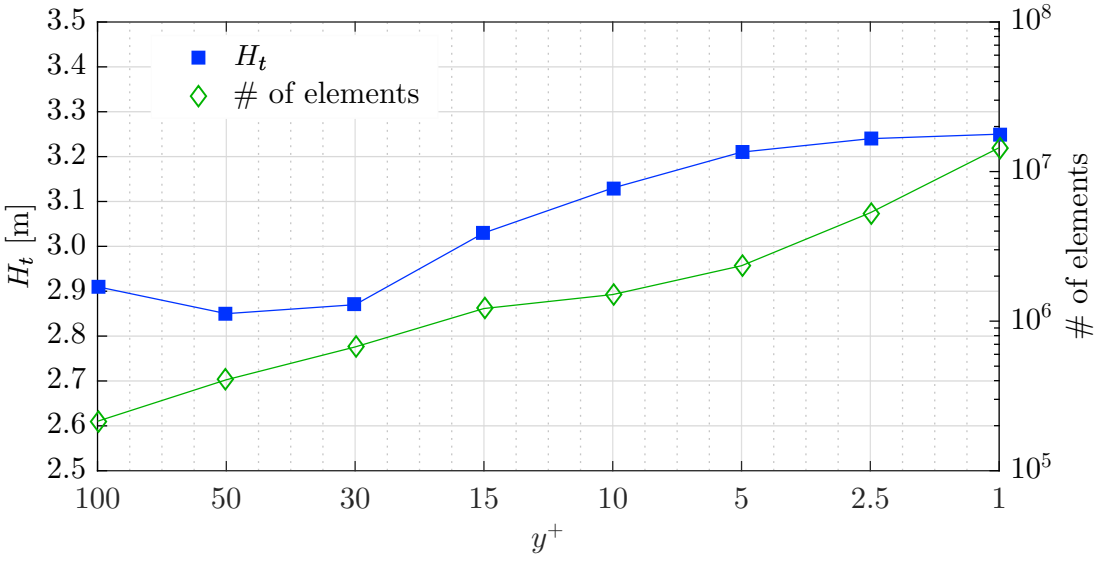

Figure 3.17: Number of mesh elements and H_t at varying y^+

In the preliminary optimization steps, meshes with a target value of $y^+ = 50$ were used and for the simulation of the final geometry meshes the target value of $y^+ = 5$ was set. This proved to be a very efficient strategy for keeping the computation time within limits, while still achieving an accurate end result.

3.3.5 Boundary conditions

The computational domain is spatially limited by the boundaries of the mesh which imposes a boundary value problem. In order to solve the differential equations governing the fluid flow, the conditions on all boundaries have to be defined. There are different types of boundary conditions. If the value of the function itself is defined at the boundary, this is referred to as a Dirichlet boundary condition. Boundary conditions that define the value of the derivative of the function in question are known as Neumann boundary conditions. A combination of these two types is the Robin boundary condition, which linearly combines the function values and the values of the derivative of the function on the boundary. Cauchy boundary conditions define both the function value on the boundary and the normal derivative on the boundary of the domain.

Inlet and outlet boundary condition

In the CFD context, inlet boundary conditions are set at locations where flow predominantly enters the domain, while outlet boundary conditions are set where flow predominantly exits the domain. In turbine mode, the inlet is the boundary that is located upstream of the guide vanes and the outlet is at the draft tube end. In simulations of the pumping mode, the location of the two boundary conditions is reversed.

There are different types of inlet and outlet boundary conditions and only a few combinations make sense, as the numerical problem must not be under-determined, nor over-determined. The most robust combination according to the ANSYS CFX modeling guide is to define a mass flow rate $\dot{m}$ at the inlet and a static pressure p_s at the outlet. This was done for all simulations, while the static pressure at the outlet was set to the same value of $p_s = 40.000\,\text{Pascal}$ in all simulations. The total pressure at the inlet is then an implicit result of the computation as it depends on the flow rate and head H.

Static pressure The exact conditions under which the turbine would operate in a tidal barrage plant were not known when the turbine was designed, as they depend to a great extent on the characteristics of the specific site. However, in order to assess the cavitation susceptibility, a Thoma number for the plant had to be defined. To be on the safe side, the maximum turbine head was assumed to be $H = 8$ m, a value which might only be reached in places with a exceptionally high tidal range. The design head of the turbines in the La Rance tidal barrage plant is 6.4 m by comparison. The maximum suction head of $h_s = -2.4$ m was estimated on the basis of the final draft tube design, an assumed runner diameter of $D = 5$ m and a minimum submergence

at the draft tube end of 0.5 m (see Figure 3.18). The vapor pressure of water is a function of its temperature; its maximum value was defined to be $p_v = 2073$ Pa at $T = 25$ °C.

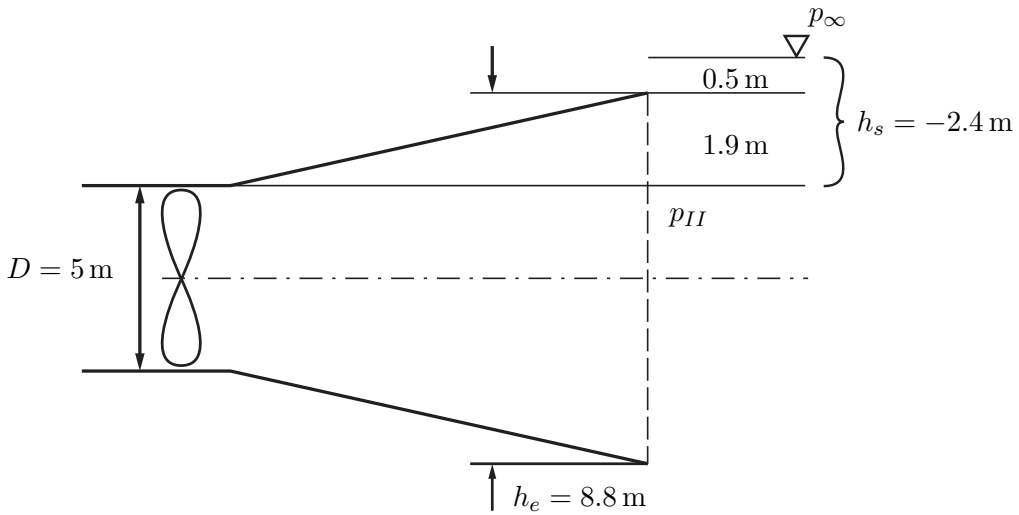

Figure 3.18: Definition of a setting to obtain σ_{plant}

With these values, σ_{plant} can be calculated for the turbine mode with

$$\sigma_{plant} = \frac{p_\infty - p_v - \rho g h_s}{\rho g H} = \frac{101.325\,\text{Pa} - 2.073\,\text{Pa} + 23.474\,\text{Pa}}{78.248\,\text{Pa}} = 1.57. \quad [–] \qquad (3.56)$$

The value of $\sigma_{plant} = 1.57$ is well within the limits of σ_c for typical bulb turbines (see Figure 3.6). In order to evaluate the cavitation characteristics of the turbine in the defined setting, the static pressure at the suction side boundary condition has to be adjusted individually for each operating point. This results from the fact that the head H is different in each simulated operating point and therefore the suction head h_s has to change in order to keep σ_{plant} constant. This adjustment, i.e. a shift of static pressure p, was done in the post-processing stage rather than the pre-processing stage, as the head H of each operating point is not known beforehand.

This methodology can also be applied to the pumping mode, where the required head for flood and ebb pumping is less than in the turbine mode. With a runner diameter of $D = 5$ m and a suction head of $h_s = -2.4$ m, pumping at $\varphi = 0.328$, where the maximum efficiency is reached, results in a maximum pumping head H of 4.10 m. The head limitation stems from the generator capacity, which is usually determined with regard to the turbine mode. Under these conditions, the pump operates at a Thoma number of $\sigma_{plant} = 3.06$. As in the turbine mode, the static pressure p_s at the suction side of the machine has to be adjusted for each operating point according to the respective pumping head H in order to achieve a specific Thoma number σ_{plant}.

Turbulence inlet conditions In order to obtain valid simulation results, it is important to set realistic values for parameters that describe turbulence, i.e. the turbulence intensity and length-scale at the inlet boundary of the computation domain. Ideally, exact values are known from measurements or similar applications. Unfortunately, no information is available on the turbulence parameters for the present case or similar turbines in the test rig.

For this reason, the turbulence intensity is assumed to be in the medium range. In the model test setup, there is a perforated grid in the upstream pressure tank in order to smoothen the flow and there are no large turbulence generating components directly upstream of the inlet in the test rig. However, the flow is more complex than a simple large pipe flow and the flow velocity is quite high.

The option *medium (Intensity = 5 %)* was chosen as is recommended in the CFX modeling guide when no data is available [90]. With this option, a turbulence intensity of 5 % and a viscosity ratio of $\mu_t/\mu = 10$ are defined, where μ_t is the turbulent viscosity and μ is the molecular dynamic viscosity.

To evaluate the significance of the turbulent intensity setting for the turbine efficiency, three comparison runs were conducted with different levels of turbulent intensity. There are no significant discrepancies in the results of the three simulations (see Table 3.7).

Table 3.7: Comparison of simulations results with different inlet turbulence intensity

I [–]	n [min^{-1}]	$\dot{m}$ [kg/s]	$\Delta\gamma$ [°]	P_{fl}[W]	P_{me} [W]	η [%]	H_t [m]
low (1 %)	800	475	0	16,084	14,910	92.70	3.453
medium (5 %)	800	475	0	16,102	14,933	92.74	3.457
high (10 %)	800	475	0	16,062	14,913	92.85	3.448

It was therefore decided to perform all the simulations with a turbulence intensity inlet setting of medium (5 %). The outlet boundary condition was set to be an opening. This allows a static pressure to be specified that is distributed equally on the boundary. The velocity profile at the boundary is a result of the computation and backflow into the domain is possible. This is an advantage in comparison to the outlet type "outlet" that does not allow backflow and dynamically places an artificial wall in locations where backflow occurs.

Surface boundary conditions

At all walls, boundary conditions have to be set as well. Any wall boundary condition dictates that no flow can pass through the wall, but there are different possibilities as

to how the numerical model treats the flow perpendicular to the wall.

Free slip wall With the free slip wall boundary condition there is no shear force transfer on the fluid, i.e. the flow can move freely along the wall. It is an appropriate choice if viscous effects can be neglected or if a symmetry surface is to be modeled.

No-slip wall A no-slip wall boundary condition specifies that the flow velocity directly at the wall is equal to the wall velocity, which in many cases is zero. If a physical surface is to be modeled this usually is the appropriate choice. No-slip wall boundary conditions were set on all surfaces.

Wall velocity If the wall velocity at the defined surface is to be non-zero, a wall velocity can be defined. By choosing the option of a counter-rotating wall, the wall velocity is automatically set so that the wall is stationary with respect to the stationary frame. This can be used to simulate a wall as stationary when it is part of a mesh with a rotating frame of reference. The counter-rotating wall velocity can be set at all physically stationary walls and rotating walls can be set to the default no-slip wall boundary condition.

In the turbine design, all walls except the hub and shroud surfaces are stationary, while the surfaces directly at the blades, i.e. the ring carrying the generator and the hub, rotate. During the optimization process, the dimensions of the generator, the length of the blades and the rotating rings at the shroud and hub were not known. Therefore, the hub and shroud surfaces were not split lengthwise into separate sections during the optimization, but were instead treated as a single surface each. The whole length of the runner shroud was simulated with the wall velocity option counter-rotating wall and the hub was simulated with a wall velocity of zero. This approximation was considered to be acceptable, as the rotating surfaces at the blades, i.e. the shroud ring and the hub of the final turbine are comparatively short in comparison to the whole runner domain, as can be seen in Figure 3.14. In simulations of the pumping mode of the final turbine design, the runner domain was split into different sections, as shown in Figure 3.19. This was done in order to increase the model accuracy, because the long rotating hub surface was shown to induce a swirl upstream of the runner blades, which does not occur in real-world conditions.

Wall roughness No-slip walls can be defined as either hydraulically smooth, or rough. For smooth walls, the velocity profile adjacent to the walls is modeled by using wall functions as described in Section 3.2.3. When the roughness of walls is modeled, the logarithmic velocity profile depicted in Figure 3.9 moves closer to the wall

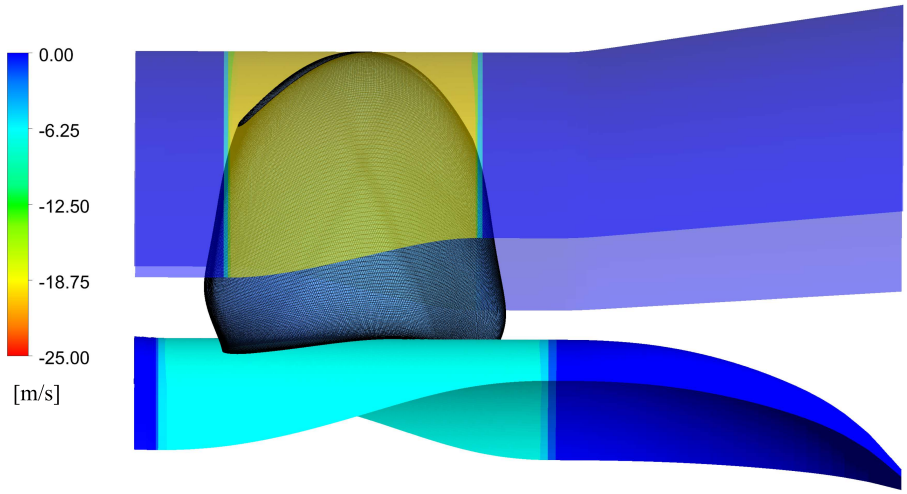

Figure 3.19: The runner domain with rotating hub and shroud surfaces shown in lighter colors

[90]. The magnitude of the shift is dependent on the equivalent sand-grain roughness, which has to be defined as an input. The equivalent sand-grain roughness is highly dependent on the surface quality of the machined parts. Comparative simulations with increasingly rough walls were carried out in order to estimate the effect of the wall roughness on the turbine efficiency. This showed that the turbine efficiency decreases with increasing sand grain roughness, but as the latter is not defined by the turbine design, all subsequent simulations were carried out using the smooth wall option.

Domain Interface Modeling

The computational domain was partitioned into four different domains, which were named inlet domain, guide vane domain, runner domain and outlet domain (see Figure 3.14). In order to combine such different domains into one setup that is treated as a continuous system, methods referred to as domain interfaces have to be implemented. Each interface consists of two domain boundaries that are meant to be connected. These can be boundaries of different domains when flow passes the interface, e.g. the guide vane outlet and the runner domain inlet. It can also be two boundaries of the same mesh, as is the case with rotational periodicities.

ANSYS CFX supports direct connections where each node of a mesh has a corresponding node on the other mesh in the same location, within a small tolerance. Another mesh connection method is the general grid interface (GGI), which is very powerful and flexible. It allows for the mesh elements of the two sides of a domain interface to not line up perfectly and therefore enables non-matching meshes to be connected. This conveniently permits the use of different mesh types and resolutions

in the connected domains and simplifies mesh generation, as varying mesh generating methods can be applied.

Another purpose of domain interfaces is to allow changes in the frame of reference to be modeled. This is the case when, for instance, a rotating domain and a stationary domain are to be connected.

Periodic interfaces Periodic interfaces are made in such a way that the flow leaving one boundary automatically appears on the opposite side. There are two types of periodicity: translational and rotational. In the first case, the periodicity lies on a straight line, while in the latter case it revolves around a straight line.

The rotational periodicity interface is very useful when simulating turbomachinery. The blades of rotating machines are often arranged periodically around the axis of rotation, and all blades have the same geometry. Thus, the flow in each blade passage, i.e.the space between two blades, is considered to be equal. It is therefore sufficient to simulate a single blade passage that represents all the combined blade passages. This approach can save enormous amounts of computational effort and was used for both the guide vane and the runner domain. The number of mesh elements could thus be reduced by 93.75 % and 66.7 %, respectively. The inlet and outlet domain each have a rectangular cross-section at their respective outer ends and thus they are not periodic.

General connection Interfaces The general connection interface model is used to connect regions where grids are non-matching and a frame change is necessary. It was therefore used to connect the inlet to the guide vane domain, the guide vane domain to the runner domain and the runner domain to the outlet domain. None of the corresponding meshes are matching and therefore direct connections are not applicable. Moreover, a pitch change is often necessary when periodic interfaces are used. The boundary of the inlet domain covers the full circular cross-section of the flow passage, while one blade passage of the guide vanes covers 1/16th and one blade passage of the runner covers one-third of the full turbine. The corresponding pitch angles for this case are 360°, 22.5° and 120°.

No frame change was employed between the inlet and the guide vane domain, as both domains are stationary. Between the guide vane domain and the runner as well as between the runner domain and the outlet domain, frame changes from stationary to rotating had to be modeled. ANSYS CFX supports three frame change models that are explained in the following sections.

Frozen rotor With the frozen rotor model, the relative orientation between the stationary guide vane blade passage and the rotor blade passage is fixed. The frame of

reference is transformed in the rotating domain according to the set rotational velocity of the runner. A steady-state solution is calculated and the fluxes between the domains are scaled according to the pitch ratio. Due to the steady-state character of the simulation, no transient effects are resolved. However, effects such as the wake behind the blade and secondary flows are modeled and transferred from one domain to the other. Due to the fixed orientation of runner and guide vanes, these flow phenomena can lead to different results, depending on the exact positioning of the guide vane and rotor blades. When the leading edge of the runner, for example, is located directly in the wake of the guide vane the simulated turbine efficiency is different from when the leading edge is located aside of the wake. To account for this, it is recommended to run multiple simulations with different orientations of the blades relative to each other.

Stage model An alternative frame change model is the mixing-plane method introduced by Denton & Singh in 1979 [105]. In ANSYS CFX it is referred to as stage model. It does not assume a fixed relative position of the two domains but splits the interface radially into multiple bands. In each band, a circumferential averaging of the flow is employed and then the flow is handed over to the corresponding band of the downstream domain. Thus, variations in the flow field in the circumferential direction, such as blade wakes, are neglected. This gives fairly representative results even if the pitch ratio is comparatively large. As in the frozen rotor model, steady-state solutions are calculated for each domain, and therefore transient effects are neglected. According to the Modeling Guide of ANSYS CFX [90] the stage interface "is most appropriate when the circumferential variation of the flow is of the order of the component pitch", which is true in the present case.

The stage model is computationally more costly than the frozen rotor model, but it usually gives more reliable results.

Transient Rotor-Stator If transient effects have to be accounted for, the transient Rotor-Stator model is the method of choice. It uses a sliding interface where the flow passes from one domain to the other. The mesh of the runner domain is rotated stepwise according to the speed of revolution and therefore all relative positions occurring during one full revolution of the runner are simulated. By doing this, the true transient interaction between the guide vanes and the runner can be resolved. This also allows unsteady effects to be resolved. However, the computational effort with this approach is very high. This comes from the fact that a transient solution has to be calculated and no spatial periodicity can be used to reduce the number of blade passages that have to be simulated if the pitch ratio is unequal.

3.3.6 Timescale control

ANSYS CFX uses a fully implicit solver and employs a false timestep in order to stabilize the equations [90]. Selecting a large timescale usually leads to fast convergence, but selecting a too large timescale may result in convergence problems. ANSYS CFX offers three options to control the timescale:

- Auto Timescale
- Local Time Scale Factor
- Physical Time Scale

Auto Timescale is the default option, which dictates that the solver internally calculates an appropriate timescale from information on the boundary conditions, flow conditions, physics and the domain geometry. It usually sets a conservative value, which is robust but not perfectly efficient in terms of convergence. According to [90] selecting an automatic timestep will result in a timestep of $\Delta t = 0.2/\omega$.

With the Local Time Scale method, different timescales are used in different regions of the calculation domain. It uses small timescales where flow velocities are high and large timescales where flow velocities are low. It is most useful for simulations with a wide range of velocities such as jet flow, where velocities change in orders of magnitude. It is however not well suited when elements are small or have a large aspect ratio. In those cases, the local timescale and eventually the convergence rate may become very small. This applies especially to mesh elements in the inflation layers near wall boundaries, for which the aspect ratio approaches 1,000. Therefore this method was not considered applicable in the present study.

The Physical Time Scale option can be used to set a fixed timescale manually. In the present study, a physical timescale of $\Delta t = 1/\omega$ was used. This results in smaller timesteps at higher rotational velocities. With a rotational speed of $n = 900\,\mathrm{min}^{-1}$, which is equal to $\omega = 94.25\,\mathrm{rad/s}$, the timestep size is $0.0106\,\mathrm{s}$. It is recommended to use the quotient of a length scale and a velocity scale. A good estimate for the physical timescale is the time it takes the flow to make its way through the whole domain as recommended by the CFX modeling guide. "For many simulations, a reasonable time estimate t is easy to make based on the length of the fluid domain L , and the mean velocity U" [90]. The guide's example equation is:

$$\Delta t \approx \frac{L}{U} \quad [\mathrm{s}] \tag{3.57}$$

3.3.7 Transient effects

Transient simulations were carried out in order to evaluate time-dependent effects such as vortex shedding, blade wakes, rotor-stator-interactions or unstable flow in the draft tube. They generally give a more realistic prediction of the turbine characteristics as steady-state simulations, however, the computational effort is much higher. The simulation is based on many more mesh elements, as the whole turbine domain has to be simulated. Moreover, not only one steady-state solution of the flow field is computed, but many sequential results, i.e. time steps, are obtained. Each time step is iteratively computed until the desired convergence criterion is reached.

The runner rotation is modeled by incrementally rotating the runner mesh between timesteps according to the rotational speed. The flow passage between different meshes is implemented by a general connection transient rotor-stator interface as described in Section 3.3.5. This method makes it possible to connect nonidentical meshes that slide against each other. A pitch change is not necessary, as the mesh contains the full turbine geometry. Transient simulations are initialized with the solution data of a full circle steady-state simulation that is specifically computed in advance with identical settings. Examples for the application of this method are given in [106] and [107].

3.3.8 Estimation of leakage and friction losses

Both leakage losses and friction losses in the generator gap were not considered in the CFD simulations. The complexity of such simulations would have led to a computational effort that would have been too high. However, the magnitude of these losses was estimated in order to gauge their relevance.

Leakage flow rate

An exact calculation of the flow rate through the gap is very difficult, as the flow has a high rotational velocity, and is generally very complex and different for every machine [79]. Its magnitude can, however, be estimated with Equation 3.19 presented in Section 3.1.5. To estimate the leakage losses in the model turbine at a head of 3 m the friction coefficient has to be approximated. [79] suggests a range for lambda of $\lambda = 0.03...0.06$. The resulting leakage flow rate has a magnitude of $Q_{gp} \approx 0.005\,\mathrm{m}^3/\mathrm{s}$ which is in the range of 1 % of the design flow rate and is quite relevant. Table 3.8 shows the values taken for the calculation.

Table 3.8: Estimate of leakage losses in the model turbine design

$(p_i - p_o)$ [Pa]	L_{gp} [m]	s_{gp} [m]	λ [–]	μ_{gp} [–]	A_{gp} [m^2]	Q_{gp} [m^3/s]
30,000 Pa	0.094	0.001	0.05	0.51	0.00124	0.0049

Gap friction

The gap between the generator rotor and the generator stator has to be relatively thin because otherwise the magnetic field strength weakens and the generator efficiency is impaired. Literature indicates that a thinner gap leads to higher friction losses, as the gradient of velocity between the standing outer wall and the rotating inner wall gets steeper. The disc friction losses were a concern in the development of the project. Consequently, a literature study was conducted to obtain some information on its magnitude.

In [108] a study on the torque resistance of a flow between rotating co-axial cylinders having axial flow is presented which is very similar to the present case. The analysis covers the range of Reynolds numbers needed for the present analysis. However, the range of relative gap width r/s is slightly too low. For the model turbine geometry with a gap width of $s = 0.001$ m and a rotor radius $r_1 = 0.197$ m the relative gap width $s/r_1 = +0.00508$. However, from Figure 3.20 we can deduce that the smaller s/r_1 gets, the more the lines of C_f seem to converge to the same values.

At an operating point of $Q'_1 = 2.42$ m^3/s, $n'_1 = 160$ min^{-1} and $H = 3.0$ m the Reynolds number is $Re_\omega = 1.67 \cdot 10^{-4}$ and the friction coefficient is in the range of $C_f = 0.0008...0.001$. This gives rise to a shear stress on the outer rotor surface of $\tau = 225...285\,\mathrm{N/m^2}$ which in turn creates a friction power of $P_R = 440...550\,\mathrm{W}$. Compared to a turbine power of 12 800 W this is a loss of 3.4 % to 4.3 %. Not included in this estimate is the friction induced by the side walls of the rotor.

By extrapolating the findings presented in [108] and calculating the friction losses we can deduce the following conclusions:

- The generator length is directly proportional to the friction area and therefore friction losses.
- The gap width s influences the friction factor C_f, but the changes are quite small. Increasing s from 0.001 m to 0.005 m results in C_f dropping from 0.0008 to 0.0005.
- The rotational speed n is dominant with $P_r^3 \propto n$, i.e. a doubling of n increases the friction losses eightfold.

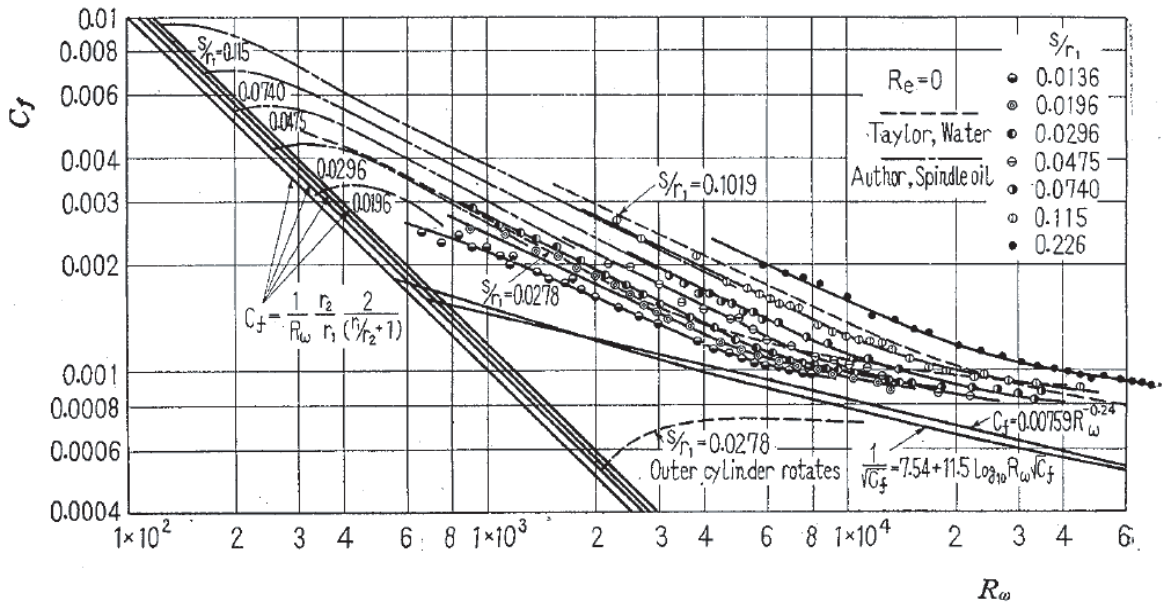

Figure 3.20: The relation between friction coefficient C_f and Reynolds number Re_ω for various s/r_1 ratios [108]

The applicability of these calculations is limited due to the many assumptions made. As shown before there will be a flow in the axial gap of the model turbine, but it is uncertain how much it is exactly. Moreover, the axial flow depends on many variables such as H, n, guide vane angle γ.

3.3.9 Structural mechanical simulations

During the turbine development, a finite element structural mechanical analysis was conducted. Its purpose was to assess whether the defined blade profile would also be feasible from a mechanical point of view. Turbine blades that are very good from a hydrodynamic point of view still have to withstand the mechanical forces during operation. Simulations were carried out for the turbine runner as well as for the guide vanes.

The analysis of the runner was conducted for the design operating point as well as the runaway condition. In both cases, it was found that the maximum stresses within the runner would never exceed the yield strength of typical materials used in turbine manufacturing. The guide vanes were analyzed in relation to the maximum stresses as well as their deformation for two distinct cases. Firstly a case was considered where the vanes were only supported in a ring around the turbine. In the second case, the guide vanes were supported on the outside as well as the inside. In a modal analysis, the natural frequency for both cases was determined. The purpose of the modal analysis was to ensure that the natural frequency of the guide vanes would not be similar to the

blade passing frequency of the runner in the pumping mode. Such a setup could lead to a build-up of vibrations due to resonance. The analysis showed that the natural frequencies and the blade passing frequency are very distinct and no problems should arise.

Chapter 4

Results

In the following chapter, the results of the computational fluid dynamics simulations of the optimized geometry are presented separately for the turbine and pumping modes. Firstly, results of steady-state simulations at different operating points are presented. Secondly comparisons between steady-state and transient simulations for one turbine and pump operating point are shown.

4.1 Steady-state simulation results

Steady-state simulations of the optimized geometry were carried out for a wide range of operating points. This was made possible by using the parameterization capabilities of the simulation software, which allowed for a batch processing of the operating points. Moreover, with steady-state simulations, a solution can be obtained with tolerable computational effort.

4.1.1 Turbine mode

For eight distinct guide vane angles γ, the rotational speed of the runner was altered while keeping the mass flow rate constant at $\dot{m} = 475\,\mathrm{kg/s}$. The hydraulic head adjusts according to the flow phenomena in the turbine. This results in a set of operating points of the turbine, each with an individual combination of unit discharge Q'_1 and unit speed n'_1.

Efficiency

The turbine efficiency $\eta_{tu,IEC}$ was calculated at different unit speeds n'_1 and guide vane angles γ for the complete turbine length, including the inlet and draft tube.

Negative guide vane angles γ indicate a closing of the guide vanes, while $\gamma = 0°$ defines a condition where the incidence angle is zero (see Figure 3.12). The best

efficiency reached is $\eta_{tu,IEC} = 85.0\,\%$ at a unit speed of $n'_1 = 152\,\mathrm{min}^{-1}$ and a guide vane angle of $\gamma = -7.5°$ as depicted in Figure 4.1. For each guide vane setting, the efficiency drops at both lower and higher unit speeds. Additionally, the efficiency drops slightly when the guide vanes are opened up to a angle of $\gamma = 0°$, while the peak efficiency at each guide vane angle stays at the same unit speed approximately $n'_1 = 152\,\mathrm{min}^{-1}$. This reduction in efficiency results from a higher unit discharge, which leads to increased friction losses. At guide vane angles above $\gamma = 0°$, the overall efficiency reduces further, especially at high unit speeds.

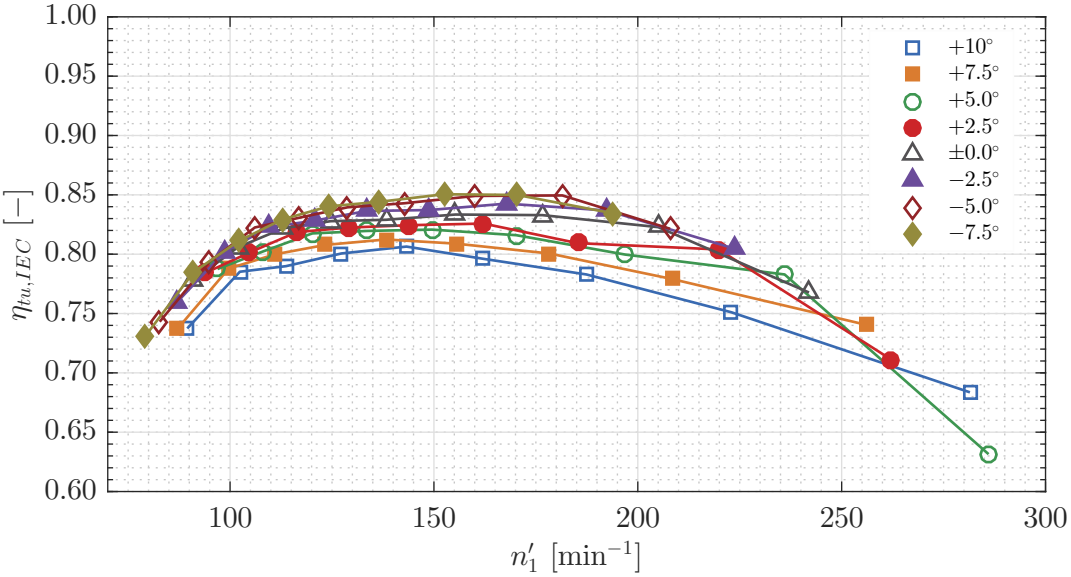

Figure 4.1: Turbine efficiency $\eta_{tu,IEC}$ versus n'_1 at guide vane angles $\gamma = 10.0°$ to $-7.5°$

Loss analysis To identify the optimization potential in the individual components, a loss analysis was conducted. Figure 4.2 depicts the efficiency in turbine mode for a guide vane angle of $\gamma = 0°$ and different unit speeds n'_1. Each line represents the efficiency after adding the losses of one or multiple components. The differences between the various curves indicate the loss of each turbine component as a percentage of the total head.

The losses in the turbine inlet are lower and amount to between $H_{l,in} = 0.4\,\%$ and $1.1\,\%$. The absolute magnitude of the losses is equal for all cases as is the flow rate. However, the total head at high unit speeds is lower, which results in greater values for the relative losses. This shows in a constant slope of the blue curve that represents the efficiency after the inlet.

The losses in the guide vanes are roughly three times as large with values between $H_{l,gv} = 1.2\,\%$ and $3.1\,\%$. The corresponding orange curve has a constant slope as well. The runner losses are very dependent on the unit speed and have a range of

$H_{l,ru} = 3.9\,\%$ to $8.3\,\%$, which is twice as much as the combined losses of the inlet and guide vanes. The runner losses reach a minimum at a runner speed of $n_1' = 138\ \mathrm{min}^{-1}$. In this case, the shock losses are very low, as the angle of the inflow fits very well to the blade angle. This is not the case when the unit speed is lower or higher, resulting in increasing shock losses in the runner. In extreme conditions, there can also be flow separations on the blades which further increases losses.

The losses in the draft tube are the second main contributor to the total losses. They are between $H_{l,dt} = 4.5\,\%$ and $11.1\,\%$ and reach a minimum at $n_1' = 176\ \mathrm{min}^{-1}$, which unfortunately does not coincide with the point of operation where minimum runner losses occur. The high losses at low unit speeds result from a large swirl turning in an opposite direction to the runner rotation, that leads to high friction losses at the draft tube walls.

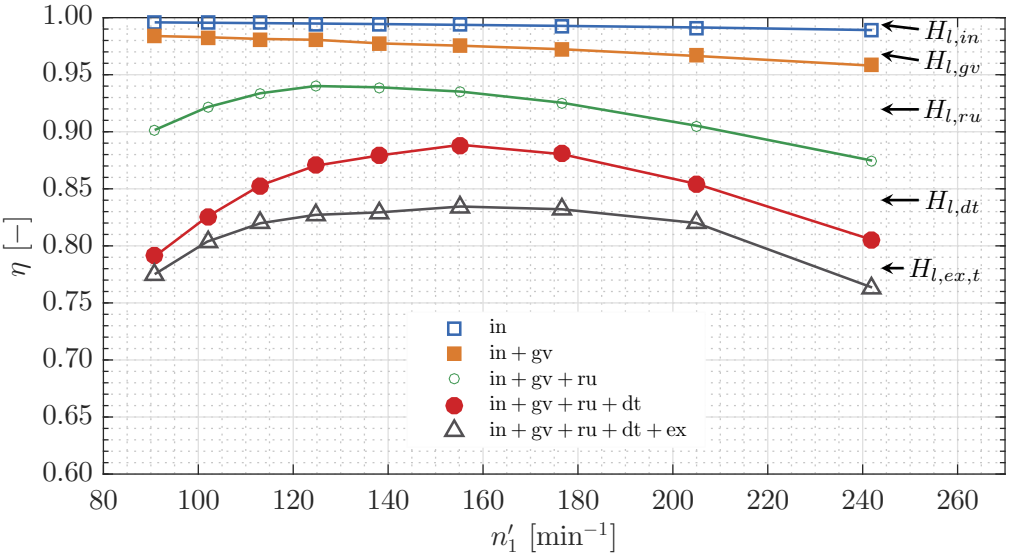

Figure 4.2: Loss analysis of the turbine mode for a guide vane angle of $\gamma = 0°$

Finally, if the nonuniform velocity distribution at the outlet is taken into account, the exit loss based on H_t has to be considered, see Section 3.1.5. This modified exit loss is dependent on the swirl distribution downstream of the runner and the draft tube quality grade. In the present case it reaches its minimum values of $H_{l,ex,t} = 1.6\,\%$ at low unit speeds of $n_1' = 91\ \mathrm{min}^{-1}$. In this case, the total head is high, which reduces the relative effect of the lost kinetic energy at the draft tube outlet. Moreover, the draft tube works quite well, converting most of the kinetic energy available at its inlet into static pressure. At unit speeds of $n_1' = 155\ \mathrm{min}^{-1}$, the modified exit loss has a maximum of $H_{l,ex,t} = 5.4\,\%$. Unfortunately, this coincides with the operating point where the other combined losses are at a minimum. At even higher unit speeds the exit loss are lower again. Figure 4.3 depicts the total pressure p_t and static pressure

p_s along the Z-axis of the turbine for different turbine operating points and a guide vane opening of $\gamma = 0°$. The flow direction is from $-Z$ to $+Z$.

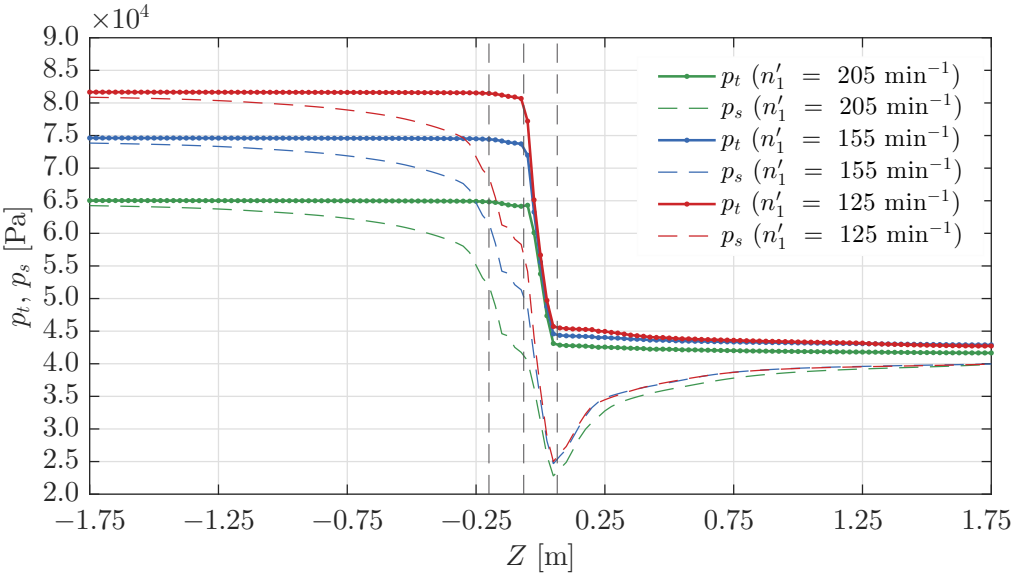

Figure 4.3: Total pressure p_t and static pressure p_s in axial direction at different unit speeds n'_1 and a guide vane angle of $\gamma = 0°$, steady

The difference in inlet and outlet pressure is the hydraulic head and is highest at lower unit speeds. In all cases, the total pressure reduces slightly in the inlet before reaching the guide vanes. This again shows that the losses in the inlet are very low. While passing the guide vanes the total pressure reduces due to the guide vane losses. In the runner, the majority of the total head is removed and converted into mechanical power. In the draft tube, the total pressure reduces again due to losses.

The static pressure is indicated by dashed lines and is almost on the same level as the total pressure at the inlet. The difference between the total pressure and the static pressure is the kinetic energy of the inlet flow. As the velocity is uniformly distributed at the inlet, the kinetic energy is relatively low. The flow is accelerated along the inlet geometry as the cross-section reduces towards the guide vanes. This leads to a reduction of the static pressure. In the guide vanes, the flow cross-section reduces further and a circumferential velocity component is added to the flow. This again increases the absolute flow velocity and the static pressure is reduced further. While passing the runner blades the majority of the static pressure is converted into mechanical power. In the draft tube, the flow is decelerated which leads to an increase in static pressure.

The difference between static pressure and total pressure at the outlet is greater than at the inlet, which is a result of a non-uniform velocity distribution, which contains a higher kinetic energy than a uniform flow. This is due to outlet swirl and a

concentration of high flow velocities in the middle of the draft tube.

When comparing the three cases the following effects can be observed: The losses at inlet and guide vanes almost equal in all three cases. Losses in the draft tube are highest at low n'_1. The draft tube quality grade is highest at high n'_1.

Unit Discharge

Figure 4.4 depicts the unit discharge Q'_1 at different unit speeds n'_1 and guide vane angles γ for the whole turbine, including the inlet and draft tube. The unit discharge Q'_1 increases when the guide vanes are opened. The highest unit discharges are achieved when the guide vanes are opened by 10° above the normal operation. However, efficiencies in these operating modes are limited as shown in Figure 4.1. Within each guide vane setting, the unit discharge increases with rising unit speed n'_1. At each unit speed, a change of the guide vane angle by $\Delta\gamma = 2.5°$ changes the unit discharge by $\Delta Q'_1 = 0.05\,\mathrm{m}^3/\mathrm{s}$. This is true for the whole range of unit speeds.

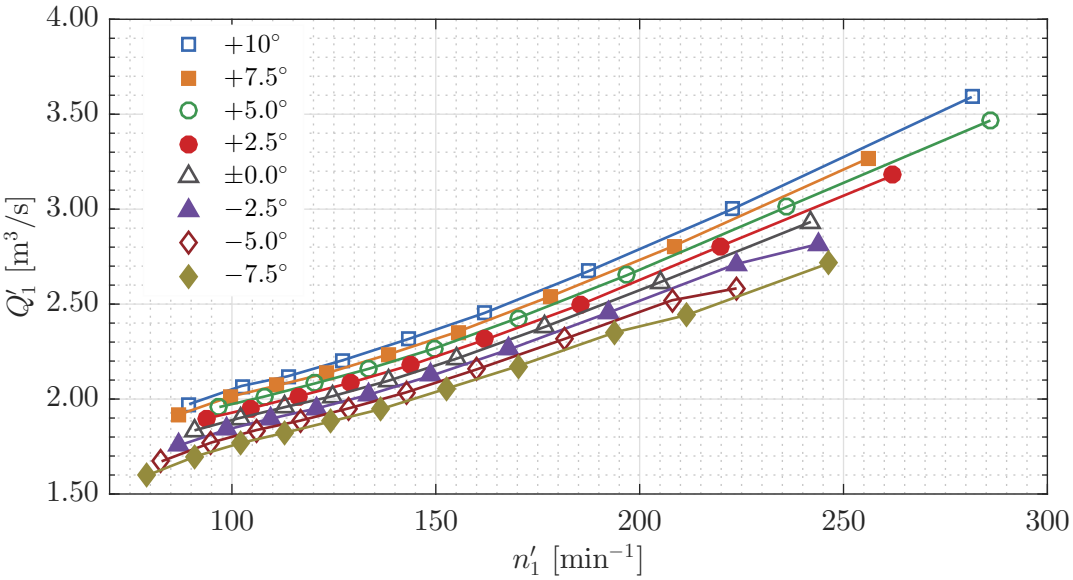

Figure 4.4: Turbine unit discharge Q'_1 versus n'_1 at guide vane angles γ from 10.0° to −7.5°

Meridional and circumferential velocity distribution

Figures 4.5 to 4.7 depict the distributions of $r \cdot c_u$ and c_m at different unit speeds. The variables were determined on a plane upstream of the guide vanes, a plane between the guide vanes and the runner and a plane downstream on the runner. The magnitude of $r \cdot c_u$ is a measure for the angular momentum, or swirl, of the flow. Upstream of the guide vanes, the angular momentum is zero, as the flow does not have a circumferential

velocity component c_u. While the flow passes the guide vanes, a circumferential velocity is introduced, which is then removed while it passes the runner. The difference in angular momentum from upstream to downstream of the runner is equivalent to the Euler Head. It is almost constant over the span in all cases and is highest for a low unit speed and lowest for the high unit speed.

The distribution of $r \cdot c_u$ upstream of the runner is independent of the unit speed, as it only depends on the guide vane angle γ. It is therefore very similar in all three operating points. The distribution of $r \cdot c_u$ downstream of the runner, however, is very dependent on the unit speed. At a low unit speed of $n_1' = 126\ \mathrm{min}^{-1}$, $r \cdot c_u$ has negative values over a wide range of the spans, with values of $r \cdot c_u = 0\,\mathrm{m}^2/\mathrm{s}$ near the shroud, i.e. $S = 1$. This means that the flow has a swirl with a rotation direction opposite to the rotation direction of the runner which is generally not favorable.

At a medium unit speed of $n_1' = 155\ \mathrm{min}^{-1}$, the angular momentum distribution at midspan, i.e. $S = 0.5$, is close to zero, with negative values near the hub, i.e. $S = 0$, and positive values near the shroud, i.e. $S = 1$. The overall magnitude of swirl downstream of the runner is lower and therefore is much more favorable than at low unit speeds. At a high unit speed of $n_1' = 205\ \mathrm{min}^{-1}$, the distribution of $r \cdot c_u$ mostly has positive values, starting with $r \cdot c_u = 0\,\mathrm{m}^2/\mathrm{s}$ at the hub and increasing with rising span up to a value of $r \cdot c_u = 0.25\,\mathrm{m}^2/\mathrm{s}$ near the shroud. This indicates that the flow has a swirl with a rotation direction equal to the rotation direction of the runner which is also not favorable.

A uniform distribution of the meridional velocity c_m over the span indicates that the flow is balanced. In all three operating points, c_m upstream of the runner has values of $6\,\mathrm{m/s}$ over the whole span. The meridional velocity is lower only in vicinity to the hub and the shroud, where $c_m = 0\,\mathrm{m/s}$ is dictated by the no-slip wall boundary condition. Upstream of the guide vanes, c_m has a lower magnitude than at the other cross-sections, due to a larger flow cross-section. The flow has a slightly larger velocity near the hub, but otherwise has a magnitude of around $c_m = 5\,\mathrm{m/s}$. The cross-section downstream of the runner is equal to the cross-section upstream of the runner. The mean values of c_m thus must have the same magnitude. At $n_1' = 126\ \mathrm{min}^{-1}$, the flow gets shifted towards the hub, where its velocity is higher than upstream of the runner. Conversely, the velocity gets slower at the shroud. This is also true for $n_1' = 155\ \mathrm{min}^{-1}$, but to a lesser degree. At $n_1' = 205\ \mathrm{min}^{-1}$ the c_m distributions up- and downstream of the runner are practically equal.

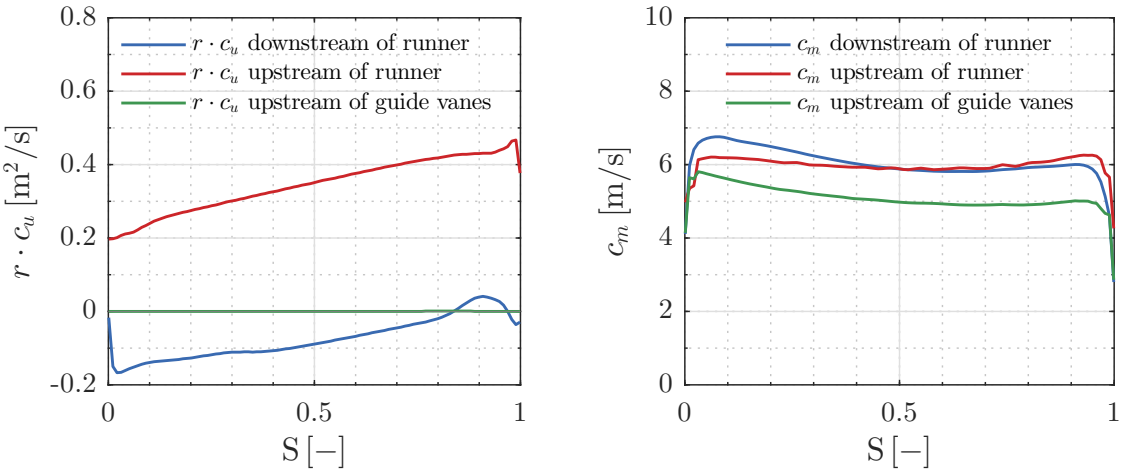

Figure 4.5: $r \cdot c_u$ and c_m in turbine mode, $\gamma = 0°$, $n_1' = 126$ min^{-1}

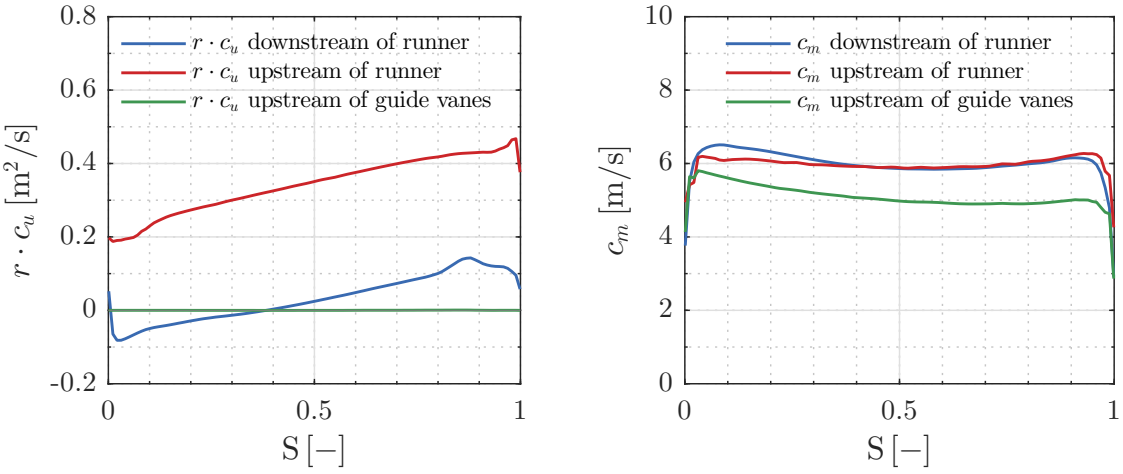

Figure 4.6: $r \cdot c_u$ and c_m in turbine mode, $\gamma = 0°$, $n_1' = 155$ min^{-1}

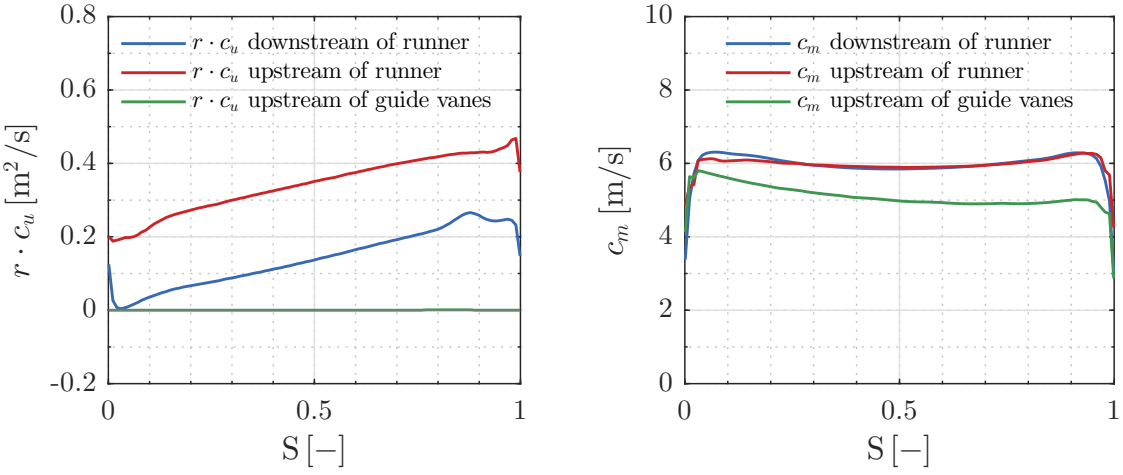

Figure 4.7: $r \cdot c_u$ and c_m in turbine mode, $\gamma = 0°$, $n_1' = 205$ min^{-1}

Blade loading

Figures 4.8 to 4.10 depict the blade loading on the guide vanes and runner blades on spans between $S = 0.05$–0.95 and at the three unit speeds of $n_1' = 126$, $n_1' = 155$ and $n_1' = 205$. As described in Section 3.3.5, the static pressure p_s was adjusted individually for the three operating points so that the turbine operates at a Thoma number of $\sigma = 1.57$. In these figures the vapor pressure of water p_{va} is also taken into account, so that Δp_s represents the pressure exceeding the vapor pressure, i.e. $\Delta p_s = p_s - p_{va}$. The blade loading is represented by the distribution of Δp_s on the pressure and suction side of the profiles in streamwise direction, i.e. between the leading and trailing edge. The normalized streamwise distance is expressed by the variable SW, with $SW = 0$ representing the leading edge and $SW = 1$ representing the trailing edge. On the runner blades, the Δp_s distribution ideally would have a shape that resembles a rectangle or cigar, i.e. the pressure difference between the suction and pressure side is constant in the streamwise direction. Another favorable characteristic is that the pressure does not increase along the suction side, as this would entail a risk of flow separation.

The mean pressure Δp_s on the guide vanes is higher than on the runner blades, as the cross-section reduces towards the runner, which leads to an acceleration of the meridional velocity and therefore a reduction in pressure. At the guide vane leading edge, i.e. at $SW = 0$, the flow splits and takes two paths, i.e. on the suction side and the pressure side of the guide vane. Locally, this split results in a large difference in pressure, since the flow is strongly accelerated as it follows the contour of the blade tip at the suction side, which leads to a low-pressure region. The static pressure difference between the suction and pressure side of the guide vanes is lowest near the shroud, i.e. $S = 0.95$, and highest near the hub, i.e. $S = 0.0$. This comes from the fact that the deflection is lowest near the shroud and takes place along a longer profile length of the vanes. The mean pressure level is slightly higher near the shroud and slightly reduces in streamwise direction on all spans. The pressure distribution on the guide vanes generally is very similar for all unit speeds, however, the overall pressure level is highest at $n_1' = 126$ min^{-1} and lowest at $n_1' = 205$ min^{-1}. The pressure difference in streamwise direction is constant on all spans between $S = 0.2$ and $S = 0.8$ and then converges to equal pressure at the trailing edge. In all operating points the static pressure p_s is well above the vapor pressure of water and therefore no cavitation is expected to occur at the guide vanes.

The blade loading, i.e. the pressure difference between the suction and pressure side of the runner blades, is highest for low unit speeds. This is as expected because the head H is high in these cases. At $n_1' = 126$ min^{-1}, there is a large pressure difference

at the leading edge, with very low pressures on the suction side of the blades. This area of low pressure extends up to a streamwise distance of $SW = 0.2$ at the innermost and outermost spans. At spans between $S = 0.25$ and $S = 0.75$, the zone is narrower, only reaching up to a streamwise position of $SW = 0.1$. The static pressure p_s in these areas goes below the vapor pressure of water, i.e. $\Delta p_s = 0$, and therefore cavitation is likely to occur in this operating point. At a higher streamwise distance, the pressure distribution reaches a plateau on all spans. The pressure on the pressure side of the blade constantly declines from the leading edge towards the trailing edge. Towards the trailing edge, i.e. $SW > 0.9$, the pressure of the suction and pressure side of the blades converges rapidly. The pressure distributions on all spans are generally very similar.

At $n_1' = 155$ min^{-1}, the overall pressure level Δp_s is lower, which stems from the adjustment to constant σ. The pressure distribution at the leading edge is, however, more favorable than at $n_1' = 126$ min^{-1}. There are small excess pressures at the leading edge and large low-pressures at outer spans where $S = 0.75$–0.95. The pressure distribution on the suction and pressure side is constant and similar on all spans. Overall, the pressure distribution in this operating point is very favorable and resembles an ideal shape, apart from a little shock at the leading edge. The only place where the pressure is below the vapor pressure p_{va} is at the outermost spans where $S = 0.75$–0.95. However, as the streamwise extension of this potential cavitation zone is very short, cavitation will probably not occur, as the transit time of the fluid is too short for the evaporation process to take place.

At $n_1' = 205$ min^{-1}, the overall blade loading is lower due to the low head. The low-pressure zone at the leading edge almost completely disappears. The pressures of the suction and pressure side of the runner blades cross at the leading edge, as the negative incidence angle of the inflow leads to a shock, producing a suction peak on the pressure side of the blade leading edge. The pressure distribution on all spans is very similar and almost constant over the streamwise direction. The overall pressure distribution has a favorable shape and indicates a completely cavitation free operation at $\sigma = 1.57$.

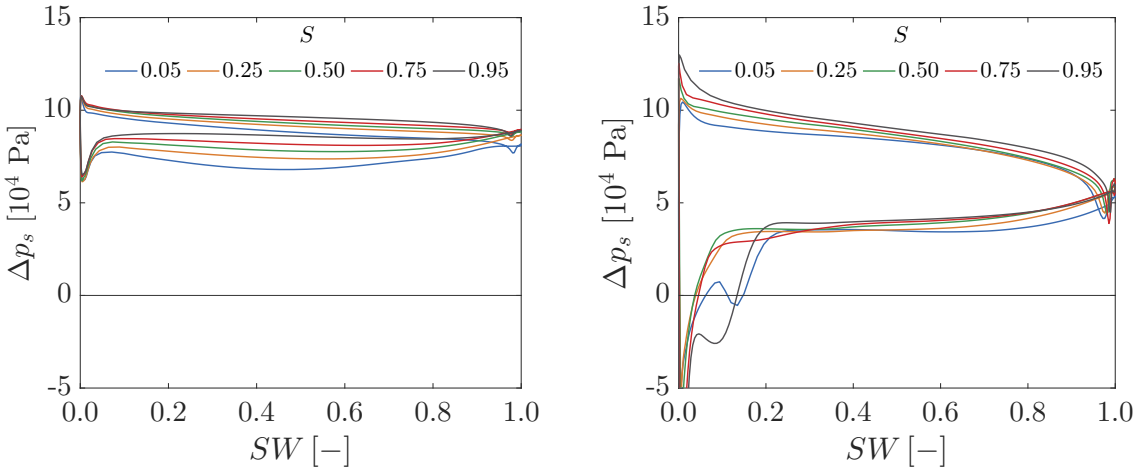

Figure 4.8: Δp_s on guide vanes (l) and runner blades (r) at $n_1' = 126$ min$^{-1}, \sigma = 1.57$

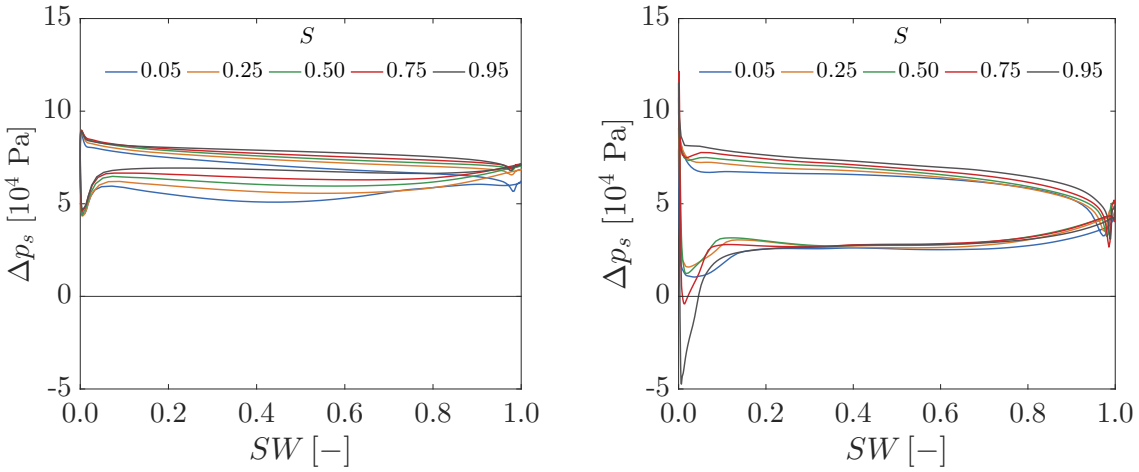

Figure 4.9: Δp_s on guide vanes (l) and runner blades (r) at $n_1' = 155$ min$^{-1}, \sigma = 1.57$

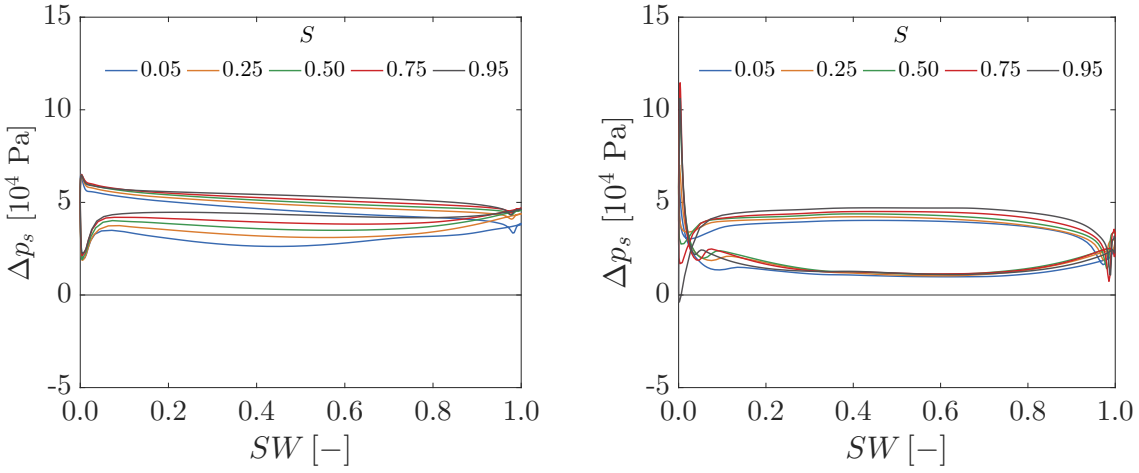

Figure 4.10: Δp_s on guide vanes (l) and runner blades (r) at $n_1' = 205$ min$^{-1}, \sigma = 1.57$

4.1.2 Pumping mode

The pumping mode was simulated for guide vane angles from $\gamma = 10°$ to $\gamma = -10°$ and for flow coefficients from $\varphi = 0.173$ to $\varphi = 0.368$.

Efficiency

The peak pumping efficiency of $\eta_{pu,IEC} = 70.8\,\%$ is achieved at a guide vane angle of $\gamma = 5.5°$ at a flow coefficient of $\varphi = 0.295$, as is depicted in Figure 4.11. Efficiencies are very similar for guide vane angles between $\gamma = 0°$ and $+5.5°$. Here the highest efficiencies are found in the range around $\varphi = 0.325$. When the guide vanes are opened too far, i.e. $\gamma = +10°$, the maximum efficiency drops and equally if the guide vanes are closed too far, i.e. $\gamma \leq 0°$.

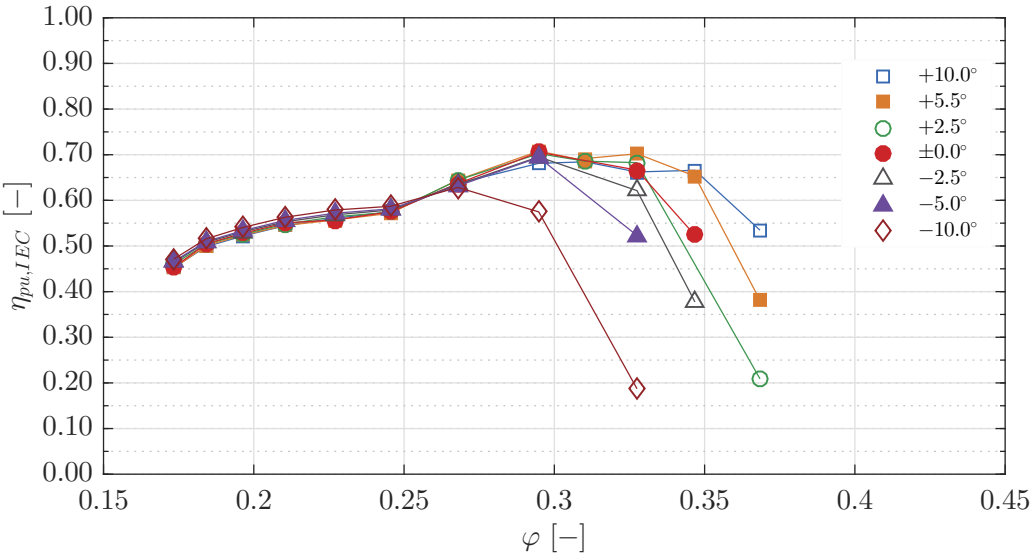

Figure 4.11: Pumping efficiency $\eta_{pu,IEC}$ for guide vane angles γ from 10° to −10°

At high flow coefficients, a steep decline of the efficiency is observed. Due to the increasing meridional component c_m, the incidence angle at the leading edge of the runner becomes negative and the delivery head becomes very low and approaches zero. This effect is most pronounced at low guide vane openings, which can be observed in the efficiency curves for $\gamma = -10°$ and $-5°$. At the same time, the friction losses grow in a quadratically proportional manner to the flow coefficient.

At operating points $\varphi \leq 0.275$, the efficiency decreases as well, although the decrease is less steep than at $\varphi > 0.325$. The efficiency trend in this region is equal for all guide vane angles, as the majority of the losses arise at the runner and in the diffuser. A more detailed breakdown of the individual losses is given in the following loss analysis.

An efficient operation in pumping mode is only possible in a limited range of flow coefficients φ, where the rotational speed of the runner fits well to the incoming flow, i.e. where the incidence angle at the runner blades leading edge is low. At this optimal flow coefficient, the downstream guide vanes then are adjusted to an angle where they work best, i.e. where no flow separation occurs and most of the swirl produced by the runner is converted into static pressure. As can be seen from Figures 4.11 and 4.14, there is no benefit in adapting the guide vane setting for other points of operation, except for pumping at very low flow rates. However, operation in this range should be avoided as the efficiency is very low here. A speed variable operation of the pump makes it possible to always run it at the optimal operation point and thus allows it to work efficiently in different conditions.

Loss analysis Figure 4.12 depicts the efficiency in pumping mode at a guide vane angle of $\gamma = 5.5°$ and varying flow coefficient φ. Each line represents the efficiency after subtracting losses of one or multiple components. The differences between the various curves indicate the loss arising in each turbine component as a percentage of the total head. Note that the naming of the control sections has not been changed when switching from turbine simulations to pump simulations. Thus, in pumping mode, the flow enters the domain at the turbine draft tube and leaves the domain at the turbine inlet. The relative losses in the turbine draft tube, where the flow enters

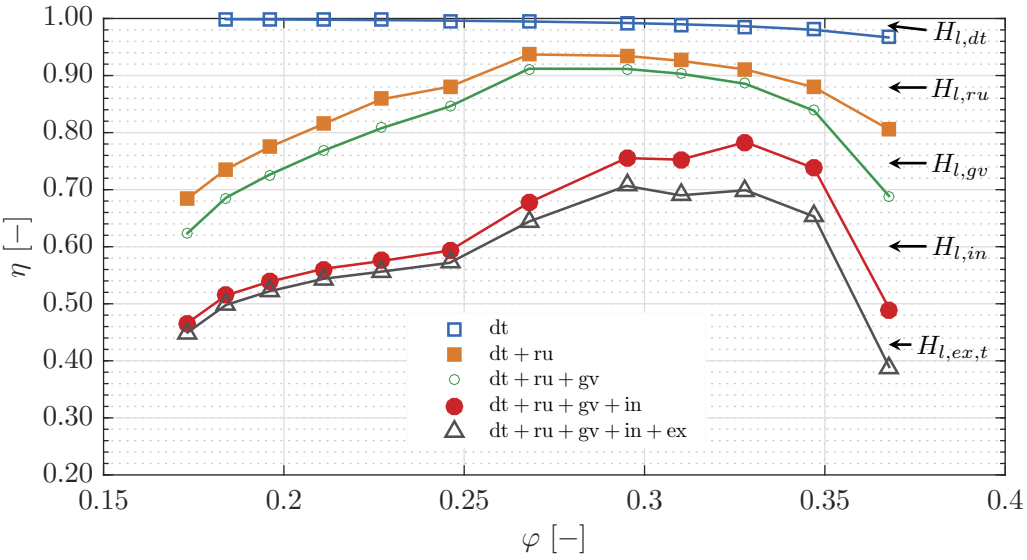

Figure 4.12: Loss analysis of the pumping mode for a guide vane angle of $\gamma = 5.5°$

the domain, are comparatively low and increase with the flow coefficient φ. As in the simulations the flow rate Q was kept constant, and the absolute losses in this part of the domain remain constant, but the total head H_t decreases with rising φ, so that

the relative losses grow. At $\varphi = 0.184$, the losses amount to $H_{l,dt} = 0.13\,\%$ and they grow to $H_{l,dt} = 3.4\,\%$ at $\varphi = 0.368$.

The losses in the runner are more substantial and range from a maximum of $H_{l,ru} = 34.3\,\%$ at $\varphi = 0.173$ to a minimum of $H_{l,ru} = 6.4\,\%$ at $\varphi = 0.310$, where the flow enters the runner blade profiles with an incidence angle is near zero. Towards higher flow coefficients the friction losses increase quadratically proportional to the flow coefficient. At $\varphi = 0.368$, the runner losses add up to $H_{l,ru} = 16.2\,\%$. For flow coefficients below $\varphi = 0.268$, the runner losses grow substantially as the incidence angle at the runner blade leading edge increases, with subsequently extending zones of flow separations on the suction side of the runner blades. These even lead to a region of recirculation flow near the hub that grows with lowering φ. The total magnitude and variation in guide vane losses are lower, with values between a minimum of $H_{l,gv} = 2.3\,\%$ at $\varphi = 0.310$ and a maximum of $H_{l,gv} = 11.7\,\%$ at $\varphi = 0.368$. As in the runner, the losses are minimal when the flow approaching the guide vanes has a incidence angle near zero. When deviating from this operating point towards lower φ, the losses grow due to shock losses and areas of flow separation that begin near the hub and grow with increasingly smaller values of φ. At higher values of φ, the reduced head H_t, as in the other components, leads to higher losses.

Overall, the greatest losses occur in the turbine inlet, which acts as a diffuser in the pumping mode. The losses are very high at any flow coefficient lower than $\varphi = 0.328$, where flow separation on the guide vanes starts to occur near the hub. With lower values of φ, these regions of flow separation grow larger from the hub towards the shroud, note c_m in Figures 4.15 to Figures 4.17 and 4.27. As a result, most of the fluid transport is concentrated in the area near the shroud, while the flow stagnates at the hub. Overall, this adverse velocity distribution entering the diffuser does not allow for it to fulfill its function properly – most of the kinetic energy is dissipated instead of being reconverted to pressure. The diffuser losses are lowest at flow rates between $\varphi = 0.328$ and $\varphi = 0.347$, where the meridional component c_m is rather uniformly distributed. Here, the diffuser losses are limited to only approximately 10 % of the total head H_t. Unfortunately, the region of best diffuser performance does not coincide completely with the operating range where the runner and guide vanes show the best performance, which is between $\varphi = 0.268$ and $\varphi = 0.328$. This apparent mismatch could not be resolved by further geometry optimization due to constraints coming from the turbine operation.

The exit losses due to the non-uniformity of the exit velocity distribution generally increase with a rising flow coefficient φ; they rise from $H_{l,ex,t} = 1.7\,\%$ at $\varphi = 0.173$ to $H_{l,ex,t} = 10.3\,\%$ at $\varphi = 0.368$. This can be explained by the head H_t decreasing

from low towards high flow coefficients φ, while the flow rate Q remains constant. Thus, the proportion of kinetic energy to head increases with rising φ. Therefore, the kinetic energy lost at the outlet $H_{l,ex,t}$ plays a significant role at high flow coefficients φ, where H_t is low, while it makes only a relatively low contribution to the overall losses at low flow coefficients, where H_t is high. Altogether, this explains why there is only a relatively narrow range of flow coefficients in which the pump is operating at acceptable efficiencies. However, this was not considered to be a serious limitation, as the variable speed operation of the machine allows the operating point to be kept within a very narrow range.

Figure 4.13 depicts the total pressure p_t and static pressure p_s along the Z-axis of the turbine for three pumping operating points and a guide vane angle of $\gamma = 5.5°$. The flow goes from $+Z$ to $-Z$, i.e. from the right to the left in the graphic.

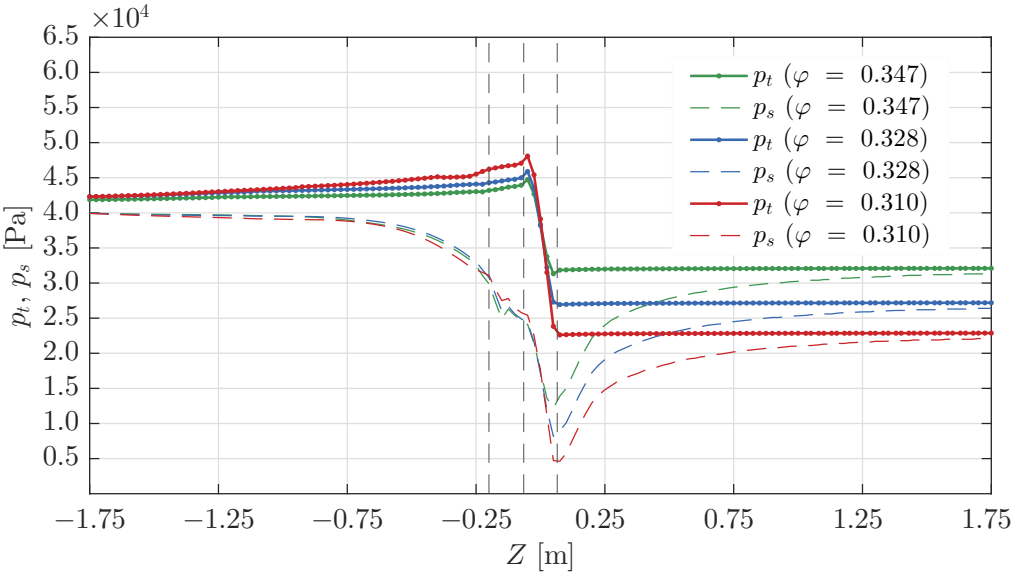

Figure 4.13: Total pressure p_t and static pressure p_s in axial direction at different flow numbers φ and a guide vane angle of $\gamma = 5.5°$

After entering the draft tube at $Z = +1.75$ m the flow accelerates, which results in a reduction of static pressure p_s. The total pressure p_t stays relatively constant, which indicates that losses are very low. At around $Z = 0$ m, between the first and second dotted line, the flow passes the runner and the total and static pressures are increased rapidly, as mechanical work is put into the flow. This increase is highest for $\varphi = 0.310$ and lowest for $\varphi = 0.347$. While passing the guide vanes p_s is increased further, as c_u is decreased and the flow generally is decelerated. From behind the guide vanes at $Z = -0.25$ m the static pressure rise continues. However, between $Z = -0.75$ m and $Z = -1.75$ m there is almost no increase in static pressure p_s. This indicates that the draft tube is not working properly in this section. The core

region with backflow, that persists in the draft tube center, grows in diameter along the draft tube length so that the deceleration of the flow near the shroud is limited. The total pressure p_t reduces along the guide vanes and inlet structure, which can be attributed to losses. These losses are highest for $\varphi = 0.310$ and lowest for $\varphi = 0.347$.

Head curves

Figure 4.14 depicts the head curves in non-dimensional form, i.e. the head coefficient ψ over the flow coefficient φ for guide vane angles γ between 10° and −10°. The curves

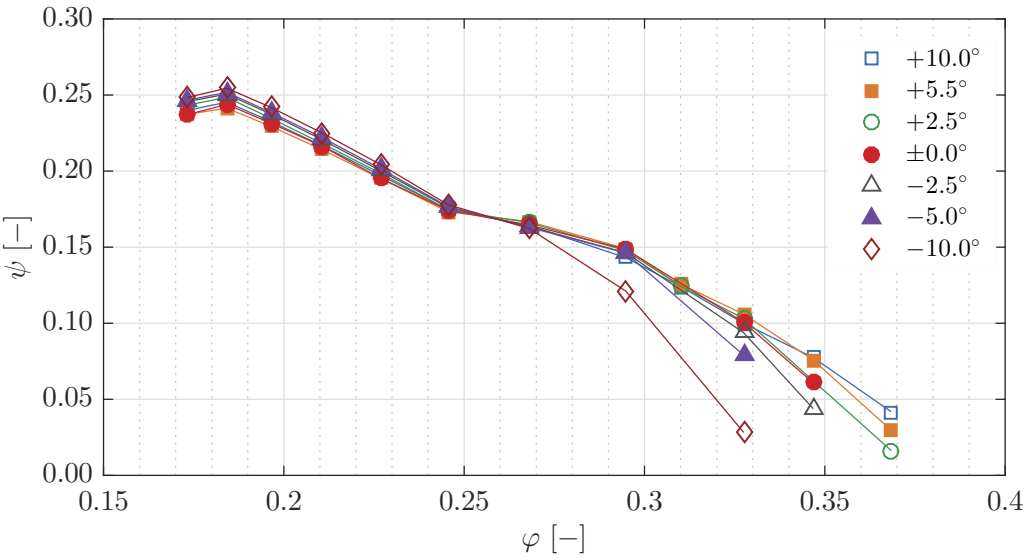

Figure 4.14: Head curves in pumping mode for guide vane angles $\gamma = 10.0°$ to $-10.0°$

generally have a similar course, i.e. ψ increases with lower φ, which relates to a higher rotational speed of the runner with respect to the flow rate, i.e. more head is produced. The curves are almost linear and only have a short plateau between $\varphi = 0.25$ and 0.3. The highest head coefficient overall is reached with a guide vane angle of −10°. At this operating point there is a very large positive incidence angle at the guide vane leading edge which leads to flow separations and a reduced guide vane functionality. By closing the guide vanes, this incidence angle is reduced, which in turn improves the guide vane performance, resulting in a higher head coefficient ψ. The head coefficient at the best efficiency point, at $\varphi = 0.295$, is $\psi = 0.149$ at a guide vane angle of $\gamma = 5.5$. This value lies well within the typical range of 0.11 to 0.159 given by [79] for axial pumps with a hub ratio of 0.35. In the range below $\varphi = 0.27$, the curves spread. In this range, the head coefficient ψ at guide vane angles deviating from $\gamma = 5.5°$ tends to be lower, which is most prominent for $\gamma = -10°$. In this setting there is a negative incidence angle at the leading edge, resulting in flow separations at the pressure side and a malfunctioning of the guide vanes.

Meridional and circumferential velocity distributions

In order to further analyze the flow properties in pumping mode, three operating points at different flow coefficients from $\varphi = 0.347$ to $\varphi = 0.310$ are studied in detail. The $r \cdot c_u$ distribution upstream of the runner is zero over the whole span, as the incoming flow has no circumferential component. This is true for all operating points and shown in Figures 4.15 to 4.17. After passing the runner, the flow has a significant swirl, which is represented by a high magnitude of $r \cdot c_u$. The negative sign indicates that the rotation direction is reversed with respect to the turbine mode. In all three operating points, the circumferential component c_u is increased near the shroud, i.e. $S = 1$, which stems from the rotating shroud ring. Towards the hub, the values decrease slightly in a linear fashion. In the region near the hub, i.e. $S = 0$ to $S = 0.05$, there is a region of increased values of $r \cdot c_u$, which is induced by the rotating hub surface. In general, $r \cdot c_u$ has a higher magnitude for operating points with small flow coefficients φ, as these correspond to a higher head.

The flow then passes the guide vanes, where the circumferential flow component c_u is reduced, i.e. swirl is taken out of the flow, and the kinetic energy contained in it is converted into static pressure. Downstream of the guide vanes some residual swirl is still existent in all three cases. It his highest for $\varphi = 0.310$ and lowest for $\varphi = 0.347$. The skew of the $r \cdot c_u$ distribution downstream of the guide vanes is equal to the one downstream of the runner. Near the hub, there is a region with increased values of $r \cdot c_u$. In this case, the reduction of circumferential velocity is limited. The extent of this region grows from a span of $S = 0.1$ at $\varphi = 0.347$ to $S = 0.3$ at $\varphi = 0.310$. The reason for this is flow separation in the guide vanes near the hub. The meridional velocity c_m upstream of the runner is very constant over the span in all operating modes, with values of $c_m = -6\,\mathrm{m/s}$. It is only lowered at the hub and shroud due to the no-slip condition of the wall boundaries. The negative sign of the velocity indicates a reversed flow direction in comparison to the turbine mode.

After passing the runner the c_m distribution is skewed with values of up to $c_m = -5.6\,\mathrm{m/s}$ near the hub and $c_m = -6.7\,\mathrm{m/s}$ near the shroud. This skewness increases when φ is lowered. At $\varphi = 0.310$, the corresponding values are $c_m = -5.0\,\mathrm{m/s}$ near the hub and $c_m = -7.0\,\mathrm{m/s}$ near the shroud. At $\varphi = 0.347$, the c_m distribution is equalized again after the flow passes the guide vanes, i.e. the values are almost constant again, except for the hub and shroud surfaces. The same is not true for $\varphi = 0.328$ and $\varphi = 0.310$. At the hub, a region with significantly lower flow velocities forms, which grows with decreasing φ.

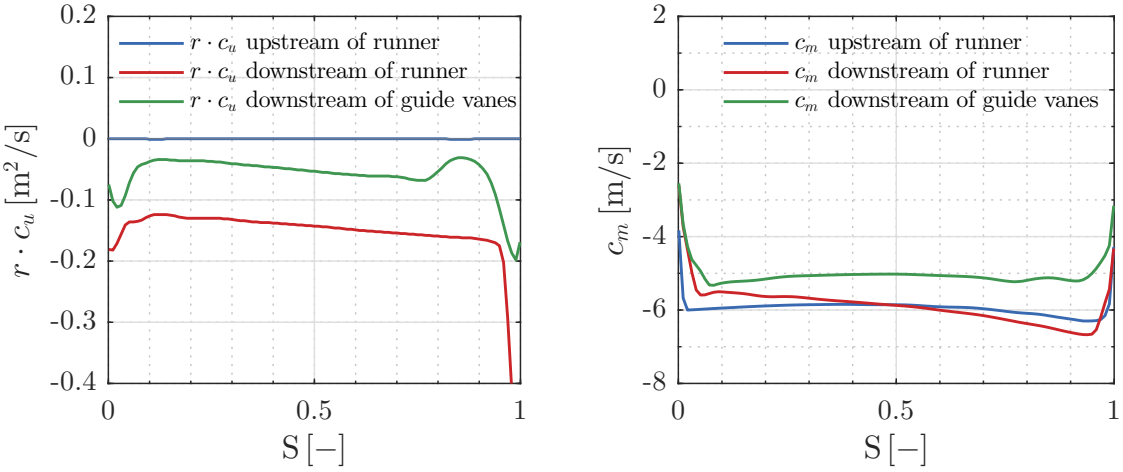

Figure 4.15: Distribution of $r \cdot c_u$ and c_m in pumping mode at $\gamma = 5.5°$, $\varphi = 0.347$

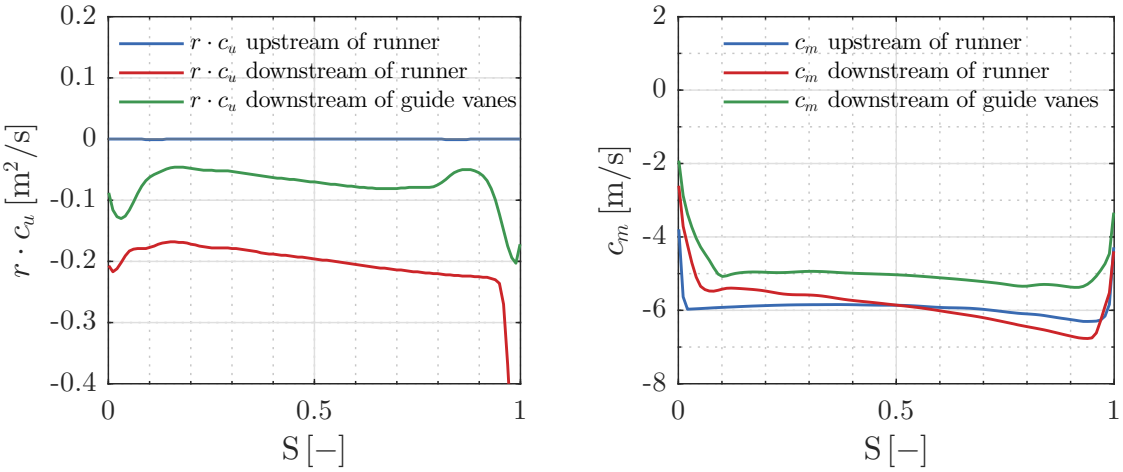

Figure 4.16: Distribution of $r \cdot c_u$ and c_m in pumping mode at $\gamma = 5.5°$, $\varphi = 0.328$

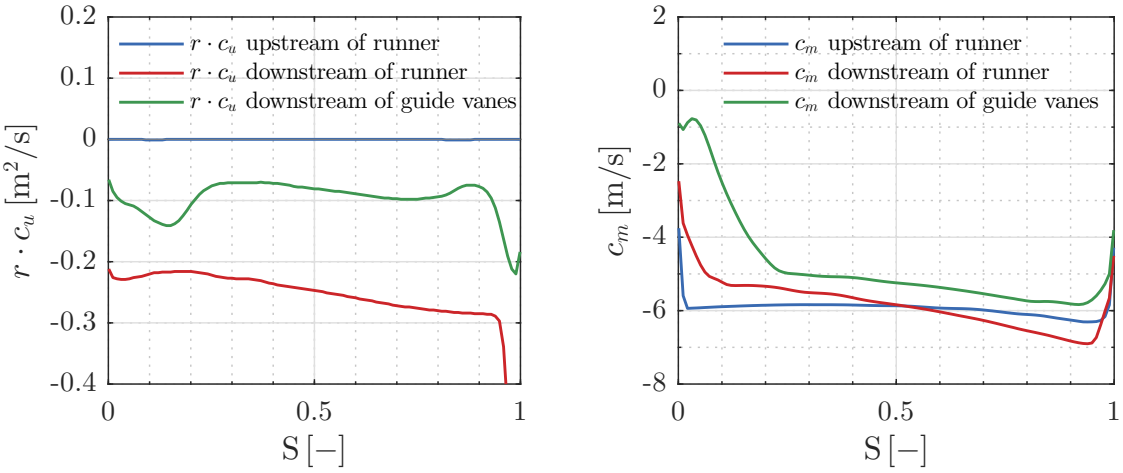

Figure 4.17: Distribution of $r \cdot c_u$ and c_m in pumping mode at $\gamma = 5.5°$, $\varphi = 0.310$

Blade loading

In the pumping mode the flow direction is reversed when compared to the turbine mode, i.e. the water flows from the runner blades to the guide vanes. Figures 4.18 to 4.19 depict the pressure difference Δp_s between the static pressure p_s and the vapor pressure p_v on the runner blades and guide vanes at a Thoma number of $\sigma = 3.06$.

At first, the flow hits the leading edge of the runner blades, where it is split and flows along the pressure and the suction side of the blades.

At a flow coefficient of $\varphi = 0.347$, the pressure lines are crossed at the leading edge, which indicates that there is a high negative incidence angle, leading to an entry shock. The overall pressure level is very close to the vapor pressure p_v and therefore cavitation might occur on the leading edge and the whole length of the suction side of the blades in this operating point. The crossing of pressures at the leading edge is smaller at $\varphi = 0.328$ and not present at $\varphi = 0.310$. At $\varphi = 0.328$ and $\varphi = 0.310$ the overall pressure level is higher and no cavitation is expected to occur. In all three operating points the pressure along the streamwise direction has a relatively constant value on both blade sides. The pressure in the middle of the streamwise direction is very similar on all spans and in all cases. Starting from a streamwise distance of $SW = 0.6$ the pressure on the suction side starts to rise at spans lower than S = 0.75. While this is not a desirable feature, due to the resulting growth of the boundary layer thickness and the increased susceptibility of flow separation, it could only have been avoided by adding more curvature to the blade in this region, which would have compromised the characteristics in the turbine operating mode. Thus, at the trailing edge, the pressure lines cross again in all three cases. With decreasing φ, the pressure difference on the runner blades increases, which means that the total head is increased, i.e. the head coefficient ψ rises. Apart from the previously described pressure rise on the blade suction side, the blade loading has a favorable shape at all operating points, with a constant streamwise pressure difference between the leading and trailing edge.

After leaving the runner the flow approaches the leading edge of the guide vanes, where the pressure lines again cross in all three operating points, due to a negative incidence angle of the inflow. This, again, is a tribute to the turbine mode of operation, where a relatively high curvature of the guide vanes is needed to create a sufficiently high Euler head without unduly high shock losses at the leading edge of the guide vanes. This shock is most prominent at $\varphi = 0.347$. At this operating point, cavitation might also occur at the leading edge of the guide vanes. Operation of the pump at these high discharge rates should thus be avoided. The static pressure difference between the pressure and the suction side of the guide vanes is largest at low spans and lowest at high spans. This can be attributed to the profile length that is longer at higher

spans. Generally, the pressure distribution is similar on all spans, except for a span of $S = 0.05$ where pressures towards the trailing edge are small. Apart from the entry shock, the blade loading on the guide vanes is similar at all three operating points.

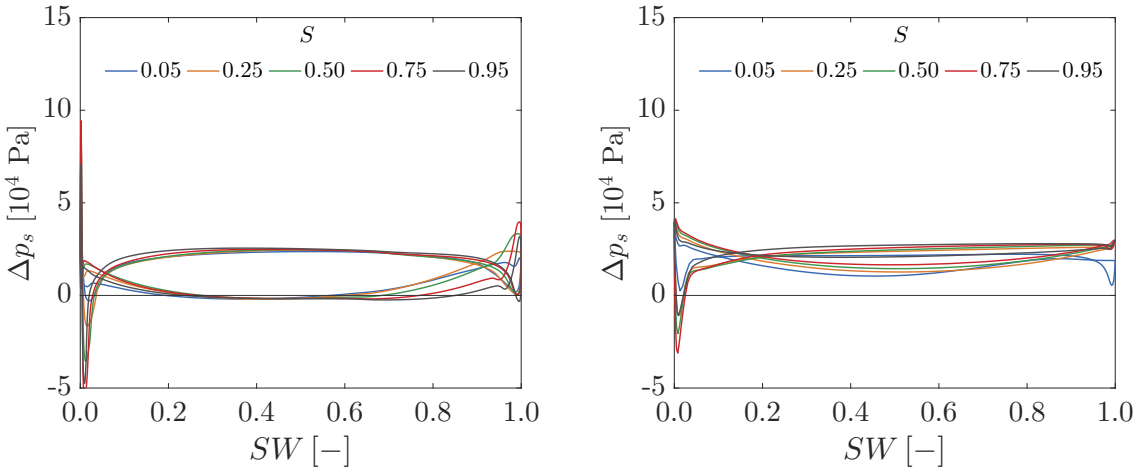

Figure 4.18: Δp_s on runner blades (l) and gv (r), $\gamma = 5.5°$, $\varphi = 0.347$, $\sigma = 3.06$

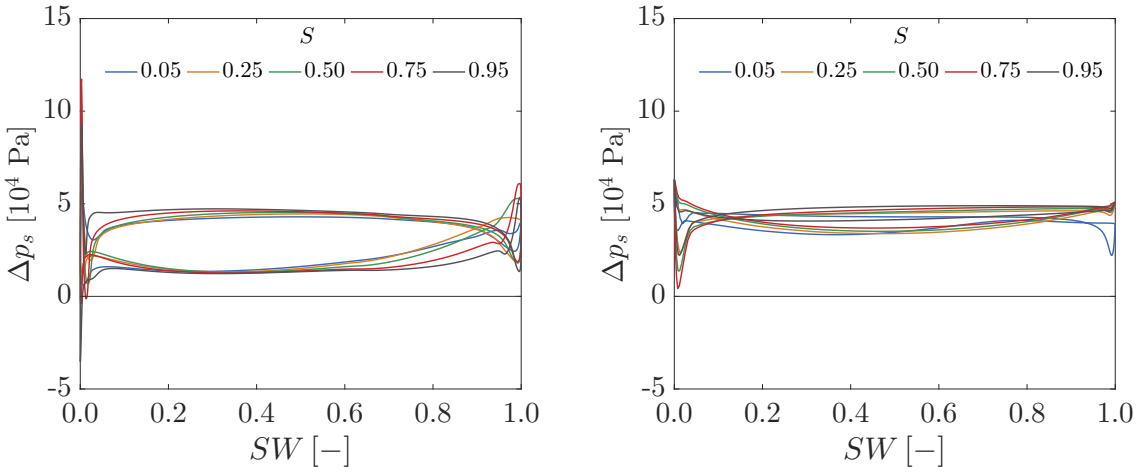

Figure 4.19: Δp_s on runner blades (l) and gv (r), $\gamma = 5.5°$, $\varphi = 0.328$, $\sigma = 3.06$

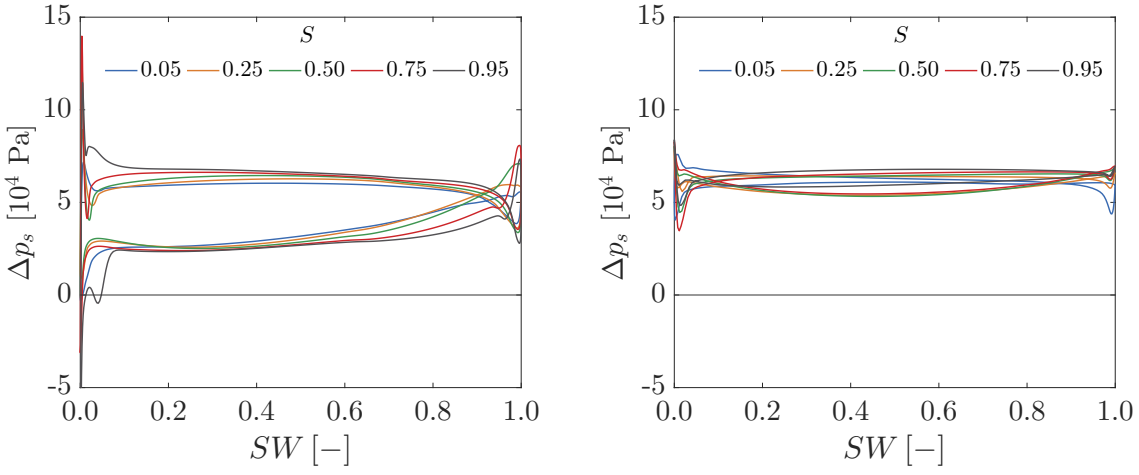

Figure 4.20: Δp_s on runner blades (l) and gv (r), $\gamma = 5.5°$, $\varphi = 0.310$, $\sigma = 3.06$

4.2 Transient simulation results

Transient simulations were computed for a single operating point in both the turbine and pumping mode. Contrary to the steady state simulations, the full extent of the turbine, including all sixteen guide vanes and three runner blades, was simulated. The individual mesh domains were connected by transient rotor-stator interfaces instead of the stage interfaces used in the steady state computations. The extraordinarily high computational effort of these simulations prohibited the simulation of a complete set of operating points that would be suitable for creating a hill chart. The simulations were carried out for two seconds of real-time flow, which corresponds to 28.33 runner revolutions at $n = 850\ \text{min}^{-1}$ in turbine mode and 30 runner revolutions at $n = 900\ \text{min}^{-1}$ in pumping mode. This time period is also approximately twice the fluid transient time from inlet to outlet.

4.2.1 Turbine mode

In the turbine mode the two simulation methods give very similar results. Table 4.1 lists resulting values for selected parameters in order to compare the steady state and transient simulation results.

Table 4.1: Comparison of steady state and transient simulation results in turbine mode

mode	n'_1 [−]	Q'_1 [−]	H_{IEC} [m]	P_{me} [W]	$P_{fl,IEC}$ [W]	$\eta_{tu,IEC}$ [%]
steady state	155.3	2.21	3.46	13,448	16,136	83.3
transient	156.8	2.24	3.40	13,671	15,829	86.4
difference	1.5	0.03	-0.06	223	-307	3.1

At the given discharge, the head H_{IEC} is 0.06 m lower in the transient simulation, which is equal to 1.9 %. This leads to a difference in both the unit speed and unit discharge of 1.0 %. However, the mechanical power P_{me} is 223 W higher in the transient case, which is a difference of 1.6 %. In combination, both these effects lead to a difference in efficiency of $\Delta\eta_{tu,IEC} = 3.1\,\%$. Figure 4.21 depicts the total pressure p_t and static pressure p_s along the Z-axis of the turbine for the steady state and transient simulation. The flow direction is from $-Z$ to $+Z$, i.e. from left to right in the figure. The corresponding curves have a very similar course with only minor differences. In the inlet and guide vanes the losses are predicted to be equal as can be derived from an identical slope of the total pressure p_t. In the runner, the reduction of the total pressure is predicted to be slightly larger in the transient simulation, which also manifests in the mechanical power p_{me} being slightly larger. The resulting losses along the draft

tube are lower in the transient simulation, which can be derived from a lower slope of p_t. Regarding the static pressure, the course of the curves is identical between the turbine inlet and the draft tube inlet, although it is shifted downwards in the transient results. This comes from the fact that the draft tube works better in the transient simulation and a larger portion of the kinetic energy is converted into static pressure between the draft tube inlet and outlet.

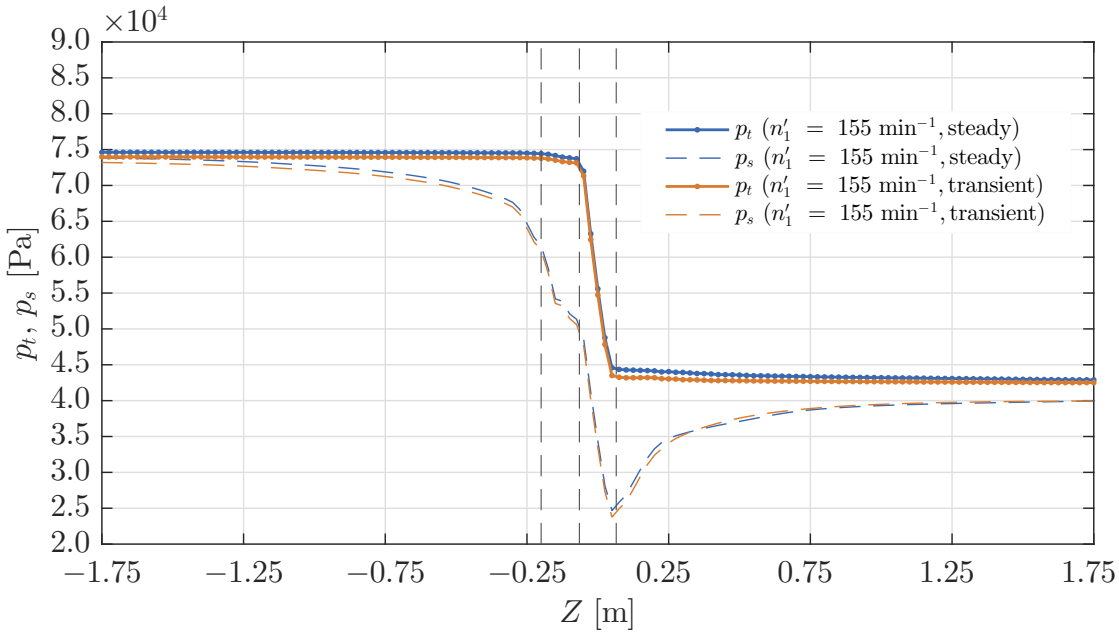

Figure 4.21: Total pressure p_t and static pressure p_s in axial direction in steady state and transient turbine simulation at $n'_1 = 155$ min^{-1} and $\gamma = 0°$

This effect can also be observed in Figures 4.22 and 4.23, which depict the distribution of the meridional velocity c_m on a plane in the Y-Z direction in the steady state and transient simulation, respectively. Note that in the steady state simulation only one guide vane and runner blade passage are simulated and hence only a part of the turbine is shown in this area. The overall velocity distribution is very similar for both cases in the inlet, guide vanes and runner. However, a difference is apparent starting from the draft tube inlet. In the steady state simulation, the flow velocity magnitude is lower near the shroud and draft tube walls and higher in the draft tube center. The difference in velocity might be a result of the different mesh interfaces used, i.e. the stage interface with velocity averaging in the steady state simulation and the transient-rotor-stator interface in the transient simulation.

The difference in the velocity distribution of the draft tube inflow explains the better performance of the draft tube in the transient simulation. There, the flow is decelerated more strongly, which yields a larger static pressure increase. This results in a larger head across the runner and thus more generated mechanical power, while

the overall head between turbine inlet and draft tube outlet is smaller. Overall, this leads to a difference in the efficiency prediction of $\Delta\eta_{tu,IEC} = 3.1\,\%$ between the transient and steady state simulation.

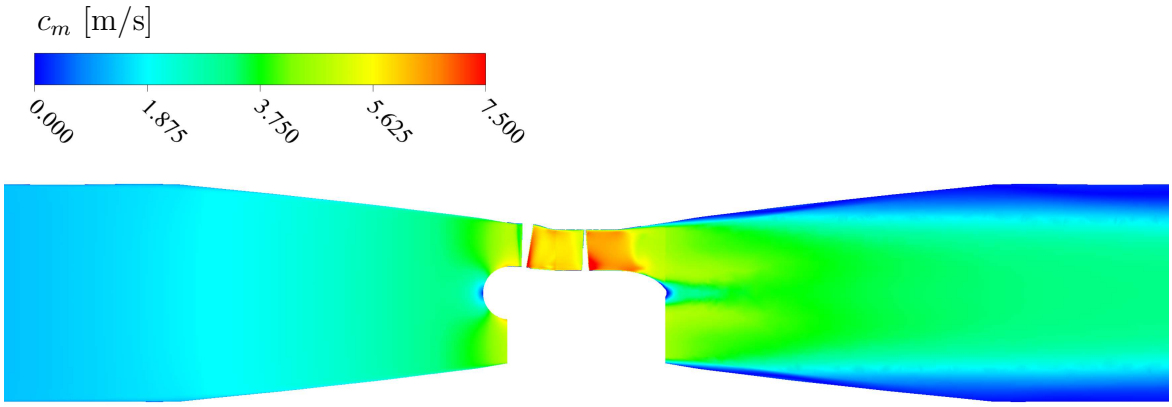

Figure 4.22: Velocity c_m in steady state turbine simulation at $\gamma = 0°$, $n_1' = 155$ min^{-1}

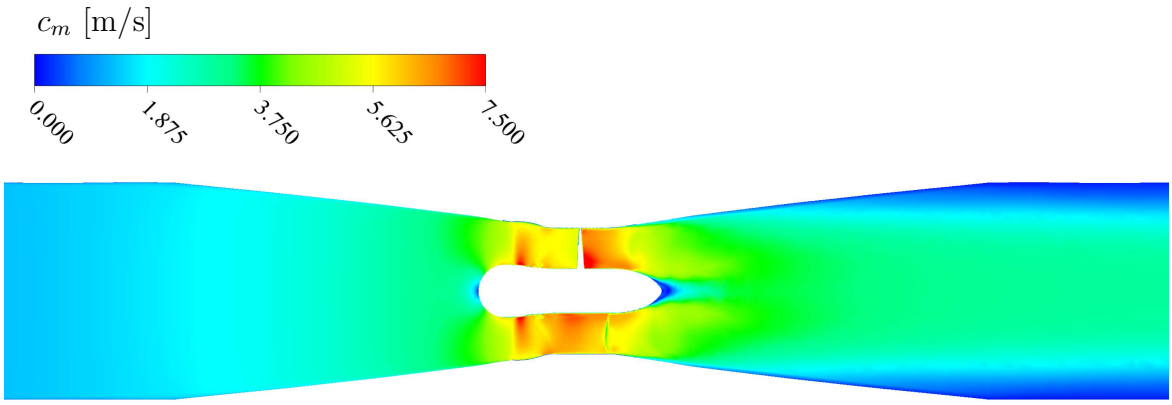

Figure 4.23: Velocity c_m in transient turbine simulation at $\gamma = 0°$, $n_1' = 155$ min^{-1}

Figures 4.24 depicts the distributions of $r \cdot c_u$ and c_m at a guide vane angle of $\gamma = 0°$ and unit speed of $n_1' = 155$ min^{-1} in solid lines for the steady state and dashed lines for the transient simulation. The distributions are almost equal, only in the distribution of $r \cdot c_u$ is a very minor difference in the region near the shroud, i.e. $S = 0.9$.

The same is true for the blade loading, which is shown in Figure 4.9 and 4.25 for the steady state and the transient turbine simulation, respectively. There is almost no difference observable between the steady state and transient simulation of the turbine mode.

Overall, this leads to the conclusion that the simulation with a reduced number of blade passages in the steady state very closely approximates the simulation results of a transient simulation of the turbine stage. However, the transient simulation is predicting a significantly better performance of the diffuser, which is due to the fact

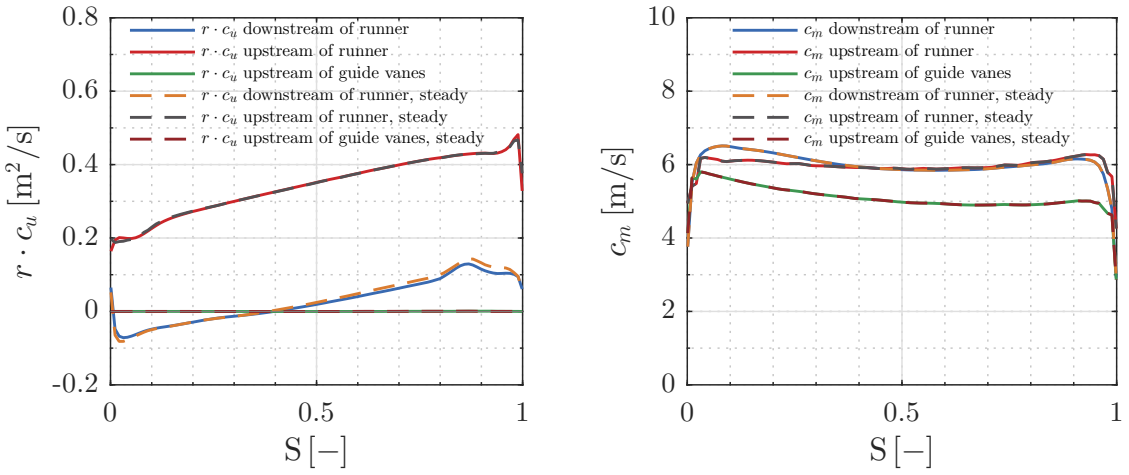

Figure 4.24: Distribution of $r \cdot c_u$ and c_m in steady state and transient turbine mode, $\gamma = 0°$, $n_1' = 155$ min^{-1}

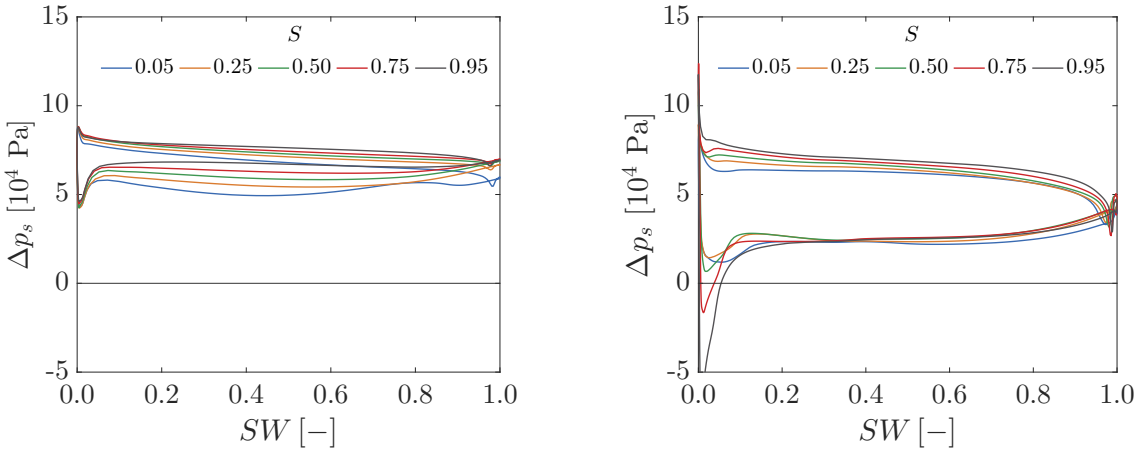

Figure 4.25: Δp_s on guide vanes (l) and runner blades (r) at $n_1' = 155$ min^{-1}, $\sigma = 1.57$, transient

that the unsteady inflow condition at the draft tube inlet is leading to a more realistic simulation of behavior of the boundary layer at the draft tube walls.

4.2.2 Pumping mode

In the pumping mode the two simulation methods produce generally similar results as well, however, the diffuser flow is modeled differently. Table 4.2 lists resulting values for selected parameters in order to compare the steady state and transient simulation results. The head H_{IEC} generated by the pumping operation is 0.044 m lower in the

Table 4.2: Comparison of steady state and transient pumping simulation results

mode	φ [−]	ψ [−]	H_{IEC} [m]	P_{me} [W]	$P_{fl,IEC}$ [W]	$\eta_{pu,IEC}$ [%]
steady state	0.328	0.106	1.386	9,198	6,458	70.2
transient	0.328	0.103	1.342	9,127	6,250	68.5
difference	0.0	-0.003	-0.044	-71	- 208	-1.7

transient simulation. This is equal to 3.2 % and shows also in the head coefficient ψ. The mechanical power P_{me} is 71 W lower in the transient case as well, which is 0.77 %, while the fluid Power P_{fl} is smaller by 208 W, which equals to 3.2 %. Overall, the pumping efficiency in the transient simulation is 1.7 % lower than in the steady state simulation.

Figure 4.26 depicts the total pressure p_t and static pressure p_s along the Z-axis of the turbine for the steady state and transient simulation. The flow direction is from $-Z$ to $+Z$, i.e. from the right to the left in the figure. The corresponding curves have

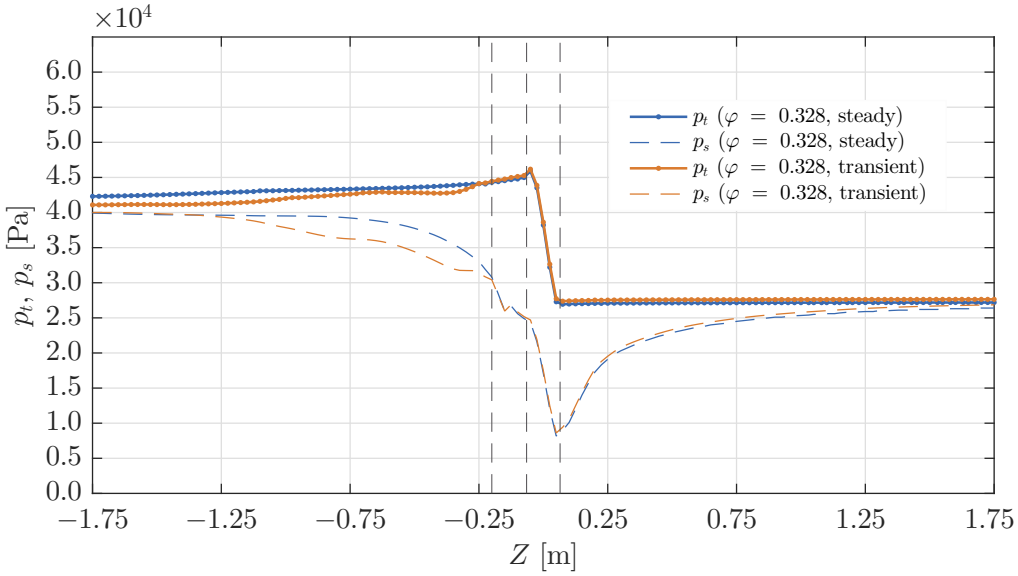

Figure 4.26: Total pressure p_t and static pressure p_s in axial direction in steady state and transient pumping simulation at $\varphi = 0.328$ and $\gamma = 5.5°$

a similar course with only minor differences starting from the inlet and then passing

the runner and guide vanes.
Downstream of the guide vanes, starting at a distance of $Z = -0.3\,\text{m}$, the curves have a different course. While the total pressure p_t shows a steady decline along the diffuser in the steady state simulation, it shows an irregular, unstable progression in the transient simulation. The losses in this region are higher in the transient simulation, which shows in an overall larger drop of p_t over the diffuser length. Correspondingly, the static pressure p_s undergoes a steady increase in the steady state simulation, while in the transient simulation, the rise is unstable, with varying gradient along the diffuser length. Beginning at a distance of $Z = -1.25\,\text{m}$ this difference seems to vanish, as the corresponding curves take the same course again.

Figures 4.27 and 4.28 depict the distribution of the meridional velocity c_m on a plane in the Y-Z direction in the steady state and transient pumping simulation, respectively.

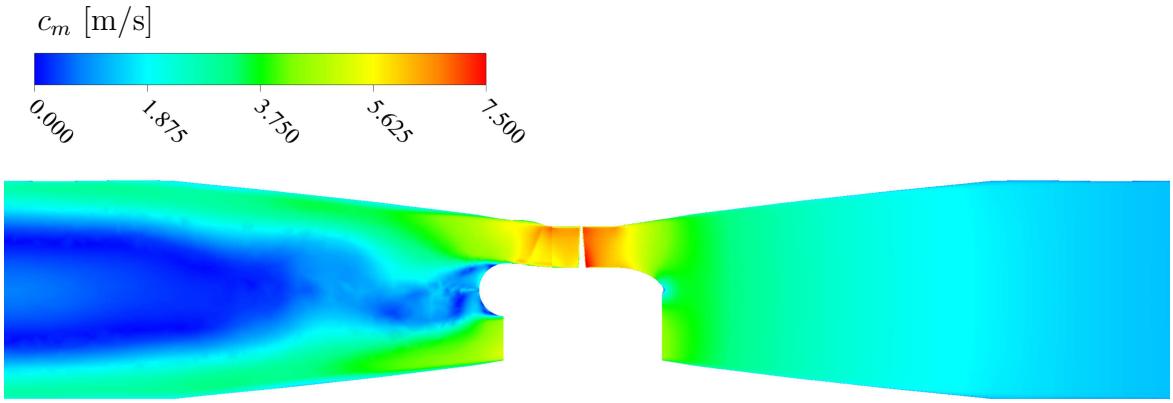

Figure 4.27: Velocity c_m in steady state pumping simulation at $\gamma = 5.5°$, $\varphi = 0.328$

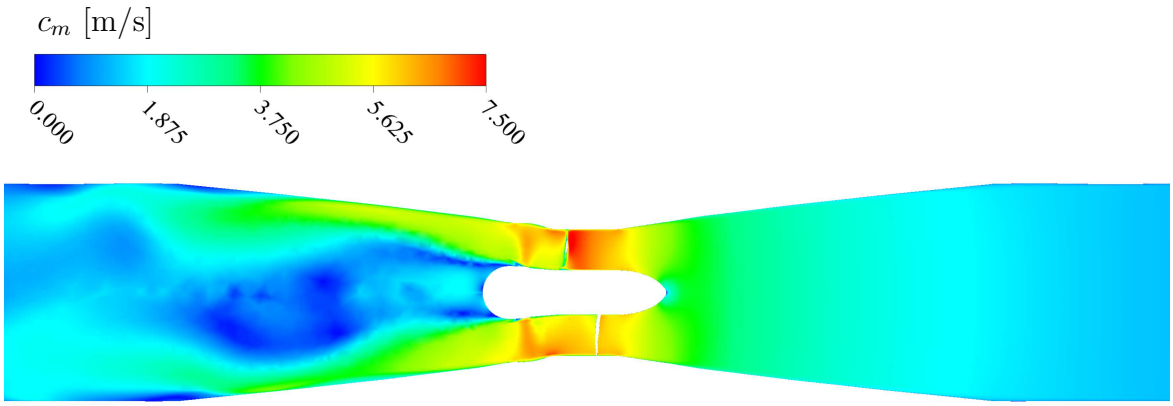

Figure 4.28: Velocity c_m in transient pumping simulation at $\gamma = 5.5°$, $\varphi = 0.328$

The flow is equal from the inlet up to the guide vanes. Downstream of the guide vanes, i.e. in the diffuser, the flow distribution is similar in a sense that most of the transport

takes place near the shroud, which shows in large values of the meridional velocity c_m. In both cases the flow detaches from the hub and there is stagnating flow in the center of the draft tube, i.e. downstream of the hub region. The exact extent and shape of this region differs between the two simulations. The flow is unstable, shows vortex shedding and generally is comparable to a Kármán vortex street. The chaotic nature of the flow in this stretch explains the different flow pattern.

Figures 4.29 depicts the distributions of $r \cdot c_u$ and c_m at a guide vane angle of $\gamma = 5.5°$ and flow coefficient of $\varphi = 0.328$ in solid lines for the steady state and dashed lines for the transient simulation.

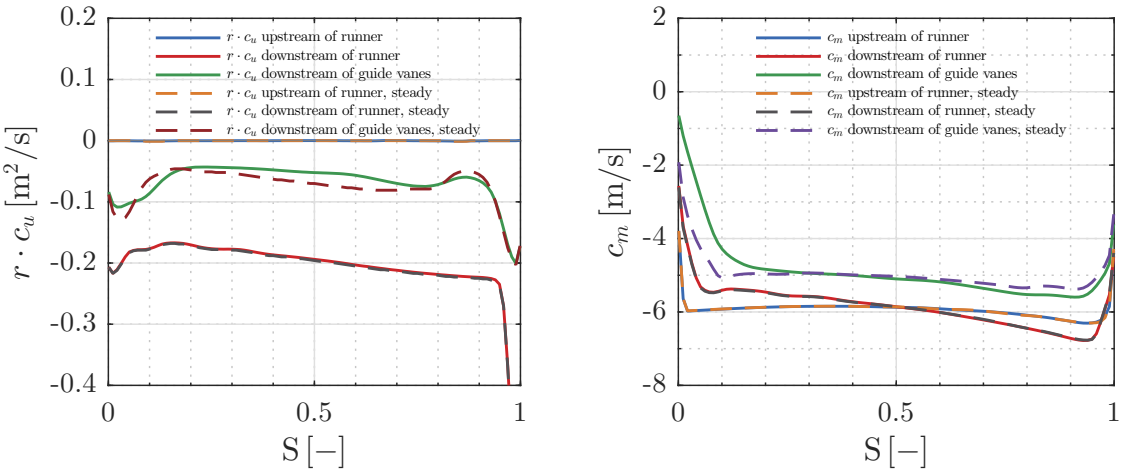

Figure 4.29: Distribution of $r \cdot c_u$ and c_m in steady state and transient pumping mode, $\gamma = 5.5°$, $\varphi = 0.328$

The distributions are equal upstream and downstream of the runner, i.e. upstream of the guide vanes. However, downstream of the guide vanes both distributions have a different shape. The $r \cdot c_u$ is very alike, but has a larger magnitude in the steady state simulation in the region of $S = 0.3$ to 0.7 and 0.05. The c_m distribution is more evenly distributed in the steady state as well. In the transient simulation, the meridional velocity is slightly increased near the shroud and strongly decreased at the hub in comparison to the steady state simulation. Thus, the velocity distribution entering the diffuser is less favorable in the transient case, which leads to a decreased performance.

As in the turbine mode, the blade loading charts, which are shown in Figure 4.19 and 4.30 for the steady state and the transient pumping simulation, respectively, are almost equal. Almost no difference is observable between the steady state and transient simulation of the pumping mode.

This indicates that steady state simulations are well suited for optimizing the runner and guide vane blades. The prediction of the diffuser performance, especially in con-

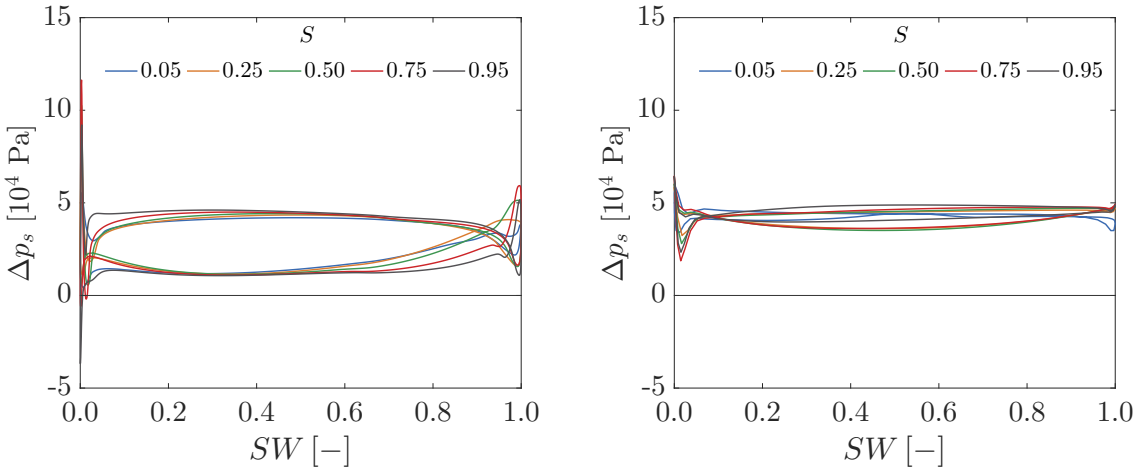

Figure 4.30: Δp_s on runner blades (l) and gv (r) at $\gamma = 5.5°$, $\varphi = 0.328$, $\sigma = 3.06$, transient

junction with beginning local flow separation on the guide vanes, appears to be more realistic in the transient simulation mode. However, as any numerical simulation, save the direct numerical simulation, has to rely on boundary layer models, a definite and accurate verification of the achievable efficiency can only be expected from a properly conducted model turbine test.

Chapter 5

Discussion and conclusions

The simulation results give a good indication that the turbine can fulfill the desired goals. Overall a peak efficiency of $\eta_{tu,IEC} = 85\,\%$ is achieved in the turbine mode, which is slightly lower than the peak efficiency of 87 % that the turbines in the Rance tidal power plant achieve in the forward turbine mode. However, it is significantly higher than the peak efficiency of 73 % in the Rance turbine's backward turbine mode. [45] gives the results of model tests of an optimized bulb turbine capable of four quadrant operation. This turbine reaches an efficiency of 78 % in the forward turbine mode and an efficiency of 80 % in the backward turbine mode. In the light of these figures, the performance of the turbine developed in the present study, with an efficiency of $\eta_{tu,IEC} = 85\,\%$ in both flow directions can be considered quite satisfactory. [79] states that bulb turbines, among others, can reach peak efficiencies of 90 %. However, this has to be seen in the light of these turbines being optimized for a single flow direction.

The loss analysis of the developed turbine has shown that the losses occurring in turbine operation are almost evenly distributed on all components, but the minimum losses of the individual components unfortunately do not occur at the same unit speed. Thus, there is scope for further improvement of the peak efficiency by optimizing the hydraulic design in such a way that all components reach their maximum efficiency at the same point of operation – a task that could not be fully accomplished within the time frame of the development project. The exit losses are relatively high, especially at medium unit speeds. A reduction of these has the largest optimization potential.

The peak efficiency reached by the present design in the pumping mode is $\eta_{pu,IEC} = 70.8\,\%$ and surpasses the peak efficiency of the Rance turbines in both the forward and backward pumping modes, which are 66 % and 58 % respectively.

In comparison to the turbine presented in [45], giving a pump efficiency of 70 %, the new turbine still offers a slight advantage. The distribution of losses in the pumping mode is comparable to the turbine mode, especially for the incoming flow and the guide

vanes. The runner losses at the points of best efficiency are also comparable, but for unit speeds deviating from the optimal point, runner losses grow rapidly. This could be due to a greater range of simulated runner speeds. In pumping mode, the pressure recovery in the draft tube is relatively low. This stems from the fact that the guide vanes cannot reduce the swirl downstream of the runner sufficiently combined with the fact that the hub has a relatively large diameter downstream of the guide vanes. This is a consequence of optimizing both the turbine and pumping modes and could not be avoided. Eventually, it leads to a relatively low peak efficiency in the pumping mode. When the turbine deviates from the optimum operation point, its efficiency drops rapidly. However, if a speed variable motor is used, the pump can always be run at its operating point of maximum efficiency. The decrease in efficiency can be attributed to two effects, the runner and draft tube losses. The steep increase of the runner losses in operating points aside from the best efficiency point is due to the rather sharp leading edge of the runner blades in pumping operation, which is giving a distinct advantage in turbine mode. The high draft tube losses are caused by a flow distribution with high velocities near the shroud and backflow in the core region of the draft tube. High velocities cause high friction losses at the draft tube walls and in the shear zone between the backflow and normal flow region. This inadequate flow distribution is induced by flow separation at the guide vanes near the hub, as depicted in Figure 4.17. The swirl of the flow downstream of the runner is not reduced near the hub and this leads to very small values of the meridional velocity c_m. The flow near the hub stagnates and leads to the formation of a backflow region downstream. This effect can potentially be reduced in a next design, by changing the guide vanes in a way that they have an even higher twist from hub to shroud. This would increase the reduction of swirl and increase the meridional velocity c_m near the hub, resulting in a better draft tube quality grade.

In summary, the efficiency of the newly developed reversible turbine design surpasses the efficiency of the Rance turbines in three out of four operating modes in a fully employed four-quadrant-operation.

The unit discharge of the turbine mode is $Q_1' = 2.3\,\mathrm{m}^3/\mathrm{s}$ at a guide vane angle of $\gamma = -5.0°$. This is higher than the unit discharge of reached by the Rance turbines at peak turbine efficiency, which is $Q_1' = 1.6\,\mathrm{m}^3/\mathrm{s}$ [11]. Larger unit discharges can be achieved at acceptable efficiency when the guide vanes are opened further.

The feasibility of the concept has been established and a first functional hydraulic design of the turbine has been developed. The peak efficiencies and unit discharge in the turbine mode, and the peak efficiency in pumping mode are satisfactory for an initial design. For commercial applications, the design can be optimized further and

a number of potential improvements have been identified. The present work further demonstrates where the fundamental challenges of the proposed concept lie.

The main constraints of the concept are the strongly limited axial extent and the required symmetry of the inlet and outlet. The small axial space and the symmetry requirement allow for only a small contraction ratio in the guide vane section. It is therefore not possible to make as much use of the conservation of angular momentum as in standard bulb turbines. This leads to an unfavorable swirl distribution ahead of the runner that can be partially mitigated by increasing the specific speed and guide vanes with a twist. This is, however, possible only up to a limited degree because the guide vanes start to produce flow separations near the hub. A modified guide vane design with longer chord length near the hub might resolve this issue. Due to the large curvature and twist of the guide vanes, the related losses are higher than usual for this kind of applications. High flow velocities also contribute to the losses.

In the first designs, in the pumping mode the incidence angle of the guide vanes near the hub was very high. This resulted in flow separation at the guide vanes, which entailed high losses and an unsatisfactory draft tube flow. Again, an increase of the specific speed, along with a twisting of the guide vanes, partially solved this problem.

However, the overall increased specific speed has drawbacks in relation to gap and runner friction losses. The new turbine's rim generator does not necessarily benefit from the high specific speed, as it has a large diameter in comparison with bulb turbines which means it inherently allows for a high torque and therefore high power at low rotational speeds.

The draft tube quality is very important and the comparatively high losses in this section of the turbine should be reduced as much as possible. The pumping mode, above all, is the mode where there is the greatest potential for increasing the efficiency of the turbine.

Critical view and study limitations The simulations results are generally be very plausible. However, some assumptions had to be made in order to fulfill the development goals in the set time frame.

One of the main limitations of the simulations is that they do not model the gap between the generator rotor and the sealing tube. Incorporating a model of the generator gap would have required a very high computational effort, since the number of mesh elements needed to resolve the narrow gap would have been very large. Neglecting to do so leads to two effects that lower the turbine efficiency. Firstly, the leakage flow rate through the generator gap is not considered. Secondly, the friction in the generator gap, which reduces the effective runner torque, is not modeled. The magnitude of both effects can only be predicted uncertainly and can lead to a significant

discrepancy between the predicted and measured efficiency in the model turbine.

In addition, several assumptions had to be made about the boundary conditions. The turbulent inlet intensity in real applications is unknown and depends on the specific features of an individual installation. It can be measured in the turbine test rig, but only after the model turbine has been manufactured and installed. During the development process, the model turbine had not yet been manufactured and, for this reason no data was available. The same is true for the inlet velocity profile and the wall roughness. The velocity distribution entering the turbine was assumed to be uniform and the turbulence inlet intensity was set to medium. Walls were simulated as hydraulically smooth, which is a standard approach given that the actual roughness of a model or prototype turbine depends on the manufacturing process.

Transient simulations could only be carried out after the optimization process had been completed. The high computational effort for analyses of this kind meant it was not possible to run multiple iterations of the turbine geometry and to simulate multiple operating points. In consequence, transient effects that influence the turbine characteristics thus were not taken into account during optimization. These are, for example, the shedding of vortex streets behind runner blades and the blade-to-blade interaction between the guide vanes and runner. A comparison between a steady state and a transient simulation of a single operating point of the finished geometry showed, however, that the principal performance characteristics predicted using the two methods are very similar and confirmed that steady state simulations were the appropriate choice for the geometry optimization.

The focus of the optimization process was on the turbine stage, i.e. the meridional contour, the guide vanes and the runner blades. Draft tube simulations were carried out for three geometries. However, a deeper analysis with more variations in geometries could yield even better results. Simulations that were carried out in a Master's Thesis after the final design was fixed showed that the draft tube design could be improved further.

The structural design of the turbine implements conservative safety margins and was evaluated using structural mechanical simulations. By making the runner blades and guide vanes thinner, it may be possible to increase the turbine's unit discharge. However, this would require a specific application to be defined, as the actual size and head of the prototype would need to be known to ensure that the structural integrity would not be endangered.

Recommendations Some improvements that potentially increase the machine characteristics can be identified from the simulation results.

Firstly, it is very probable that the draft tube design can be improved further.

With the turbine being a new concept, the focus during optimization was on the guide vanes, the runner and the meridional contour of the turbine. Due to the set time frame and the various parameters influencing the turbine performance, the draft tube geometry had to be determined at a relatively early stage in the development process and could not be altered later. Additional draft tube geometries were, however, studied in a Master's Thesis after the turbine geometry was finalized. This study suggests that the overall turbine efficiency can be improved. The step-wall diffuser approach proposed by [109] may also be worth considering.

The guide vanes and runner geometry had to be finalized at a specific date in order to manufacture the model turbine. As a result, only a limited number of designs could be evaluated. With regard to the guide vanes, profiles with less drag may improve the efficiency or unit discharge of the turbine. It is also possible that an additional bending of the leading edge into the approach flow and guide vanes with a larger twist could facilitate a better circumferential flow distribution upstream of the runner.

As with the guide vanes, a further variation of the runner blade profile and length could decrease friction losses. The thickness distribution for both the guide vanes and runner blades was designed to be symmetrical with regard to the chord length, in order to allow for an efficient pumping mode. Profiles with a maximum thickness at a chord length of 25 % to 30 % may also improve the efficiency. The hub ratio of the runner is constant in a streamwise direction. A reduction of the hub ratio along the streamwise direction could benefit the machine performance, as it may help with the deceleration of the flow velocity and improve the incoming flow of the draft tube.

If the gap friction emerges as a significant contributor to losses during the model tests, measures to reduce it should be investigated. Potential solutions are regulated air injection into the generator gap, reduction of the generator length, and lowering of the specific speed of the turbine design. Along with the gap friction, the leakage losses should be investigated and reduced if necessary. A reduction of the gap inlet width or the introduction of a labyrinth seal or a sealing lip could fulfill this function.

It should be notet that the new concept may be of interest for commercial applications but the present study does not assess its economic viability.

Outlook The hydraulic design for the new turbine was optimized and then evaluated with numerical methods. Even though these methods are very advanced, their predictions are not entirely reliable, as they rely on a number of assumptions. Before the production of a full-size prototype it is therefore necessary to perform physical model tests. When performed thoroughly, measurements on a model turbine are more authoritative than numerical simulations and can uncover unanticipated effects. The results can be used to improve and calibrate the simulation setup. Methods for use in

model tests are presented in [83].

The construction of a model turbine and subsequent investigation of the model was planned from the outset of the project. Mechanical drawings were derived from the hydraulic design and a model turbine was manufactured. Following this, the model turbine was tested in a closed loop turbine test rig at the Technical University of Munich. Detailed information about the test rig and the model turbine is presented in [76]. The model testing results and their implications are not the scope of this thesis and will be published separately.

Summary of discussion The present study shows that according to literature the energy output from tidal power plants could be increased substantially by implementing a two-way operation with pumping. However, the four-quadrant performance of tidal turbines needs to be good in order to realize the potential benefits. The simulation results of the newly developed turbine show favorable characteristics in the turbine mode and adequate performance in the pumping mode. It is thus a viable candidate for a four-quadrant turbine concept. Due to the symmetrical design which gives identical characteristics in both flow directions, the overall performance is superior to that of tidal turbines in existing power plants. The short axial length of the turbine proved to be a major design challenge that could be solved successfully. However, the optimized turbine is a first design and further research and development could improve its performance. A number of possibilities for improving the design have been identified in this study, but they could not be implemented due to restrictions in the time frame. The numerical results need to be verified by model tests and these may also provide insight into effects that could not be adequately simulated. These effects are the friction and leakage losses in the generator gap and transient effects.

Appendix A

Appendix

Table A.1: Basic harmonic constituents of the tide-generating force [11]

Type	Constituent	Designation	Period [h]
Semidiurnal	Principal lunar	M_2	12.42
	Principal solar	S_2	12.00
	Larger lunar elliptic	N_2	12.66
	Lunisolar declinational	K_2	11.97
Diurnal	Lunisolar declinational	K_1	23.93
	Larger Lunar	O_1	25.82
	Larger solar	P_1	24.07
	Larger lunar elliptic	Q_1	26.87
Long-period	Lunar fortnightly	M_f	327.86
	Lunar monthly	M_m	661.30
	Solar semiannual	S_{Sa}	2191.43

Bibliography

[1] Hötzl, S.; Schechtl, T.; Knapp, W. Development of a turnable turbine for use in barrage type tidal power plants. In *Wasserbau - mehr als Bauen im Wasser*; Rutschmann, P., Ed.; Berichte des Lehrstuhls und der Versuchsanstalt für Wasserbau und Wasserwirtschaft, TUM: München, 2016.

[2] Höller, K.; Miller, H. Rohrturbinen und STRAFLO-Turbinen für Niederdruck-Kraftwerke. *Escher Wyss Mitteilungen* **1977**, *50*, 3–10.

[3] Spain, R. A Possible Roman Tide Mill: Paper 005. *Kent Archaeological Society* **2002**.

[4] Rynne, C. Milling in the 7th-century-europe's earliest tide mills. *Archaeology Ireland* **1992**, *6*, 22–24.

[5] James, H. *Domesday book: or, The great survey of England of William the Conqueror, A.D. 1086: Facsimile of the Part Relating to Suffolk*; Ordnance Survey Office: Southampton, UK, 1863.

[6] Minchinton, W.E. Early Tide Mills: Some Problems. *Technology and Culture* **1979**, *20*, 777–786, doi:10.2307/3103639.

[7] Charlier, R.H. *Ocean energy*; Springer: Berlin, 2009; ISBN. 978-3-540-77931-5.

[8] Boyle, G. *Renewable Energy: Power for a Sustainable Future*, 3rd ed.; Oxford University Press in association with the Open University: Oxford, 2012; ISBN. 978-0-19-954533-9.

[9] Blain, C.A. Tidal Hydrodynamics and Modeling, 2-13. January 2013.

[10] Federal Highway Administration. *Tidal Hydrology, Hydraulics, and Scour at Bridges*, 1 ed.; Vol. 25, *Hydraulic Engineering Circular*, 2004.

[11] Bernshtein, L.B. *Tidal Power Plants*; Korea Ocean Research and Development Institute: Seoul, Korea, 1996; ISBN. 89-444-1001-1.

[12] Lempérière, F. An overview of tidal power potential and prospects. *Marine Energy* **2009**, *Supplement to: The International Journal on Hydropower & Dams*, 40–46.

[13] Blunden, L.S.; Bahaj, A.S. Tidal energy resource assessment for tidal stream generators. *Proceedings of the Institution of Mechanical Engineers, Part A: Journal of Power and Energy* **2007**, *221*, 137–146, doi:10.1243/09576509JPE332.

[14] Nicholls-Lee, R.F.; Turnock, S.R. Tidal energy extraction: Renewable, sustainable and predictable. *Science Progress* **2008**, *91*, 81–111, doi:10.3184/003685008X285582.

[15] Harvey, L.D.D. *Energy and the new reality 2: Carbon-free energy supply*; Earthscan: London and Washingon DC, 2010; ISBN. 18-4-9710-732.

[16] Fried, L.; Qiao, L.; Sawyer, S.; Shukla, S. Global Wind Report 2016: Annual Market Update, 2017.

[17] Burrows, R.; Walkington, I.A.; Yates, N.; Hedges, T.S.; Wolf, J.; Holt, J. The tidal range energy potential of the West Coast of the United Kingdom. *Applied Ocean Research* **2009**, *31*, 229–238, doi:10.1016/j.apor.2009.10.002.

[18] Department for Business, Energy & Industrial Strategy. Energy trends: Electricity generation, trade and consumption. London, UK, 2018.

[19] Clark, R.H. *Elements of tidal-electric engineering*; Wiley-IEEE: Hoboken, NJ, USA, 2007; ISBN. 9780470107096.

[20] Prandle, D. Simple theory for designing tidal power schemes. *Advances in Water Resources* **1984**, *7*, 21–27, doi:10.1016/0309-1708(84)90026-5.

[21] Sustainable Development Commission. Tidal Power in the UK: Research Report 5 - UK Case Studies, 2007.

[22] World Energy Council. 2007 Survey of Energy Resources: Promoting the sustainable supply and use of energy for the greatest benefit of all. London, U.K., 2007.

[23] Hammons, T.J. Tidal power. *Proceedings of the IEEE* **1993**, *81*, 419–433.

[24] Hammons, T.J. Tidal power in the UK and worldwide to reduce greenhouse gas emissions. *International Journal of Engineering Business Management* **2011**, *3*, 16–28.

[25] Waters, S.; Aggidis, G.A. Tidal range technologies and state of the art in review. *Renewable and Sustainable Energy Reviews* **2016**, *59*, 514–529, doi:10.1016/j.rser.2015.12.347.

[26] Shaw, T.L.; Watson, M.J. The effects of pumping on the energy potential of a tidal power barrage. Proceedings of the ICE - Engineering Sustainability, 2003, pp. 111–117.

[27] Burrows, R.; Walkington, I.A.; Yates, N.; Hedges, T.; Chen, D.; Li, M.; Zhou, J. Tapping the Tidal Power Potential of the Eastern Irish Sea: Joule Project JIRP106/03 Final Report. Liverpool, 2009.

[28] Sustainable Development Commission. Tidal Power in the UK: Research Report 3 - Severn Barrage Proposals, 2007.

[29] Jain, S.; Bansal, S.; Khanna, Y. Improvement in the Performance of a Tidal Power Plant Incorporating Ebbing, Positive and Negative Pumping. *Asian Journal of Scientific Research* **2013**, *6*, 508–517, doi:10.3923/ajsr.2013.508.517.

[30] J.M. Voith GmbH. Ausführungsbeispiele von Turbinen und Absperrorganen, 2025.

[31] Thamsen, P.U. Wasserturbinen. In *Dubbel: Taschenbuch für den Maschinenbau*; Grote, K.H.; Feldhusen, J., Eds.; Springer Berlin Heidelberg: Berlin, Heidelberg, 2011; pp. 26–32.

[32] Gorlov, A.M. Development of the helical reaction hydraulic turbine. Final technical report. Washington, D.C., 1998.

[33] Ragheb, M.; Ragheb, A.M. Wind Turbines Theory - The Betz Equation and Optimal Rotor Tip Speed Ratio. In *Fundamental and advanced topics in wind power*; Carriveau, R.e., Ed.; InTechOpen Open Access Publisher, 2011; pp. 19–39.

[34] Clarke, J.A.; Connor, G.; Grant, A.; Johnstone, C.; Ordonez-Sanchez, S. Contra-rotating Marine Current Turbines: Performance in Field Trials and Power Train Developments. Proceedings of the 10th World Renewable Energy Congress 2008; Sayigh, A., Ed., 2008.

[35] Miyaji, T.; Kasahara, R.; Kanemoto, T.; Kim, J.H.; Choi, Y.S.; Umekage, T. Power Stabilization System with Counter-Rotating Type Pump-Turbine

Unit for Renewable Energy. *Journal of Power and Energy Engineering* **2014**, *02*, 47–52, doi:10.4236/jpee.2014.24007.

[36] Kanemoto, T.; Suzuki, T. Counter rotating type hydroelectric unit suitable for tidal power station. *IOP Conference Series: Earth and Environmental Science* **2010**, *12*, 012111, doi:10.1088/1755-1315/12/1/012111.

[37] Sonohata, R. Study on Contra-Rotating Small-Sized Axial Flow Hydro Turbine. *Open Journal of Fluid Dynamics* **2012**, *02*, 318–323, doi:10.4236/ojfd.2012.24A039.

[38] Han, F.; Yang, L.; Yan, S.; Kubota, T. New Bulb Turbine with Counterrotating Tandemrunner. *Chinese journal of mechanical engineering* **2012**, *25*, 919–925.

[39] Biner, D.; Hasmatuchi, V.; Avellan, F.; Münch-Alligné, C. *2015 5th International Youth Conference on Energy (IYCE 2015): 27 - 30 May 2015, Pisa, Italy*; 2015; ISBN. 978-1-4673-7171-1.

[40] Miller, H. *The STRAFLO Turbine: The realisation of Harza's idea*; Escher Wyss Ltd.: Zürich, 1974.

[41] Schiffer, J.; Benigni, H.; Jaberg, H.; Wessiak, M.; Mayrhuber, J. Experimental investigation of the rim-lip-seal of a double regulated STRAFLO Kaplan-turbine under extreme conditions. Proceedings of the Hydro 2013 International Conference and Exhibition. Aqua Media International, 2013.

[42] Severn Barrage Committee.; Bondi, H. *Tidal power from the Severn Estuary*; Vol. 46, *Energy paper*, H.M.S.O.: London, 1981; ISBN. 978-0-114109165.

[43] Rice, R.; Baker, G. Annapolis: the Straflo Turbine and other operation experiences. Tidal Power: Trends and Developments; Clare, R., Ed. Thomas Telford, 1992, pp. 3–13, ISBN. 978-0-7277-1905-8.

[44] Borodin, V.; Zhepetov, V.; Sivkov, A. Floating Tidal Power Generating Unit with a Vertical Orthogonal Turbine. *Marine Energy* **2009**, *Supplement to: The International Journal on Hydropower & Dams*, 26–31.

[45] Zhengwei, W.; Xiaosheng, Y.; Yexiang, X. Hydraulic performance optimization of bidirectional tidal power turbine. *China Journal of Drainage and Irrigation Machinery Engineering* **2010**, *5*, 115–123.

[46] Bae, Y.H.; Kim, K.O.; Choi, B.H. Lake Sihwa tidal power plant project. *Ocean Engineering* **2010**, *37*, 454–463, doi:10.1016/j.oceaneng.2010.01.015.

[47] Abonnel, C.; Louis, F. La Rance: more than 40 years of successful operation. *Marine Energy* **2009**, *Supplement to: International Journal on Hydropower & Dams*, 47–50.

[48] Usachev, I.N.; Danilov, A.; Likhomanov, V. Maintaining Reliable Marine Energy Structures Under Heavy Ice Conditions in Russia. *Marine Energy* **2009**, *Supplement to: International Journal on Hydropower & Dams*, 16–20.

[49] Shpolyanskij, Y.B.; Istorik, B.L.; Usachev, I.N.; Sobolev, V. The new orthogonal turbine for tidal, wave and low-head hydropower plants. *Marine Energy* **2009**, *Supplement to: International Journal on Hydropower & Dams*.

[50] Fedorov, M.P.; Shilin, M.B. Ecological safety of tidal-power projects. *Power Technology and Engineering* **2010**, *44*, 117–121, doi:10.1007/s10749-010-0152-x.

[51] DeLory, R. Prototyp-Gezeitenkraftwerk erreicht 99% Verfügbarkeit. *Technische Rundschau Sulzer* **1987**, *69*, 3–7.

[52] Cousineau, J.; Nistor, I.; Cornett, A. Hydrodynamic Impacts of Tidal Power Lagoons in the Bay of Fundy. *Proceedings of 33rd Conference on Coastal Engineering, Santander, Spain, 2012* **2012**, *1*, doi:10.9753/icce.v33.management.69.

[53] Charlier, R.H. Sustainable co-generation from the tides. *Renewable and Sustainable Energy Reviews* **2003**, *7*, 187–213, doi:10.1016/S1364-0321(02)00011-4.

[54] Grafenberger, P.; Losbichler, L. Update on the large bulb units for the Sihwa tidal plant in Korea. *Marine Energy* **2009**, *Supplement to: International Journal on Hydropower & Dams*, 58–60.

[55] Cho, Y.S.; Lee, J.W.; Jeong, W. The Construction of a Tidal Power Plant at Sihwa Lake, Korea. *Energy Sources, Part A: Recovery, Utilization, and Environmental Effects* **2012**, *34*, 1280–1287, doi:10.1080/15567030903586055.

[56] Schneeberger, M. Gegenwart und Zukunft der Kaplan-Turbine bei Andritz Hydro. *Wasserwirtschaft* **2014**, *104*, 46–50, doi:10.1365/s35147-014-1054-x.

[57] Dadswell, M.J.; Rulifson, R.A.; Daborn, G.R. Potential Impact of Large-Scale Tidal Power Developments in the Upper Bay of Fundy on Fisheries Resources of the Northwest Atlantic. *Fisheries* **1986**, *11*, doi:10.1577/1548-8446(1986)011<0026:PIOLTP>2.0.CO;2.

[58] Walters, R.A.; Tarbotton, M.R.; Hiles, C.E. Estimation of tidal power potential. *Renewable Energy* **2013**, *51*, 255–262, doi:10.1016/j.renene.2012.09.027.

[59] Peters, C. *Severn Estuary Tidal Power*; National Assembly for Wales: Cardiff Bay, UK, 2010.

[60] Xia, J.; Falconer, R.A.; Lin, B. Impact of different operating modes for a Severn Barrage on the tidal power and flood inundation in the Severn Estuary, UK. *Applied Energy* **2010**, *87*, 2374–2391, doi:10.1016/j.apenergy.2009.11.024.

[61] Anthony, L.J. *Information Sources in Energy Technology: Butterworths Guides to Information Sources*; Elsevier Science, 2013; ISBN. 978-1-4831-9233-8.

[62] Severn Tidal Power Group. *The Severn Barrage Project: General report, Energy Paper 57*; Vol. 57, *Energy paper*, H.M.S.O: London, 1989; ISBN. 9780114129521.

[63] Sustainable Development Commission. Tidal Power in the UK: Research Report 2 - Tidal technologies overview. Bristol, UK, 2007.

[64] Department of Energy & Climate Change. Severn Tidal Power: Feasibility Study Conclusions and Summary Report, October 2010.

[65] Hendry, C. The Role Of Tidal Lagoons, December 2016.

[66] Cockle, P.J. The Mersey Barrage - indirect benefits: the economic and regional case. Tidal Power; Gray, T.J., Ed. Plenum Press, 1972, ISBN. 978-1-4613-4594-7.

[67] Park, Y.H. Analysis of characteristics of Dynamic Tidal Power on the west coast of Korea. *Renewable and Sustainable Energy Reviews* **2017**, *68*, 461–474, doi:10.1016/j.rser.2016.10.008.

[68] Shihai, H.; Jinhua, J. *Planning and Site Selection Report for Preselected Tidal Power Stations in Zhejiang Province*; HydroChina Huadong Engineering Corporation: Hangzhou, China, 2009.

[69] Singh, V.P.; Hager, W.H. *Environmental hydraulics*, 1 ed.; Vol. 19, *Water science and technology library*, Springer-Science+Business Media Dordrecht: Dordrecht and Boston, 1996; ISBN. 0-7923-3983-5.

[70] Wolf, J.; Walkington, I.A.; Holt, J.; Burrows, R. Environmental impacts of tidal power schemes. *Proceedings of the Institution of Civil Engineers - Maritime Engineering* **2009**, *162*, 165–177, doi:10.1680/maen.2009.162.4.165.

[71] Fedorov, M.P.; Usachev, I.N.; Demidenko, N.A. Ecological aspects of tidal powerplants. *Marine Energy* **2009**, *Supplement to: International Journal on Hydropower & Dams*, 32–35.

[72] Ivanov, A.V.; Filipov, G.G.; Usachev, I.N. Fish pass facilities at the Severnaya tidal plant. *Marine Energy* **2009**, *Supplement to: International Journal on Hydropower & Dams*, 36–38.

[73] Yebra, D.M.; Kiil, S.; Dam-Johansen, K. Antifouling technology—past, present and future steps towards efficient and environmentally friendly antifouling coatings. *Progress in Organic Coatings* **2004**, *50*, 75–104, doi:10.1016/j.porgcoat.2003.06.001.

[74] Bernshtein, L.B.; Usachev, I.N. Utilization of Tidal Power in Russia in Overcoming the Global Energy and Ecological Crisis. *La Houille Blanche* **1997**, *83*, 96–100, doi:10.1051/lhb/1997022.

[75] Schneeberger, M.; Schmid, H. StrafloMatrix: Further refinement to the HYDROMATRIX technology, 2011.

[76] Schechtl, T.; Hötzl, S.; Rutschmann, P.; Knapp, W. Development of a Low Head Tidal Turbine Part 2: Test Rig and Model Turbine Design. Proceedings of the European Wave and Tidal Energy Conference 2017; Lewis, T., Ed., 2017.

[77] Denton, J.D. Some Limitations of Turbomachinery CFD. Proceedings of ASME Turbo Expo 2010: Power for Land, Sea and Air; ASME., Ed. ASME, 2010, pp. 735–745, ISBN. 978-0-7918-4402-1.

[78] Euler, L. Théorie plus complette des machines qui sont mises en mouvement par la réaction de l'eau. In *Histoire de l'Académie Royale des Sciences et des Belles Lettres de Berlin 1745[-1757, 1792 et 1793]:*; Haude., Ed.; Deutsche Akademie der Wissenschaften zu Berlin: Berlin, 1756; pp. 227–295.

[79] Sigloch, H. *Strömungsmaschinen: Grundlagen und Anwendungen*, 6 ed.; Carl Hanser Verlag: München, 2018; ISBN. 978-3-446-4549-89.

[80] Wilson, D.G. *The Design of High-Efficiency Turbomachinery and Gas Turbines*; MIT Press and MIT: Cambridge, Massachusetts, 1984; ISBN. 026223114-x.

[81] Hutter, M. Numerische Untersuchung und Optimierung der Leitrad-Laufrad-Saugrohrinteraktion bei Axialturbinen. PhD thesis, Technische Universität München, München, 15. September 2015.

[82] Giesecke, J.; Mosonyi, E. *Wasserkraftanlagen: Planung, Bau und Betrieb*; Springer-Verlag Berlin Heidelberg: Berlin, Heidelberg, 2009; ISBN. 978-3-540-88989-2.

[83] International Electrotechnical Commission. Hydraulic turbines, storage pumps and pump-turbines – Model acceptance tests, 16.11.1999.

[84] Pejovic, S.; Karney, B.W.; Zhang, Q.; Kumar, G. Smaller Hydro, Higher Risk. 2007 IEEE Canada Electrical Power Conference; IEEE Staff., Ed. IEEE, 2007, pp. 91–96, ISBN. 978-1-4244-1444-4.

[85] Dubbel, H. *Zahlentafeln und Formeln für den Maschinenbau*, 9 ed.; Springer Berlin Heidelberg: Berlin, Heidelberg and s.l., 1947; ISBN. 978-3-6425-2673-2.

[86] Crum, L.A. Cavitation Microjets as a Contributory Mechanism for Renal Calculi Disintegration in Eswl. *The Journal of Urology* **1988**, *140*, 1587–1590, doi:10.1016/S0022-5347(17)42132-X.

[87] Deniz, S.; Bosshard, M.; Speerli, J.; Volkart, P. *Saugrohre bei Flusskraftwerken*; Vol. 106, *VAW Mitteilungen*, Versuchsanstalt für Wasserbau Hydrologie und Glaziologie der ETH Zürich: Zürich, 1990.

[88] Deniz, S.; Speerli, J.; Volkart, P. *Saugrohre, Geschwindigkeitsmessungen am Saugrohraustritt einer Rohrturbine*; Vol. 109, *VAW Mitteilungen*, Versuchsanstalt für Wasserbau Hydrologie und Glaziologie der ETH Zürich: Zürich, 1991.

[89] Laurien, E.; Oertel, H. *Numerische Strömungsmechanik*; Springer Fachmedien Wiesbaden: Wiesbaden, 2013; ISBN. 978-3-658-03144-2.

[90] ANSYS Inc.. ANSYS CFX, Release 17.2, Help System, 2016.

[91] Kuhlmann, H.C. *Strömungsmechanik*; Pearson Studium: München, 2007; ISBN. 978-3-8273-7230-7.

[92] Ferziger, J.H.; Perić, M. *Numerische Strömungsmechanik*; Springer: Berlin, 2008; ISBN. 978-3-540-67586-0.

[93] Mazumder, S. *Numerical methods for partial differential equations: Finite difference and finite volume methods*; Academic Press: London, 2016; ISBN. 9780128498941.

[94] Wilcox, D.C. *Turbulence modeling for CFD*, 3 ed.; DCW Industries: La Cãnada Flintridge, U.S., 2006; ISBN. 978-1-9287-2908-2.

[95] Thompson, D.J.; Latorre Iglesias, E.; Liu, X.; Zhu, J.; Hu, Z. Recent developments in the prediction and control of aerodynamic noise from high-speed trains. *International Journal of Rail Transportation* **2015**, *3*, 119–150, doi:10.1080/23248378.2015.1052996.

[96] Kajishima, T.; Taira, K. *Computational fluid dynamics*; Springer Berlin Heidelberg: New York NY, 2016; ISBN. 978-3-3194-5302-6.

[97] George, W.K. *Lectures in Turbulence for the 21st Century*; 2013.

[98] Versteeg, H.K.; Malalasekera, W. *An introduction to computational fluid dynamics: The finite volume method*, 1 ed.; Longman Scientific & Technical: Harlow, UK, 1995; ISBN. 0-582-21884-5.

[99] Menter, F.R. Two-equation eddy-viscosity turbulence models for engineering applications. *AIAA Journal* **1994**, *32*, 1598–1605.

[100] Menter, F.R.; Kuntz, M.; Langtry, R. Ten years of industrial experience with the SST turbulence model. *Proceedings of the Fourth International Symposium on Turbulence, Heat and Mass Transfer, Antalya, Turkey, 12-17 October, 2003* **2003**.

[101] Kato, M.; Launder, B. The modelling of turbulent flow around stationary and vibrating square cylinders. *Proceedings of the 9th Symposium on Turbulent Shear Flow* **1993**, pp. 10.4.1–10.4.6.

[102] Russo, F.; Basse, N.T. Scaling of turbulence intensity for low-speed flow in smooth pipes. *Flow Measurement and Instrumentation* **2016**, *52*, 101–114, doi:10.1016/j.flowmeasinst.2016.09.012.

[103] Schlichting, H.; Gersten, K. *Grenzschicht-Theorie*, 10 ed.; Springer: Berlin, 2006; ISBN. 3-540-23004-1.

[104] Fröhlich, J. *Large Eddy Simulation turbulenter Strömungen: Mit 14 Tabellen*, 1 ed.; Lehrbuch Maschinenbau, Teubner: Wiesbaden, 2006; ISBN. 978-3-8351-0104-3.

[105] Denton, J.D.; Singh, U.K. Time marching methods for turbomachinery flow calculation. *von Karman Institute Lecture Series* **1979**.

[106] Benigni, H.; Jaberg, H. Stationary and transient numerical simulation of a bulb turbine. *Proceedings of the 5th IASME / WSEAS International Conference on Fluid Mechanics and Aerodynamics, Athens, Greece, August 25-27, 2007* **2007**, pp. 135–140.

[107] KC, A.; Thapa, B.; Lee, Y.H. Transient numerical analysis of rotor–stator interaction in a Francis turbine. *Renewable Energy* **2014**, *65*, 227–235, doi:10.1016/j.renene.2013.09.013.

[108] Yamada, Y. Torque Resistance of a Flow between Rotating Co-Axial Cylinders Having Axial Flow. *Bulletin of JSME* **1962**, *5*, 634–642, doi:10.1299/jsme1958.5.634.

[109] Lo, K.P.; Elkins, C.J.; Eaton, J.K. Flow Separation Control in an Annular to Conical Diffuser Using Two-Dimensional and Three-Dimensional Wall Steps. *Journal of Fluids Engineering* **2013**, *135*, 041102–1–11, doi:10.1115/1.4023648.